



저작자표시 2.0 대한민국

이용자는 아래의 조건을 따르는 경우에 한하여 자유롭게

- 이 저작물을 복제, 배포, 전송, 전시, 공연 및 방송할 수 있습니다.
- 이차적 저작물을 작성할 수 있습니다.
- 이 저작물을 영리 목적으로 이용할 수 있습니다.

다음과 같은 조건을 따라야 합니다:



저작자표시. 귀하는 원저작자를 표시하여야 합니다.

- 귀하는, 이 저작물의 재이용이나 배포의 경우, 이 저작물에 적용된 이용허락조건을 명확하게 나타내어야 합니다.
- 저작권자로부터 별도의 허가를 받으면 이러한 조건들은 적용되지 않습니다.

저작권법에 따른 이용자의 권리는 위의 내용에 의하여 영향을 받지 않습니다.

이것은 [이용허락규약\(Legal Code\)](#)을 이해하기 쉽게 요약한 것입니다.

[Disclaimer](#) 

이학박사 학위논문

**Molecular design of protein-based biomaterials and
hierarchical porous polyimides**

단백질 기반의 바이오 나노 소재 및 계층적
다공성 구조의 고분자 이미드의 분자적 설계

2022 년 8 월

서울대학교 대학원
화학부 무기화학전공
양 민 우

Ph.D Dissertation

**Molecular design of protein-based biomaterials and
hierarchical porous polyimides**

단백질 기반의 바이오 나노 소재 및 계층적
다공성 구조의 고분자 이미드의 분자적 설계

October 2022

Graduate School of Seoul National University

Department of Chemistry

Inorganic Chemistry Major

Minwoo Yang

Molecular design of protein-based biomaterials and hierarchical porous polyimides

지도교수 송 윤 주

이 논문을 이학박사 학위논문으로 제출함

2022 년 8월

서울대학교 대학원

화학부 무기화학전공

양 민 우

양민우의 박사 학위논문을 인준함

2022 년 8 월

위 원 장 이 윤 호 (인)

부 위 원 장 송 윤 주 (인)

위 원 이 동 환 (인)

위 원 이 연 (인)

위 원 홍 승 우 (인)

Abstract

Molecular design of protein-based biomaterials and hierarchical porous polyimides

Minwoo Yang

Departments of Chemistry, Inorganic Chemistry

The Graduate School

Seoul National University

Molecular design often requires delicate consideration of not only building blocks but also proper reaction conditions. Controlling precursors, reaction phase, temperatures, pressure, adducts, catalysts, and even substrate changes the overall morphology and function of resulting materials. Thus, proper processing methods should be considered to unlock the full potential of designed materials. This dissertation includes the generation of protein-based biomaterials and porous organic polyimides through bottom-up approaches. Proper synthetic strategies for extending selected building units into 1, 2, and 3 dimensions, and the effect of the strategies on the properties and functions of materials will be discussed.

Chapter 1 briefly introduces the field of artificially extended protein assembly. Among diverse protein-protein interface design strategies, coordination

interaction for artificial protein assembly will mainly be discussed. Chapter 2 demonstrates that diverse protein-assembled architectures can be programmed by site-selective genetic incorporation of an unnatural chelating amino acid, bpy-Ala, followed by the addition of metal ions. Although the selected protein for our study exhibits no structural and functional properties related to self-assembly, the addition of Ni^{2+} to the chelating ligands creates potent and reversible connecting modules, $[\text{Ni}(\text{bpy})_2]$, resulting in selective and tunable protein-assembled architectures. Notably, only a single-site mutation to determine the location of bpy-Ala residue was sufficient to generate diverse structures such as one-directional linear rods, two-directional P312 planes, non-crystalline 2D, combinatory, and hierarchical architectures, demonstrating that metal-coordinating ligands endow sufficiently strong driving force and designable directionality to generate robust and diverse structures. The protein self-assembly process was extensively explored under various reaction conditions, suggesting that both thermodynamic and kinetic controls are operative and the length and shape of the protein-assembled structures are tunable. Besides, the assembled-protein structures gained thermal stability, while exhibiting their native enzyme activities, implicating that genetically incorporated inorganic reactivity can easily template biological macromolecules into versatile protein-based functional materials and biocatalysts.

Chapter 3 is about the utilization of redox-active porous organic polymers for energy storage materials. The properties and advantages of redox-active porous organic polymers will be discussed from the point of electrode applications. Chapter 4 mainly focuses on the design strategy for high-performance energy storage devices based on the structure-function relationship. We aimed to construct porous organic polymers containing redox-active groups with highly permeable structures, using an unprecedented combination of hexaazatriphenylene carboxylic acid and melamine. Our design strategy was (1) synthesizing highly redox-active hexaazatriphenylene triimide groups for high energy density materials and (2) generating mesoporous channels resulted from contorted micropores to facilitate the high flux of ions for high power density materials. Adopting self-assembly as a

processing method, homogeneous fibril morphology with an imidized network was achieved, indicating targeted highly redox-active groups were successfully formed (PI-Fiber). The structural analysis confirmed that a hierarchical porous structure with a uniform size of micropore was formed as designed. Even though our materials are poor-crystalline systems, desired imide bonds and hierarchical structures were successfully generated, demonstrating that the two-step approach is an effective method for constructing our targeted materials. As expected, pseudocapacitive behavior with high charge capacity was achieved even at a fast charge/discharge rate. Our active material exhibited moderate stability, and its fast kinetics and decay mechanism were thoroughly investigated via cyclic voltammetry. We also constructed two-electrode systems to test the possibility of applications in practical devices. The assembled AC//PI-Fiber cell exhibited high power and energy densities with moderate stability, demonstrating PI-Fiber can be a prospective electrode material for practical applications.

Keywords: biomaterials, bipyridine metal complex, polyimides, porous organic polymers, protein, psuedocapacitors, redox-active polymer, reversible interactions.

Student Number: 2017-27428

Table of Contents

Chapter 1. Extended protein assembly via coordination chemistry	1
1.1. Extended protein assembly structures.....	2
1.2. Coordination chemistry for protein-protein interface (PPI) design	3
1.3. Challenges in designing artificially extended protein assembly	6
1.4. References	9
Chapter 2. Diverse protein assembly driven by metal and chelating amino acids with selectivity and tunability.....	13
2.1. Introduction.....	14
2.2. Design strategy.....	15
2.3. 1-Dimensional assembly design.....	18
2.4. 2-Dimensional assembly design.....	29
2.5. Generation of combinatorial and hierarchical structures	35
2.6. Stability test of assembled structures	38
2.7. Conclusion	42
2.8. Experimental section.....	43
2.9. References.....	55

Chapter 3. Application of redox-active porous organic polymers in electrochemical energy storage materials	56
3.1. Redox-active porous organic polymers.....	57
3.2. Redox-active POPs for high energy/power density energy storage materials.....	58
3.3. Configurations for organic electrode materials in EESSs.....	60
3.4. Demands for organic materials with highly permeable structures	62
3.5. References.....	64
Chapter 4. One-pot two-step synthesis of micro- and mesoporous organic fibrils for efficient pseudocapacitors	67
4.1. Design strategy.....	68
4.2. Synthesis and morphological studies of PI-Fiber.....	70
4.3. Characterization of imide bond formation in PI-Fiber.....	74
4.4. Structural characterization of PI-Fiber.....	77
4.5. Electrochemical characterization and application of PI-Fiber for pseudocapacitors	80
4.6. Conclusion	95
4.7. Experimental section.....	96
4.8. References.....	104
Appendix	108

Lists of Figures, Tables, and Schemes

Lists of Figures

Chapter 1. Extended protein assembly via coordination chemistry

Figure 1.1. Examples of naturally occurring extended protein assemblies.....	2
Figure 1.2. Examples of metal-chelating amino acids in natural and unnatural systems, and advantages of coordination chemistry for protein assembly.....	4
Figure 1.3. Advantages of covalent and coordination interactions over noncovalent interactions for protein assembly design.	6
Figure 1.4. Pathway-dependent outcomes in extended assembly.	8

Chapter 2. Diverse protein assembly driven by metal and chelating amino acids with selectivity and tunability

Figure 2.1. Illustration of assembly strategy.	15
Figure 2.2. Assembled structures of K44Z	18
Figure 2.3. Metal-dependent 1D-rod formation with K44Z	19
Figure 2.4. TEM images of K44Z-linear assembly of with the mixtures of metal ions.....	20
Figure 2.5. TEM images of K44Z (10 μ M) reacted with Ni ²⁺ with variations of salt concentration	21
Figure 2.6. Formation of K44Z-derived rods at various pH condition.	22

Figure 2.7. Optimization of K44Z-rod formation	23
Figure 2.8. Kinetics of 1D-rod formation	24
Figure 2.9. Concentration dependency of assembly at 37 °C and changes in distributions, average lengths, and maximum lengths of assembled structures after condition optimization	26
Figure 2.10. Tunability of metal-binding sites and changes in assembly aspects	27
Figure 2.11. Effects of mutations in metal binding sites on metal selectivity..	28
Figure 2.12. Experimental and plausible 2-D assembled structures of K337Z variant with Ni ²⁺	29
Figure 2.13. TEM images of 2D-planes under various conditions	30
Figure 2.14. Kinetics of 2D assembly.	31
Figure 2.15. Formation of noncrystalline 2D aterials with W298Z with Ni ²⁺	33
Figure 2.16. Various structures derived from 1D rods and/or 2D planes.....	35
Figure 2.17. Fibril formation with 1D-rods upon solvent addition.....	37
Figure 2.18. TEM images of the 1D and 2D-assembled structures after heating at 55 °C	38
Figure 2.19. The native enzyme activities as acetyltransferases in the reactions with acetyl coenzyme A and kanamycin before and after heating at 55 °C	40
Figure 2.20. Expression and purification of bpy-Ala variants	50

Figure 2.21. TEM images of the linear rods collected with different focal points.	52
--	----

Chapter 3. Application of redox-active porous organic polymers in electrochemical energy storage materials

Figure 3.1. Characteristics of redox-active POPs	59
Figure 3.2. Configurations for organic electrode materials in Li batteries	61
Figure 3.3. Effect of Hierarchical structures on ion permeability and power density of supercapacitors.....	62

Chapter 4. One-pot two-step synthesis of micro- and mesoporous organic fibrils for efficient pseudocapacitors

Figure 4.1. Reported reduction potentials and LUMO levels of triphenylene and hexaazatriphenylene derivatives	68
Figure 4.2. Illustration and DFT-calculated structural model of the building unit of desired structures	69
Figure 4.3. Structures of pre-organized and reacted species of PI-Fiber.	70
Figure 4.4. TEM images of fibrils synthesized with various concentrations of monomers.....	71
Figure 4.5. Effects of solvent on polymer synthesis.	72
Figure 4.6. TEM images of samples prepared under unoptimized conditions.	73

Figure 4.7. Fourier transform infrared spectroscopy (FTIR) spectra of building units and samples synthesized via above conditions.....	74
Figure 4.8. Chemical analysis of bond formation in PI-Fiber.....	75
Figure 4.9. High-resolution XPS spectra and C _{1s} , O _{1s} profile of HATCO ₂ H ..	76
Figure 4.10. Structural analysis of PI-Fiber (PXRD and HR-TEM).....	77
Figure 4.11. Structural analysis of PI-Fiber (micropore analysis).	78
Figure 4.12. The expected structure of protofilaments constituting PI-Fiber and its schematic illustration	79
Figure 4.13. Electrochemical application of PI-Fiber and electrode preparation process	80
Figure 4.14. CV curves of working electrodes prepared by sonication under various conditions	81
Figure 4.15. Mass loading optimization.....	82
Figure 4.16. CV curves measured at 100 mV s ⁻¹ in various electrolytes	83
Figure 4.17. CV curves of working electrodes constructed from PI-Fiber or samples synthesized from non-assembled building units.	84
Figure 4.18. Galvanostatic charge and discharge (GCD) curves of working electrodes in three-electrode systems.....	85
Figure 4.19. Nyquist plot from 10 kHz to 20 mHz at different offset voltages	86
Figure 4.20. Stability test and electrochemical properties of PI-Fiber before and after cycling.....	87

Figure 4.21. Electrochemical properties of PI-Fiber before and after cycling..	91
Figure 4.22. Electrochemical analysis of PI-Fiber in two-electrode system....	93
Figure 4.23. ^{13}C NMR spectrum of HATCO ₂ H.....	99
Figure 4.24. Liquid chromatography and mass spectroscopy spectrum of HATCO ₂ H.	99

Lists of Tables

Table 2.1. Equilibrium constants of 1st-row transition metals for bipyridine (mono- and bisbipyridinyl complexes) and hydroxide ion	17
Table 2.2. Sequence of the selected protein for the current work.	47
Table 2.3. Primer sequences used for site-directed mutagenesis..	48
Table 4.1. Specific capacities and columbic efficiencies at different current densities.	85
Table 4.2. Specific capacities and columbic efficiencies of the cycled electrode at different current densities.....	88
Table 4.3. Comparison of charge capacity (mAh g ⁻¹), and capacitance (F g ⁻¹) between PI-Fiber and materials in previously reported literature	90
Table 4.4. The electrochemical performance of AC//PI-Fiber	94

Lists of Schemes

Scheme 2.1. A series of reactions related to protein-assembly using bpy ligand.

Equation (1) - (3).	17
Scheme 2.2. The colorimetric assay to measure the activity of aminoglycoside acetyl-transferase.	40
Scheme 2.3. Synthesis of Bpy-Ala.....	43
Scheme 4.1. Schematic illustration of porous polyimide generation.....	69
Scheme 4.2. Synthesis of 1,4,5,8,9,12-hexaazatriphenylene hexacarboxylic acid.....	97

Chapter 1. Extended protein assembly via coordination chemistry

1.1. Extended protein assembly structures

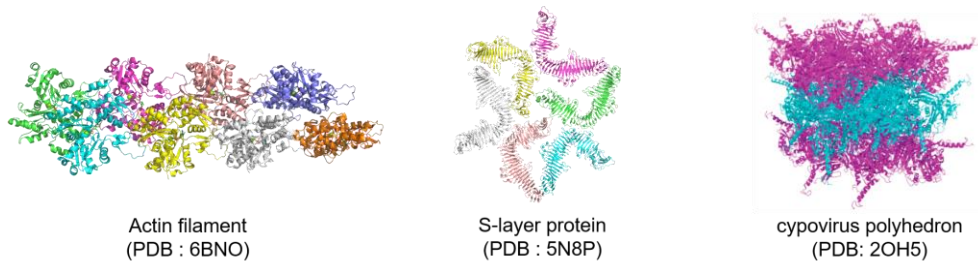


Figure 1.1. Examples of naturally occurring extended protein assemblies.

Elaborate systems of nature with more advanced functionality and structural complexity come from covalently linked biological polymers such as polysaccharides for energy storage^{1,2,3}, polynucleotides for genetic information maintenance, and transmittance^{4,5,6}, and polypeptides for chemical, physical, and mechanical information transfer^{7,8,9}. Polypeptides have superior chemical versatility among biopolymers since the linear polymers constituted of 20 different building units have nearly an infinite number of possible combinations. The intramolecular chemical interactions between building units in linear polymer construct well-defined 3-dimensional structures, protein, which can act as a catalyst^{10,11}, transporter¹², signal recorder¹³, and transducer¹⁴. Nature further utilizes these tens of thousands of Dalton macromolecules to build well-ordered extended protein assembly structures which serve as scaffolding/transport of other cellular components, structural integrities, and mechanical/architectural elements. For instance, 1-dimensional filament structures such as actin¹⁵ or microtubules¹⁶ perform in controlling cellular movement, shape, and intracellular transport; 2-dimensionally assembled protein architectures such as bacterial S-layers¹⁷ serve as selective membranes or protective layers; 3-dimensional protein lattices such as cypovirus polyhedrin¹⁸ and peroxisomal alcohol oxidase¹⁹ act as platforms for catalysis, storage, and scaffolding (Figure 1.1).

As the needs for platforms with diverse functionalities and compatibilities increase, materials with unprecedented building blocks have been enormously reported. With controlling chemical and structural properties of organic, inorganic, or even biological composites, promising materials that can be used as sensors, catalysts, conductors or insulators, filters, separators, energy storage or production systems, and gas storage systems are emerging²⁰⁻²². Especially, bottom-up fabrication of protein-based nanomaterials is a growing research field in material science. The bionanomaterials constructed by periodic arrays of proteins can be innovative materials since the surface residues and well-defined active sites of proteins are prone to be functionalized with catalytic or sensing molecules²³⁻²⁵. Self-assembled architectures of this complex, but elaborate and promising building block can be utilized for drug-delivery²⁶ and multi-catalytic systems²⁷ in various environments due to their enhanced stability against organic solvent and heat²⁸.

1.2. Coordination chemistry for protein-protein interface (PPI) design

Major obstacles in developing protein-based materials are the instability and complexity of building units. Connecting building blocks into crystalline or at least ordered array with enthalpy gain requires high activation energy, which often causes destabilization and aggregation of proteins. Also, chemical interactions from multiple residues in proteins can interrupt designed chemical bonding, resulting in the irregular aggregates of proteins. Designing intermolecular protein-protein interfaces (PPI) which afford the generation of artificial protein-based frameworks without building unit destabilization is thus, an area of interest itself²⁹. Naturally occurring hierarchical construction of extended protein assemblies gave insights into the strategy for artificial protein-based biomaterials. Chemical interactions such as electrostatic^{30,31}, hydrophobic^{32,33}, covalent disulfide³⁴, hydrogen-bonding^{35,36}, and metal coordination³⁷⁻³⁹ have been used to drive intermolecular self-assembly

between proteins.

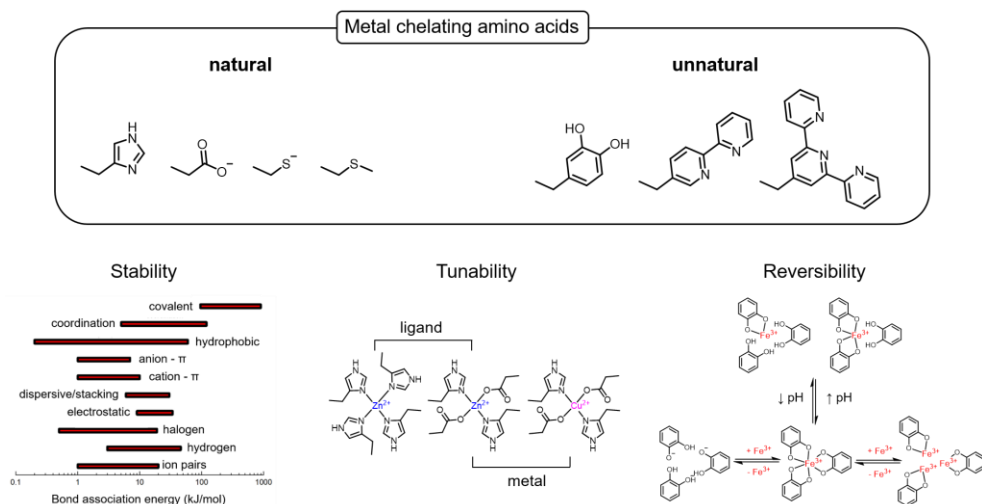


Figure 1.2. Examples of metal-chelating amino acids in natural and unnatural systems, and advantages of coordination chemistry for protein assembly.

Coordination bonds play a significant role in stabilizing tertiary and quaternary structures of proteins⁴⁰. Interfacial metal ions or metallocofactors maintain overall oligomeric protein structures, mediating transient PPI⁴¹, and serving as catalytic centers⁴². From the point of material construction, coordination bonds are highly promising connecting strategies, as coordinative interactions are energetically more stable than non-covalent interactions while at the same time, reversible, enabling them to break and reform repeatedly (Figure 1.2). The thermodynamic stability and kinetic lability of the coordination complex enable the formation of PPI with a simple design, and the assembly structure to continuously flow and remodel to form desirable structures, respectively.

Finitely assembled structures such as oligomers⁴³, and nanorings⁴⁴, and extended assembled structures involving 1-dimensional fibril⁴⁵, ribbon⁴⁶, 2-dimensional sheet⁴⁶, and 3-dimensional lattice⁴⁷ were reported by utilizing naturally occurring metal-binding amino acids (e.g. histidine, glutamate, aspartate, and cysteine) and non-biological ligands (e.g. bi-, terpyridine, phenanthroline, and

hydroxamate) with mid-late 1st-row transition metals. Among naturally occurring amino acids, multiple histidine clamp is the most used metal binding moiety for designing PPI. The concept of treating proteins as large metal-chelating ligands was pioneered by Tezcan and co-workers⁴⁸. They inserted two bis-His motifs into four-helix bundle protein and generated tetrameric assembly by adding Zn (II) ions. Further analysis revealed that the insertion of aspartate or glutamate near the metal complex controlled the innate geometrical preference of the metal ions and the overall geometry of the resultant protein assembly⁴³. Inspired by this approach, diverse protein assembly structures were constructed later using multiple histidine moieties and transition metals (e.g. Ni²⁺, Cu²⁺, and Zn²⁺). Abiological metal chelating groups are also frequently used for designing metal-complex mediated protein assembly strategies. The complexation of surface-modified bipyridine or phenanthroline groups with Fe²⁺ yielded coordination polymers⁴⁹ or controlled self-assembly⁵⁰ of proteins. The strong preference of Fe²⁺ ions to form [(L)₃Fe]²⁺ complexes, where L=bipyridine or phenanthroline, discretely drove assembly structures exhibiting enhanced thermal stability. Also, some supramolecular protein assemblies using the ternary complex (L₁-M-L₂) of nonbiological metal chelating ligands as the connecting node were reported^{51,52}, indicating that utilization of unnatural amino acids can be powerful strategies for generating assembly products that could not be achieved by conventional approaches.

Furthermore, the thermodynamic and kinetic properties of the metal complexes can be easily controlled by differing metal ions, oxidation states, coordinating ligands, secondary coordination sphere, and environmental conditions such as pH, ion adducts, solvents, and temperatures. Controllable and tunable coordination complexes can be designed for directing assembly, affecting the overall structure and chemical/mechanical properties of resulting biomaterials. The advantage of the metal-coordination bond in this perspective is well demonstrated in the study about Zn²⁺-directed protein assembly by the Tezcan Group⁴⁶. They controlled the outcome of assembly by designing two-different metal-binding sites

in a protein and changing environmental conditions such as equivalence or pH. This study well illustrates that tunable metal-binding sites in proteins and variable conditions enable the generation of diverse protein-assembled materials with a singular building block.

1.3. Challenges in designing artificially extended protein assembly

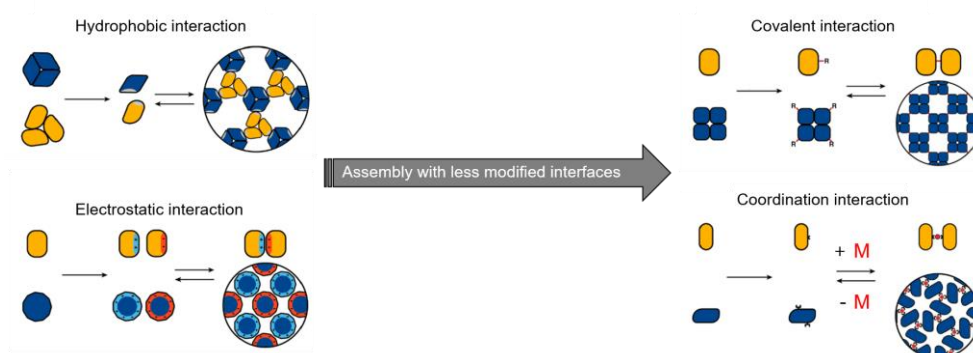


Figure 1.3. Advantages of covalent and coordination interactions over noncovalent interactions for protein assembly design. *Copyright © 2021, American Chemical Society*

Advances in genetic engineering and site-specific chemical modification technologies progressed the field of protein assembly. Various PPI design strategies involving covalent, electrostatic, metal-coordination, host-guest, and hydrophobic interactions are applied to drive the intermolecular self-assembly of proteins. However, from the point of material synthesis, it is obvious that most strategies are only applicable to limited types of proteins. For instance, designing PPI with hydrophobic or electrostatic interactions often requires a lot of mutation on the protein surface to induce assembly as designed (Figure 1.3). This narrows down the scope of building blocks into the proteins stable enough to retain their original structures and functions even with multiple mutations. Also, desired assembly

architectures may require small interfacial contact, indicating that the assembly should progress solely by enthalpy gain. The general PPI design strategies not restricted to some proteins, assembled products, or conditions should be tried to synthesize unprecedented protein-based nanomaterials from diverse types of building blocks.

Proteins, composed of 20 different amino acids, are complex building blocks. The surface residues may disturb selective assembly between designed variants, leading to disordered aggregates. To develop general strategies applicable to broad scopes of building blocks, the PPI design and assembly process should be simple and easily predictable, respectively. For example, coordination bonds or covalent interactions exhibit high thermodynamic stability on a small design footprint. Thus, diverse protein-assembled structures involving 1D, 2D, and finite assemblies could be generated in the same PPI design strategies. Likewise, developing strategies inducing desirable interactions by two or fewer inserted groups can broaden the scopes of usable building blocks.

While the structural goal of protein assembly has been achieved a lot, there are still limits to the further application of artificial biomaterials. Indeed, the great challenge is required to prove that the prospects of artificial protein assembly are not confined to aesthetic perspectives, but these biomaterials can be applied to various fields involving drug delivery, catalysis, electron transfer, and molecular selection systems. The advantages coming from ‘protein’ and ‘assembly’ should be well addressed to illustrate the unique properties and possible applications of protein-assembled materials. In this respect, the PPI design strategies which are orthogonal and compatible with previously reported protein engineering techniques should be tried. Assembly architectures from highly functionalized proteins can harness practical properties such as enhanced stability, and multiple catalytic centers, which makes the biomaterials applicable in various fields.

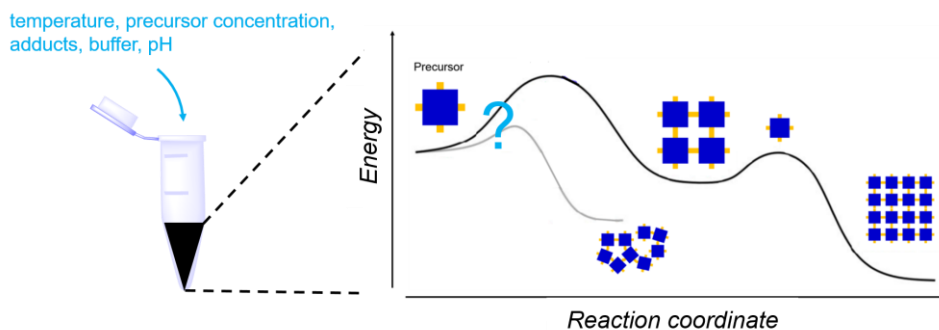


Figure 1.4. Pathway-dependent outcomes in extended assembly.

Compared to intramolecular self-assembly or ‘finite’ assembly, ‘extended’ assembly products can be pathway-dependent. Different environmental conditions can lead to different structural outcomes (Figure 1.4). In nanoscience, the interaction between nanoparticles via strong and short-range order attractive forces normally generates amorphous or small grain boundary-sized structures rather than highly ordered configurations⁵³. The environmental conditions including precursor concentrations, temperature, adducts, buffer, and pH can change the pathway of assembly. While the diverse architectures of proteins are enormously reported, the effect of these environmental factors on assembly mechanism and resultant products is less studied. It is essential to look beyond just design strategy and products. For further applications of investigated strategies, the mechanistic study should be thoroughly studied considering the nature of chemical interactions and the effects of external conditions on thermodynamic/kinetic parameters.

1.4. References

1. W. Weis and K. Drickamer, *Annu. Rev. Biochem.* 1996, **65**, 441.
2. R. Dwek, *Chem. Rev.* 1996, **96**, 683.
3. H. Lis and N. Sharon, *Chem. Rev.* 1998, **98**, 637.
4. H. Ochman, J. G. Lawrence, and E. A. Groisman, *Nature* 2000, **405**, 299.
5. M. G. Caprara and T. W. Nilsen, *Nat. Struct. Biol.* 2000, **7**, 831.
6. I. Chen, P. H. Christie, and D. Dubnau, *Science* 2005, **310**, 1456.
7. T. Lindahl and R. D. Wood, *Science* 1999, **286**, 1897.
8. Y. Jiang, J. Chen, A. Lee, and R. MacKinnon, *Nature* 2003, **423**, 42.
9. E. Perozo, A. Kloda, D. M. Cortes, and B. Martinac, *Nat. Struct. Biol.* 2002, **9**, 696.
10. S. J. Benkovic and S. H. Schiffer, *Science* 2003, **301**, 1196.
11. M. G. Viloca, J. Gao, M. Karplus, and D. G. Truhlar, *Science* 2004, **303**, 186.
12. G. Chang, R. H. Spencer, A. T. Lee, M. T. Barclay, and D. C. Rees, *Science* 1998, **282**, 2220.
13. S. B. Long, E. B. Campbell, and R. Mackinnon, *Science* 2005, **309**, 903.
14. E. Perozo, D. M. Cortes, P. Sompornpisut, A. Kloda, and B. Martinac, *Nature* 2002, **418**, 942.
15. P. A. Janmey, *Curr. Opin. Cell Biol.* 1991, **3**, 4.
16. E. Nogales, *Annu. Rev. Biochem.* 2000, **69**, 277.
17. U. B. Sleytr, B. Schuster, E. M. Egelseer, and D. Pum, *FEMS Microbiol. Rev.* 2014, **38**, 823.
18. M. G. Lopez, M. Diez, V. Alfonso, and O. Taboga, *Appl. Microbiol. Biotechnol.* 2018, **102**, 6765.
19. P. Ozimek, M. Veenhuis, and I. J. van der Klei, *FEMS Yeast Res.* 2005, **5**, 975.
20. N. Huang, P. Wang, and D. Jiang, *Nat. Rev. Mater.* 2016, **1**, 16068.
21. T. D. Bennett, F. X. Coudert, S. L. James, and A. I. Cooper, *Nat. Mater.* 2021, **20**, 1179.

22. A. E. Baumann, D. A. Burns, B. Liu, and V. Sara Thoi, *Commun. Chem.* 2019, **2**, 86.
23. Zhu, N. Avakyan, A. Kakkis, A. M. Hoffnagle, K. Han, Y. Li, Z. Zhang, T. S. Choi, Y. Na, C. J. Yu, and F. A. Tezcan, *Chem. Rev.* 2021, **121**, 13701.
24. B. J. G. E. Pieters, M. B. Eldijk, R. J. M. Nolte, and J. Mecinovic, *Chem. Soc. Rev.* 2016, **45**, 24.
25. C. J. Wilson, A. S. Bommarius, J. A. Champion, Y. O. Chernoff, D. G. Lynn, A. K. Paravastu, C. Liang, M. C. Hsieh, and J. M. Heemstra, *Chem. Rev.* 2018, **118**, 11519.
26. S. Biswas, K. Kinbara, T. Niwa, H. Taguchi, N. Ishii, S. Watanabe, K. Miyata, K. Kataoka, and T. Aida, *Nat. Chem.* 2013, **5**, 613.
27. H. Sun, L. Miao, J. Li, S. Fu, G. An, C. Si, Z. Dong, Q. Luo, S. Yu, J. Xu, and J. Liu, *ACS Nano* 2015, **9**, 5461.
28. J. D. Brodin, J. R. Carr, P. A. Sontz, and F. A. Tezcan, *Proc. Natl. Acad. Sci. USA.* 2014, **111**, 2897.
29. Q. Luo, C. Hou, Y. Bai, R. Wang, and J. Liu, *Chem. Rev.* 2016, **116**, 13571.
30. A. J. Simon, Y. Zhou, V. Ramasubramani, J. Glaser, A. Pothukuchy, J. Gollihar, J. C. Gerberich, J. C. Leggere, B. R. Morrow, C Jung, S. C. Glotzer, D W. Taylor, and A. D. Ellington, *Nat. Chem.* 2019, **11**, 204.
31. J. Ge, J. Lei, and R. N. Zare, *Nat. Nanotechnol.* 2012, **7**, 428.
32. S. Gonen, F. DiMaio, T. Gonen, and D. Baker, *Science*, 2015, **348**, 1365.
33. H. Shen, J. A. Fallas, E. Lynch, W. Sheffler, B. Parry, N. Jannetty, J. Decarreau, M. Wagenbach, J. J. Vicente, J. Chen, L. Wang, Q. Dowling, G. Oberdorfer, L. Stewart, L. Wordeman, J. D. Yoreo, C. J. Wagner, J. Kollman, D. Baker, *Science* 2018, **362**, 705.
34. Y. Suzuki, G. Cardone, D. Restrepo, P. D. Zavattieri, T. S. Baker, and F. A. Tezcan, *Nature* 2016, **533**, 369.
35. S. E. Boyken, Z. Chen, B. Groves, R. A. Langan, G. Oberdorfer, A. Ford, J. M. Gilmore, C. Xu, F. D. Maio, J. H. Pereira, B. Sankaran, G. Seelig, P. H. Zwart, D. Baker, *Science* 2016, **352**, 680.

36. Z. Chen, M. C. Johnson, J. Chen, M. J. Bick, S. E. Boyken, B. Lin, J. J. De Yoreo, J. M. Kollman, D. Baker, and F. DiMaio, *J. Am. Chem. Soc.* 2019, **141**, 8891.
37. J. D. Brodin, X. I. Ambroggio, C. Tang, K. N. Parent, T. S. Baker, and F. A. Tezcan, *Nat. Chem.* 2012, **4**, 375.
38. S. Biswas, K. Kinbara, N. Oya, N. Ishii, H. Taguchi, and T. Aida, *J. Am. Chem. Soc.* 2009, **131**, 7556.
39. Y. Bai, Q. Luo, W. Zhang, L. Miao, J. Xu, H. Li, and J. Liu, *J. Am. Chem. Soc.* 2013, **135**, 10966.
40. R. P. Bahadur, P. Chakrabarti, F. Rodier, and J. A. Janin, *J. Mol. Biol.* 2004, **336**, 943.
41. Biological Inorganic Chemistry -Structure & Reactivity, ed. I. Bertini, H. B. Gray, E. I. Stiefel and J. S. Valentine, University Science Books, Sausalito, 2007.
42. S. J. Lippard and J. M. Berg, Principles of Bioinorganic Chemistry, University Science Books, Mill Valley, 1994.
43. E. N. Salgado, R. A. Lewis, S. Mossin, A. L. Rheingold, and F. A. Tezcan, *Inorg. Chem.* 2009, **48**, 2726.
44. Y. Bai, Q. Luo, W. Zhang, L. Miao, J. Xu, H. Li and J. Liu, *J. Am. Chem. Soc.* 2013, **135**, 10966.
45. S. Burazerovic, J. Gradinaru, J. Pierron, and T. R. Ward, *Angew. Chem. Int. Ed.* 2007, **46**, 5510.
46. J. D. Brodin, X. I. Ambroggio, C. Tang, K. N. Parent, T. S. Baker, and F. A. Tezcan, *Nat. Chem.* 2012, **4**, 375.
47. R. H. Subramanian, S. J. Smith, R. G. Alberstein, H. b. Bailey, L. Zhang, G. Cardone, L. Suominen, M. Chami, H. Stahlberg, and T. S. Baker, *ACS cent. Sci.* 2018, **4**, 1578.
48. E. N. Salgado, J. F. Mennella, and F. A. Tezcan, *J. Am. Chem. Soc.* 2007, **129**, 13374.
49. C. C. Broomell, H. Birkedal, C. L. P. Oliveira, J. S. Pedersen, J. A. Gertenbach, M. Young and T. Douglas, *Soft Matter*, 2010, **6**, 3167.

50. J. H Mills, W. Sheffler, M. E. Ener, P. J. Almhjell, G. Oberdorfer, J. H. Pereira, F. Parmeggiani, B. Sankaran, H. Zwart, and D. Baker, *Proc. Natl. Acad. Sci. U. S. A.* 2016, **113**, 15012.
51. R. J. Radford and F. A. Tezcan, *J. Am. Chem. Soc.* 2009, **131**, 9136.
52. N. A. Tavenor, M. J. Murnin, and W. S. Horne, *J. Am. Chem. Soc.* 2017, **139**, 2212.
53. K. J. M. Bishop, C. E. Wilmer, S. Soh, and B. A. Grzybowski, *Small* 2009, **5**, 1600.

Chapter 2. Diverse protein assembly driven by metal and chelating amino acids with selectivity and tunability

* Part of this chapter was reprinted with permission from M.W. Yang; W.J. Song,
Nat. Commun., 2019, 10, 5545, copyright 2019, Springer Nature.

2.1. Introduction

Here, we report the assembly of symmetric protein by a single mutation of interfacial amino acids into Bipyridinyl alanine (Bpy-Ala)¹. Bipyridine (Bpy) is a bidentate chelate ligand that can bind transition metal much stronger than monodentate ligands², thus providing enough binding energy for assembly with even a single mutation at the interface. Bpy is also one of the most studied ligands, thus, the binding constants and kinetics between Bpy and 1st-row transition metals in an aqueous solution are well known³. We thought the use of the bipyridine group can simplify the protein assembly system into a well-studied polymerization process of organic-based coordination polymers. Also, orthogonal mutation to unnatural amino acids is less dependent on building block types, and complementary with natural amino acids, representing that this approach can be a general method for assembly and applications.

By mutation of one amino acid in the monomeric unit of hexameric D₃ protein, acetyltransferase from *Bacillus anthracis* (PDB code: 3N7Z)⁴, we could generate mutant proteins with totally of 6 Bpy groups as a building block. The addition of metal caused the formation of designed assembly structures, and the assembly mechanism was thoroughly studied. By controlling the type of mutant proteins and metals, concentration, temperature, stoichiometry, adducts, and even solvents, we modulated the polymerization process of our systems to yield our desired 1-, 2-dimensional structures and their hierarchical structures, illustrating that our approach is highly controllable and applicable method in generating diverse protein-based materials.

2.2. Design strategy

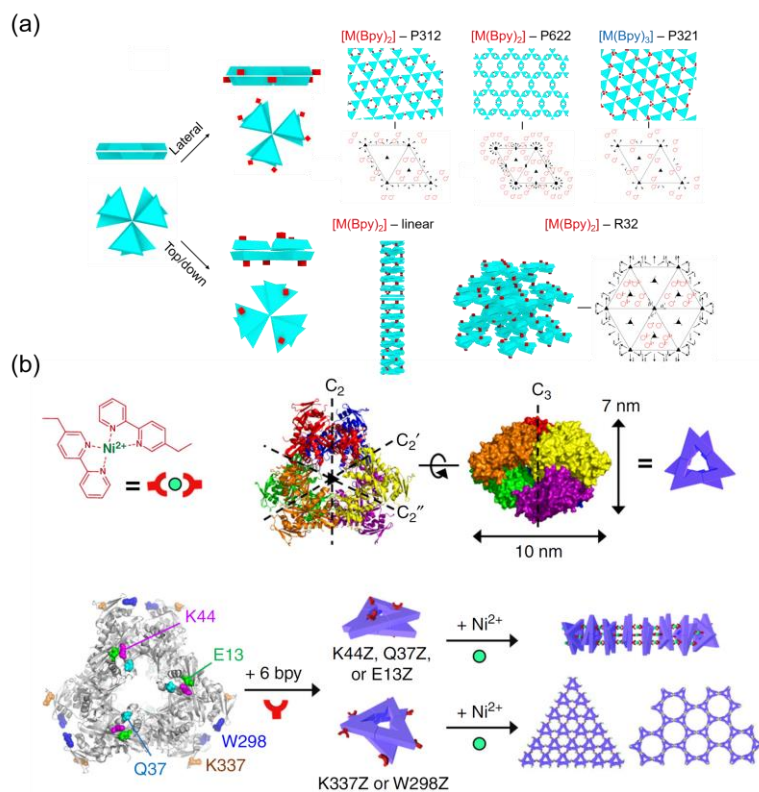


Figure 2.1. Illustration of assembly strategy. (a) Proposal assembly structures with D_3 symmetry protein as a building block (b) Structures of 3N7Z and our target assembly structures.

We proposed that the appropriate location of mutation site could drive assembly of homohexameric D_3 protein into 1- and 2-dimensional structures. D_3 proteins have not been used as a building block in symmetry-adapted assembly of protein. Depending on mutation site, 1-dimensional assembly, 2-dimensional (p312, p321, p622) and 3-dimensional (R32) structures can be constructed (Figure 2.1a). We planned to generate 1-dimensional linear assembly by inserting bipyridine at the top-bottom side of proteins, and 2-dimensional assembly, especially structures with p312, and p622 space group symmetry by mutation to bipyridine at the lateral side of proteins (Figure 2.1b).

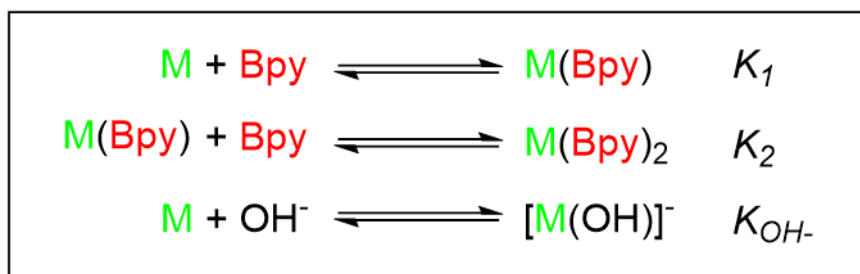
Our desired structures can be generated only by inducing $[(Bpy)_2M]$

complex formation, and sorts of building blocks and metal ions were considered to repress mono- or trisbipyridyl metal complexes formation (Figure 2.1b). Among D₃ proteins recorded in RCSB, we selected acetyltransferase from *Bacillus anthracis* (PDB code: 3N7Z) as a building block due to its potential possibility to adopt multiple assembly modes depending on mutation sites. Also, careful consideration of unnatural amino acid encoding location in 3N7Z can lead to the formation of our desired assembled structures by suppressing [(Bpy)₃M] complex formation owing to steric hindrance between building blocks.

The equilibrium towards ternary complex, [M(Bpy)L], where L is buffer derived species, such as H₂O, Cl⁻, OH⁻, would interrupt the generation of our desired structures. To resolve this issue, we considered thermodynamic equilibrium constants of kinetically reversible 1st-row transition metals (Fe²⁺, Co²⁺, Ni²⁺, Cu²⁺, Zn²⁺) towards bipyridine in an aqueous solution (Table 2.1). Equilibrium constants of monobipyridinyl and bisbipyridinyl complexes formation are represented as log K_1 and log K_2 values, and summation values (Log K_1K_2) between each metal ion were compared to confirm proper metal ion for inducing Bisbipyridinyl metal complexes³. In this regard, both Ni²⁺ ion and Cu²⁺ ion satisfy the above condition, however, low log K_2 value of Cu²⁺ ion compared to log K_1 value would shift the equilibrium toward monobipyridine complex. Not only that, the high K_{OH^-} value of Cu²⁺ ion, indicative of high affinity towards oxygen donating ligands, represents that chemical equilibrium would be shifted towards ternary complex formation⁵. Furthermore, Ni²⁺ ion has a rather small K_{OH^-} value, concluding that our desirable structure can be formed by Ni²⁺ ion with high probability. For more selective interaction between metal and bipyridine, high concentration of NaCl or LiCl was also added to screen out electrostatic binding between Ni²⁺ ion and free carboxyl groups⁶.

M ²⁺	Log K ₁	Log K ₂	Log K _{OH-}
Mn ²⁺	4.06	3.78	3.4
Co ²⁺	5.65	5.60	4.3
Ni ²⁺	7.07	6.86	4.1
Cu ²⁺	8.15	5.50	6.3
Zn ²⁺	5.04	4.35	5.0

Table 2.1. Equilibrium constants of 1st-row transition metals for bipyridine (mono- and bisbipyridinyl complexes) and hydroxide ion.



Scheme 2.1. A series of reactions related to protein-assembly using bpy ligand. K_1 , K_2 , and K_{OH^-} indicate the chemical equilibrium constants for Equation (1) - (3), respectively.

2.3. 1-Dimensional assembly design

We first designed K44Z by introducing bipyridine ligands on the top/bottom sides of protein to generate 1-dimensional assembly. The ideal stoichiometric ratio of protein and metal ion for full conversion of free ligand to $[\text{Ni}(\text{Bpy})_2]$ complex requires the 3 equivalents of Ni^{2+} to 1 equivalent of homohexameric protein. The addition of stoichiometric amounts of metal ions to the protein-buffer solution (50 mM Tris-HCl, 150 mM NaCl, 10 μM hexamer, pH 7.4 at 25 $^\circ\text{C}$) made no vivid change in transparency and color, indicating that aggregates-like species were not formed. Negatively stained transmission electron microscope (TEM) images showed that linearly arrayed repeating units formed rod-shaped species (Figure 2.2a). The thickness of a single protofilament fits with the diameter of the building block, 10 nm, indicating that selective interaction between Ni^{2+} and Bpy only acts to form linearly assembled products without any disrupting pathway. Atomic force microscopy also demonstrates that the thickness of 1D-assembled materials coincides with the size of a building block (Figure 2.2b). The average length (L_n) and the maximum length of the samples were about 0.28 and 1.6 μm , respectively with a 2.08 of polydispersity index (PDI) value (Figure 2.2c).

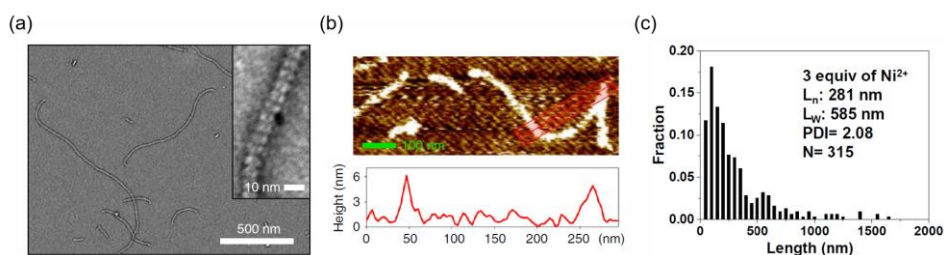


Figure 2.2. Assembled structures of K44Z (10 μM) with 3 equiv. of Ni^{2+} at 22 $^\circ\text{C}$. (a) TEM and (b) AFM images of 1D-assembled K44Z, and (c) length distributions characterized by TEM images.

Stoichiometric amounts of other transition metal ions such as Co^{2+} , Cu^{2+} , and Zn^{2+} were also mixed with K44Z to confirm that the protein assembly is created under our thoroughly controlled thermodynamic conditions (Figure 2.3). These ions could not generate 1D-assembled materials with enough length, as proposed by their low $\log K_2$, or $\log K_1K_2$ values. The addition of strong metal chelator, ethylene diamine tetraacetic acid (EDTA), to 1D rods caused shortening of nanorods. Alternatively, when one of the other metal ions listed above after or together with Ni^{2+} , extremely shorter rods were formed compared to when Ni^{2+} ions alone were added, indicating that metal binding and subsequent protein assembly process is kinetically reversible (Figure 2.4).

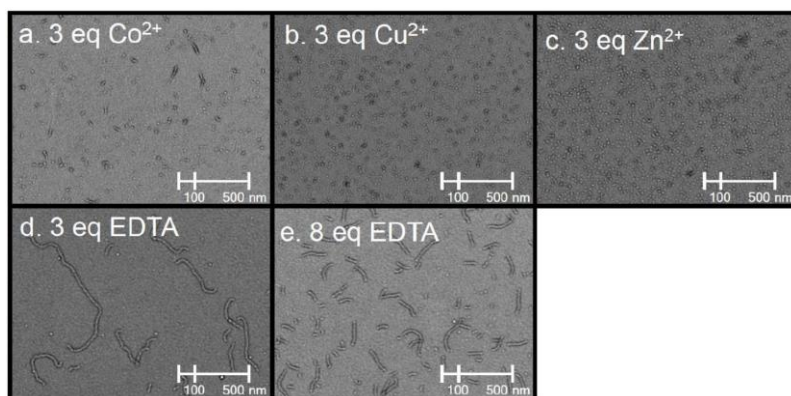


Figure 2.3. Metal-dependent 1D-rod formation with K44Z. TEM images of K44Z ($10 \mu\text{M}$) with various metal ions (3 equiv.) at $22 \text{ }^\circ\text{C}$ for 24 h. Excess EDTA (3 or 8 equiv.) was added to the pre-formed rod with Ni^{2+} for 24 h at $37 \text{ }^\circ\text{C}$.

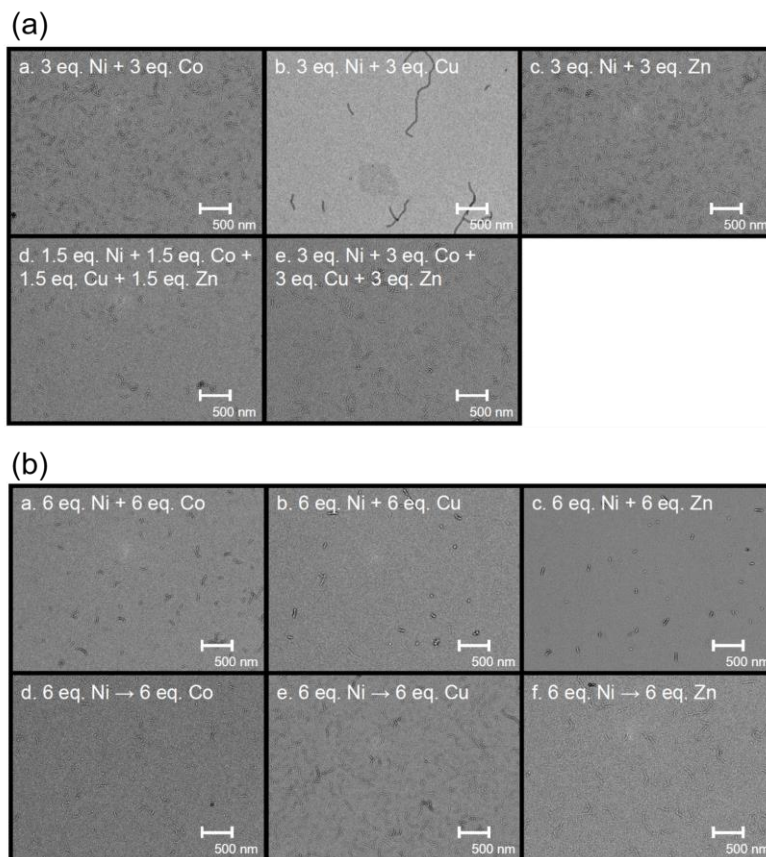


Figure 2.4. TEM images of K44Z-linear assembly of with the mixtures of metal ions. (a) TEM images of K44Z (10 μ M) incubated with more than one divalent metal ions together for 24 h at 37 $^{\circ}$ C. (b) TEM images of K44Z (10 μ M) upon the addition of metal ions in simultaneous (top) or sequential (bottom) manners.

Lower amounts of NaCl or LiCl lead to less assembled structures, presumably due to decreased degree of masking electrostatic interactions between Ni^{2+} and anions in solution (Figure 2.5). In the same way, reactions in solutions at higher pH values yielded less assembled structures (Figure 2.6). The result in pH 6 buffer is attributed to intrinsic protein instability, represented by aggregates formation without metal ion addition. These data conclude that proper selection of salts and metal ions enabled them to interact reversibly to construct desired $[\text{Ni}(\text{Bpy})_2]$ complexes and consequent assembled structures.

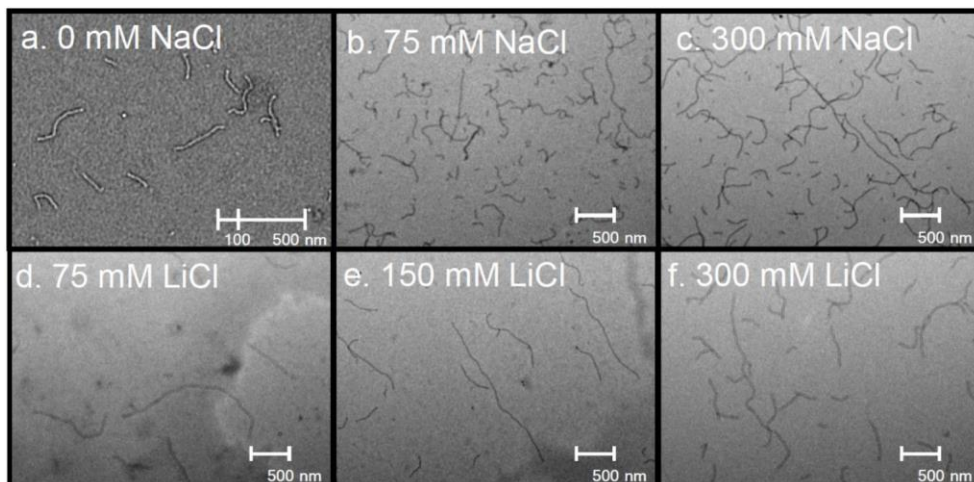


Figure 2.5. TEM images of K44Z (10 μM) reacted with Ni²⁺ with variations of salt concentration. (a) 3 equiv Ni²⁺ at 22 °C, b–f: 8 equiv Ni²⁺ at 37 °C for 24 h with [NaCl] or [LiCl] = 0–300 mM.

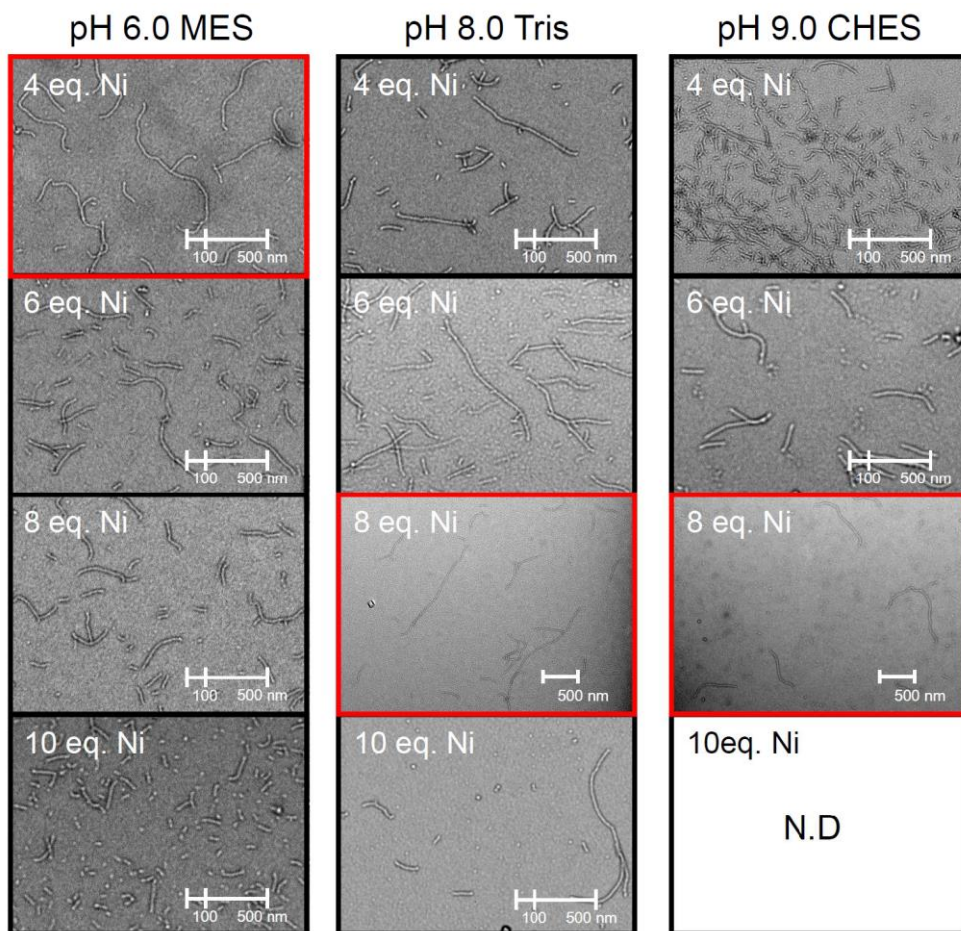


Figure 2.6. Formation of K44Z-derived rods at various pH condition. K44Z (7.5 μM) and the various concentrations of Ni^{2+} were incubated in pH 6–9 buffers (50 mM MES pH 6, 50 mM Tris at 7–8, 50 mM CHES pH 9) at 37 $^{\circ}\text{C}$. The optimal ratios of Ni^{2+} to the protein were marked with red boxes for each pH condition.

Wide range of stoichiometries, temperature, and protein concentration was applied to tune and explore the metallopolymerization process by altering the kinetic or thermodynamic factors operative in the reactions. We examined the length of nanorods in the TEM image at each condition to characterize degrees of $[\text{Ni}(\text{Bpy})_2]$ complex formation and consequent polymerizations. At 4 $^{\circ}\text{C}$, the average length of the nanorods reached its maximum when the amount of Ni^{2+} was added with its ideal stoichiometric value (Figure 2.7a and Appendix 2.1).

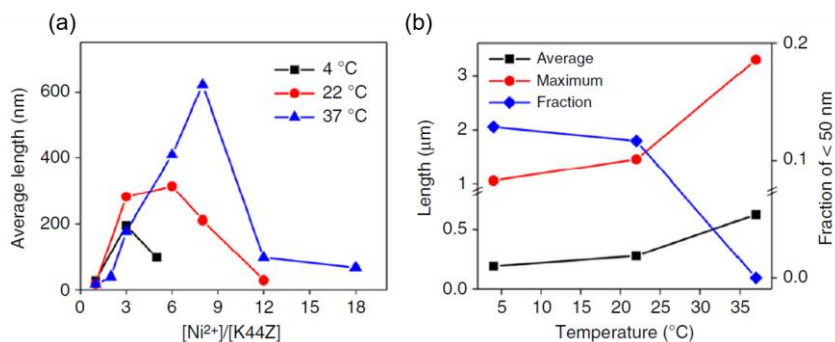


Figure 2.7. Optimization of K44Z-rod formation. (a) Various ratios of Ni²⁺ to K44Z (10 μM) at 4–37 °C. (b) Reaction of K44Z (10 μM) and the optimal Ni²⁺ at a given temperature.

The addition of greater than 3 equiv. of Ni²⁺ lead to shortening the length, presumably because the equilibrium shifts from bisbipyridinyl to monobipyridinyl species. When metal equivalent dependent length control was also conducted at higher temperatures, an analogous tendency was observed except for the optimal equivalent of metal ions were 6, and 8 at 22 °C and 37 °C, respectively (Figure 2.7a and Appendix 2.2 and 2.3). As illustrated in figure 2.7b, at optimal Ni²⁺ stoichiometry condition, the average and maximum lengths of nanorods are calculated to be longer, and the fraction of species less than 50 nm becomes lower when higher temperature conditions were applied (4 to 37 °C). These results suggest that the thermodynamic equilibrium or rates of metal complex formation were altered under the temperature changes.

Initial metal binding to metal-free bipyridine is a thermodynamically exothermic and kinetically fast process. The Ni²⁺ coordination to the ligand in K44Z was monitored by time-dependent ultraviolet-visible (UV-Vis) spectroscopy, which indicates absorption changes at 280 and 312 nm with an isosbestic point at 295 nm by the addition of Ni²⁺ (Figure 2.8a)⁷. The Ni²⁺ binding was completed in about 20 s. However, when time-dependent molecular weight changes were observed with size exclusion chromatography (SEC), the polymerization process proceeded for 24 h, indicated by continual changes of elution profiles in the SEC

graph as time passes (Figure 2.8b).

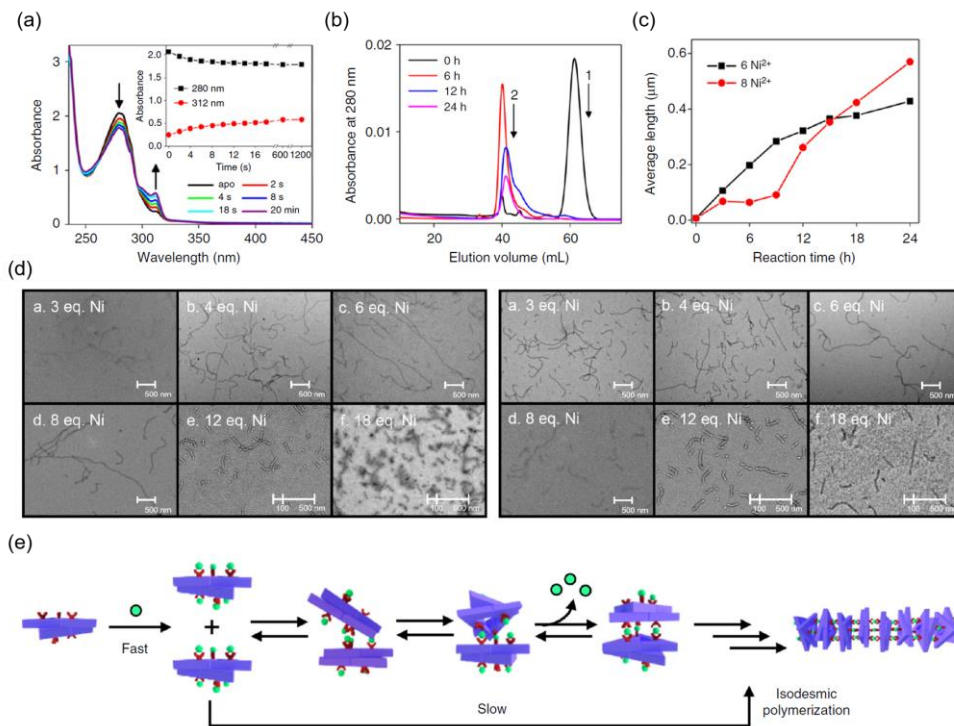


Figure 2.8. Kinetics of 1D-rod formation. (a) Optical spectral changes upon the addition of Ni²⁺ to K44Z at 22 °C. Inset: Time-dependent absorbance at 280 and 312 nm. (b) Elution trace of K44Z incubated with Ni²⁺ (3 equiv.) at 22 °C for 0-24 h from S200 column. The sequential order of the reactions was labeled. (c) Time-dependent rod-growth with K44Z (5 μM) at 37 °C monitored by TEM. (d) K44Z (10 μM) were incubated with various concentrations (left) 43 °C and (Right) 49 °C. No rod formation was observed at 55 °C (not shown). (e) A proposed scheme for 1D assembly.

Not only that, we compared time-dependent average length changes of K44Z between 6 equiv. and 8 equiv. Ni²⁺ addition conditions (Figure 2.8c, Appendix 2.4 and 2.5). The reaction was monitored for every 3 h by TEM, and the average length was calculated from each image. Assembly with smaller equiv. of Ni²⁺ is much faster at first, however, the 8 equiv. condition yielded longer species at the end of the reaction (24 h). These data indicate that even though saturated binding of Ni²⁺ would slow down the rate of [Ni(Bpy)₂] complex formation and resulting protein assembly, this process, in the end, becomes thermodynamically and kinetically favorable with the high-temperature condition to yield well-

assembled structures. The bimolecular reaction between two [Ni(Bpy)] species is an endothermic and kinetically slow process that requires dissociation of bound Ni²⁺ ion. Thus, high-temperature condition with excess metal than stoichiometric amount can shift the equilibrium from monobipyridinyl complex to bisbipyridinyl complex. The high-temperature condition also provides enough energy for elevating the mobility of macromolecules and, especially overcoming the rate-determining dissociation step, which results in accelerating the reaction rate. Further elevated temperature conditions, 43 and 49 °C, however, did not yield much longer assembled structures presumably due to intrinsic instability of the protein and metal complex itself (Figure 2.8d). Entropic effects caused by releasing of hydrated water molecules by creating protein-protein interfaces might influence the self-assembly of macromolecules⁸. The dependency of optimal condition and its degrees of polymerization on temperature cannot be attributed to a firm and discrete reason, rather may originate from the orchestration of both kinetic and thermodynamic factors. However, we could conclude, from our experimental data, that the mechanism of metallopolymerization is likely to be isodesmic polymerization where metal binding and polymerization occur in solution as a whole simultaneously⁹ (Figure 2.8e).

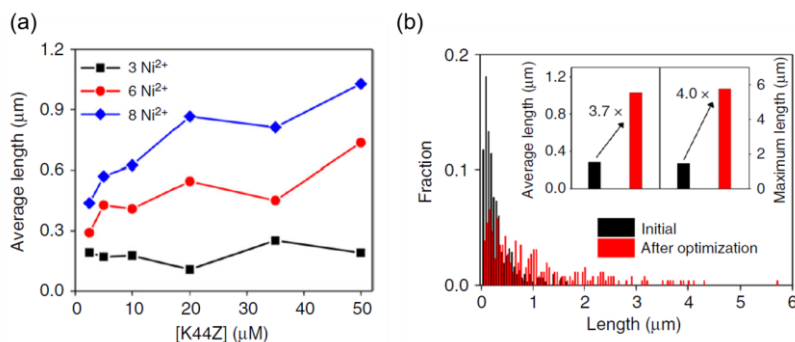


Figure 2.9. Concentration dependency of assembly at 37 °C and changes in distributions, average lengths, and maximum lengths of assembled structures after condition optimization. (a) Variations in the protein concentrations at 37 °C. (b) The length in Figure 2.2 a (black) and after optimization (red); K44Z (50 μM) and 8 equiv. Ni²⁺ (8 equiv.) at 37 °C. The average lengths (L_n) were determined by measuring 315 (PDI = 2.08) and 258 (PDI = 1.89) rods formed at the initial condition and after optimization, respectively.

The effect of protein concentration on the length of the rods was also investigated. Based on the optimal conditions described above, 2.5 to 50 μM of proteins were incubated with 3, 6, and 8 equiv. of Ni²⁺ ions for 24 h at 37 °C (Figure 2.9a, Appendix 2.6 to 2.8). At 6 and 8 equiv. conditions, higher concentration of protein condition yielded assembled products with longer average length due to intermolecular collision rate. However, this tendency was not observed when 3 equiv. of metal ions were added, indicating that the protein concentration is not a determining factor in polymerization at a given condition. Finally, when the conditions described above were all optimized, the K44Z protein assembly was observed to have 1.0 μm on average length and up to 5.8 μm as the maximum length with maintaining its single protein diameter (Figure 2.9b). The possibility of thorough study of the assembly mechanism and consequences of predictable, tunable, and uniform products demonstrate that adopting chelating ligands, bipyridine, can be a general and powerful method to drive the formation of the 1D protein assembly successfully.

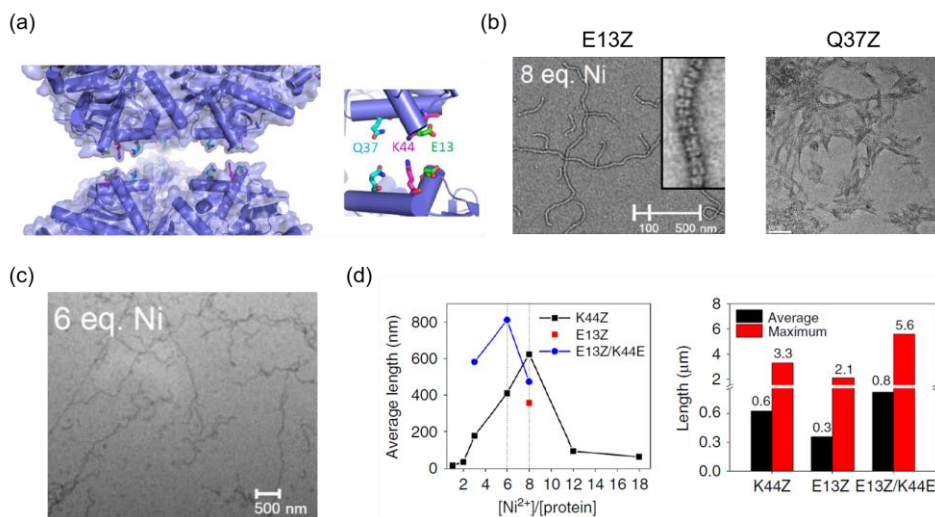


Figure 2.10. Tunability of metal binding sites and changes in assembly aspects. (a) Position of Q37Z relative to K44 and E13 residues. (b) TEM images of 1D-rods from the reactions of E13Z (10 μM) and Ni^{2+} (8 equiv.) at 37 $^{\circ}\text{C}$. (c) TEM images of Q37Z (50 μM) with 3 equiv. of Ni^{2+} at 22 $^{\circ}\text{C}$ for 24 h (Scale bar: 50 nm). (d) Formation of 1D-rods with E13Z/K44E and Ni^{2+} . (e) Optimization of Ni^{2+} ratios to the protein. The average and maximum lengths from each variant are represented when the ratio of Ni^{2+} to protein is optimized.

Other variants were also designed for 1D-assembly to demonstrate our strategy is not limited to specific locations (Figure 2.10a). The reaction of E13Z with Ni^{2+} yielded 1D-assembled structures analogous to, but shorter than, those formed with K44Z, while Q37Z generated only aggregated species (Figure 2.10b). The discrete difference between mutants is presumably due to the location of mutation sites. Q37Z is located in a concave region of proteins, causing substantial steric hindrance between building blocks for $[\text{Ni}(\text{Bpy})_2]$ complex formation. E13 is placed right next to the positively charged residue K44, which may perturb the formation of positive ionic metal complex, $[\text{Ni}(\text{Bpy})_2]^{2+}$. To control the degrees of assembly by changing the coordination environment of E13Z, positively charged K44 was mutated to glutamate, preparing the E13Z/K44E mutant. Upon the addition of Ni^{2+} , the mutant generated linearly assembled products which are even longer than the K44Z-derived ones when the assembly condition was optimized (Figure 2.10c and 2.10d, Appendix 2.9 and 2.10).

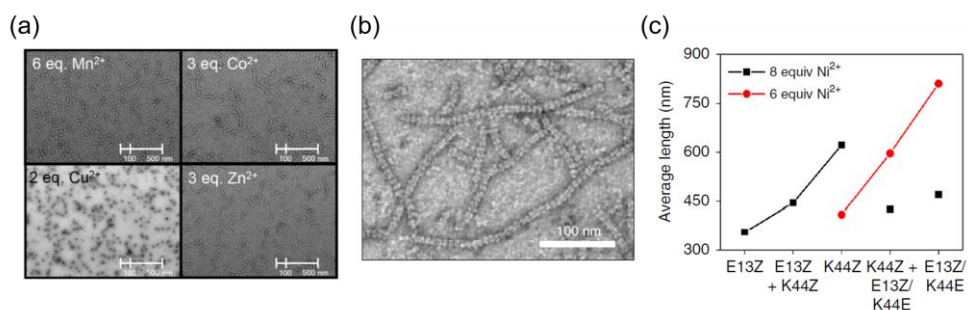


Figure 2.11. Effects of mutations in metal binding sites on metal selectivity. (a) TEM images of E13Z/K44E reacted with other divalent metal ions. (b) TEM images of pre-mixed K44Z and E13Z/K44E (5 μ M each) with 6 equiv. of Ni²⁺ at 37 °C. (c) The average length of rods formed with various variants when 6 (red spheres) or 8 equiv. (black squares) of Ni²⁺ were applied.

Interestingly, although assembly with Ni²⁺ still yielded the most lengthened products, E13Z/K44E variant generated linearly assembled products with other divalent metal ions such as Mn²⁺, Co²⁺, and Zn²⁺, which could not generate 1D-assembly with K44Z mutant (Figure 2.11a). This implies that E13Z/K44E have a coordination environment more favorable for the formation of [M(Bpy)₂] species, indicating that our design has tunability for assembly with additional mutations or metal substitution. These three variants, E13Z/K443, K44Z, and E13Z, have the common location of mutation sites, and 1D-assembled structures could be formed even when the mutants coexisted in solution. When two rod-forming variants were mixed at equal ratios, and Ni²⁺ ions were added, nanorods, which are analogous to those from single kind of mutant protein, were formed. Notably, the average length of optimized assembled rods from mixed samples appeared as the median value of the average length of nanorods made from each mutant (Figure 2.11b and 2.11c, Appendix 2.11). These results indicate that two discrete variants can also generate self-assembled products through a molecular connector of [Ni(Bpy)₂].

2.4. 2-Dimensional assembly design

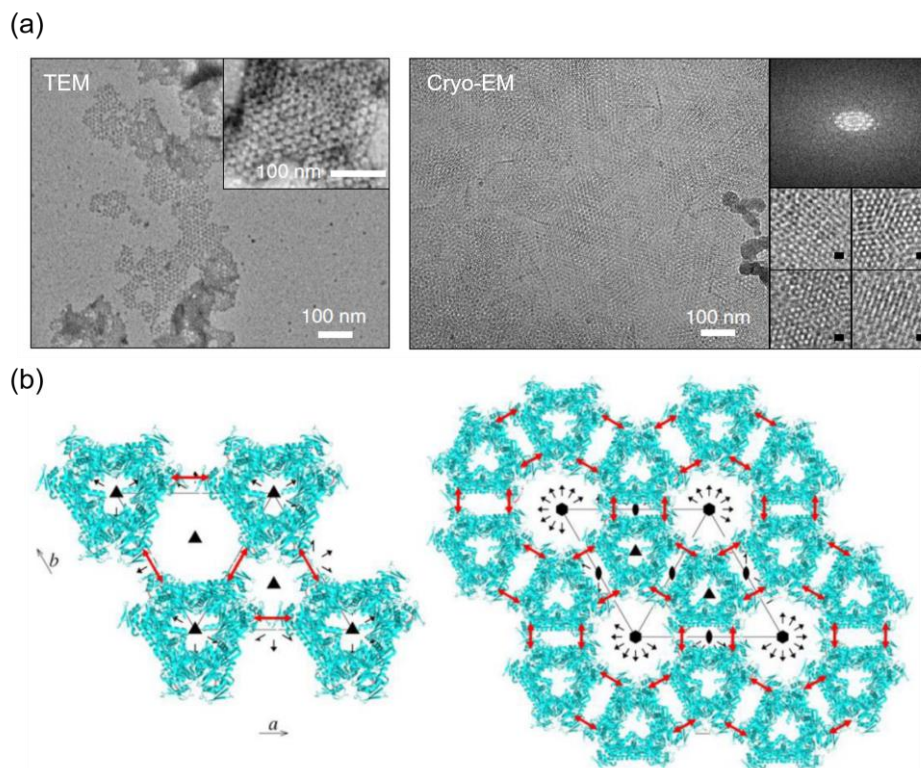


Figure 2.12. Experimental and plausible 2-D assembled structures of K337Z variant with Ni^{2+} . (a) TEM and cryo-TEM images of K337Z (5–10 μM) incubated with 6 equiv. Ni^{2+} at 37 $^{\circ}\text{C}$ for 24 h. (b) Two potential layer symmetries assembled with the D3 protein: p312 (left) and p622 (right).

The addition of Ni^{2+} to mutant whose inserted bipyridine is at the lateral location, K337Z, formed opaque colloidal suspension. TEM and cryo-TEM images of K337Z colloids demonstrate that highly crystalline 2D sheets with layer symmetry of p312 were formed (Figure 2.12a, Appendix 2.12 and 2.13). As presented in figure 2.12b, K337Z can be assembled into two different structures, p312 and p622, through $[\text{Ni}(\text{Bpy})_2]$ complex formation, however, only the p312 structure was generated.

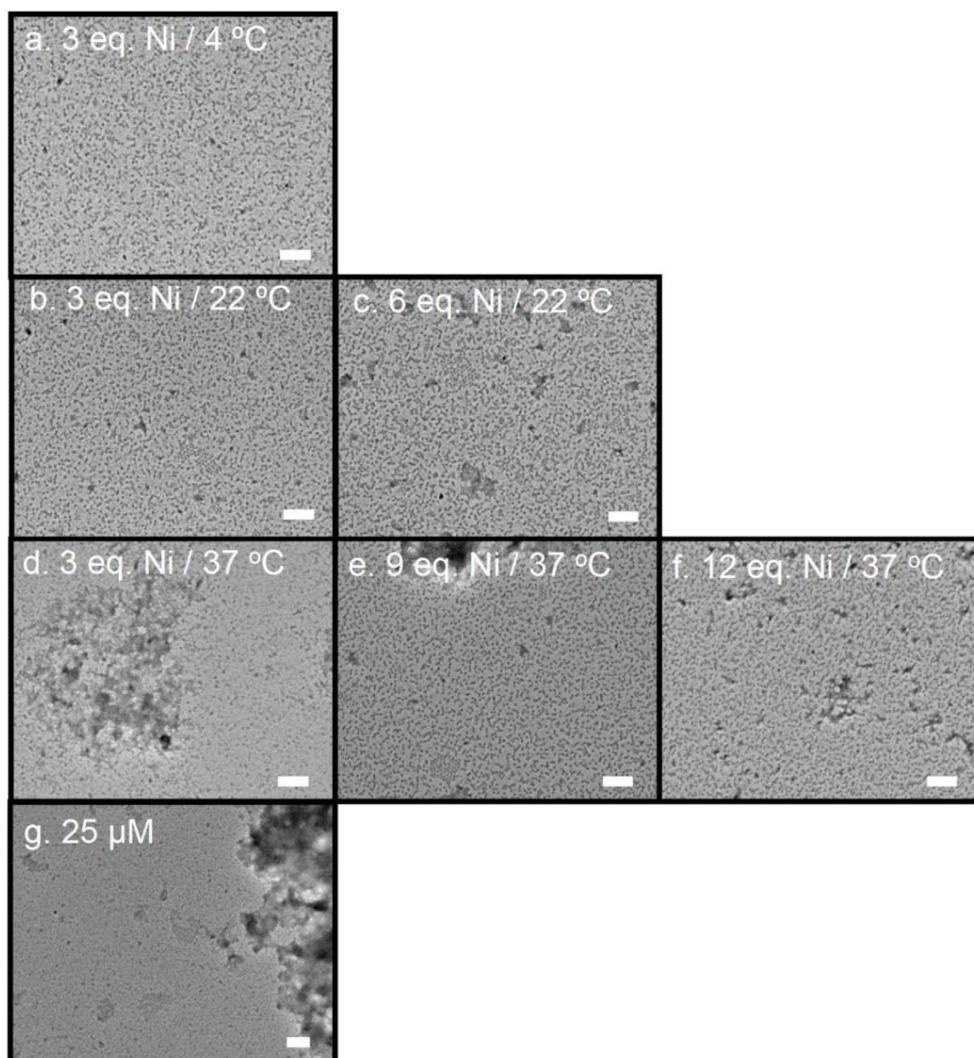


Figure 2.13. TEM images of 2D-planes under various conditions. [K337Z] = 5–10 μM reacted with (a) 3 equiv. of Ni^{2+} at 4 $^{\circ}\text{C}$ (b–c) 3–6 equiv. of Ni^{2+} at 22 $^{\circ}\text{C}$ (d–f) 3–12 equiv Ni^{2+} at 37 $^{\circ}\text{C}$ (g) [K337Z] = 25 μM mixed with 6 equiv. of Ni^{2+} at 37 $^{\circ}\text{C}$ (Scale bar: 100 nm).

To characterize this preference of K337Z for symmetry p312 than p622, we screened the reaction conditions of the formation of the 2D crystalline products by altering reaction temperature, stoichiometry, and protein concentration (Figure 2.13). Although the stacking interaction between planes interrupts the exact estimation of sizes of individual planes through TEM, we concluded that desirable structures were generated only under very narrow conditions; incubation of 5-10 μM mutant with 6 equiv. of Ni^{2+} at 37 $^{\circ}\text{C}$ for 24 h. This sharply contrasted with the

1D assembly process, implying that kinetic parameters should be thoroughly controlled for generating highly crystalline materials.

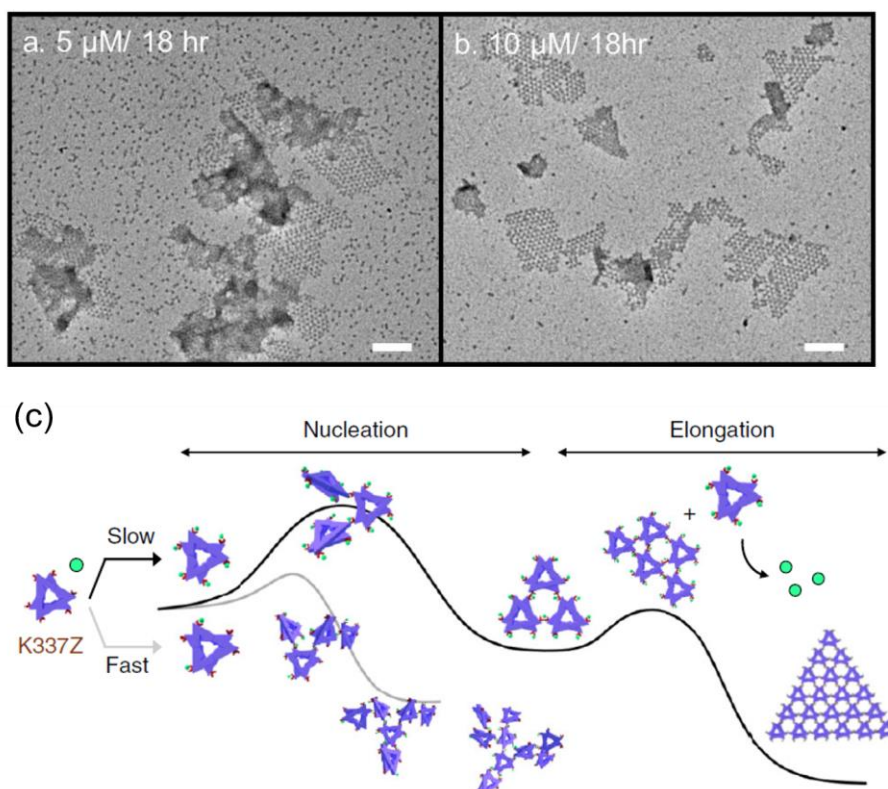


Figure 2.14. Kinetics of 2D assembly. TEM images of K337Z-derived planes formed in 18 h. (a) 5 μM (b) 10 μM of K337Z proteins. Considerable amounts of unreacted monomers were observed in (a). In contrast, no significant difference in the distribution of the monomers was observed in (b) (Scale bar = 100 nm) (c) A proposed scheme for two-directional protein assembly.

We further collected time-dependent TEM images of the 2D material formation process by K337Z (5 μM) and 6 equiv. of Ni^{2+} ions (Figure 2.14a and b). At 18 h, crystalline domain formed, but still substantial amounts of unreacted building units remained, which were then completely consumed after 6 h incubations. This indicates that a two-step process involving a slow nucleation process followed by fast elongation step is essential for the generation of highly crystalline 2D materials. The nucleation step for p312 generation requires the assembly of 3 building units, whereas 6 units are required for nucleation for p622,

indicating that nucleates for p312 could be constructed with a much higher probability. Not only that, elongation for p312 is an energetically more favorable step due to additional nodes than the nucleation step, which is different from propagation in p622 generation, also suggesting the reason for preference of p312 over p622 structure. In summary, as illustrated in figure 2.14c, slow nucleation caused by excess metal ions suppressed the formation of kinetically trapped species, and only at elevated temperatures, elongation could be occurred via reactions between two [Ni(Bpy)] complexes to yield crystalline products. Other conditions which could not satisfy the above factors yielded only amorphous products, suggesting that thorough interplay of kinetic and thermodynamic parameters is essential for crystalline product generation.

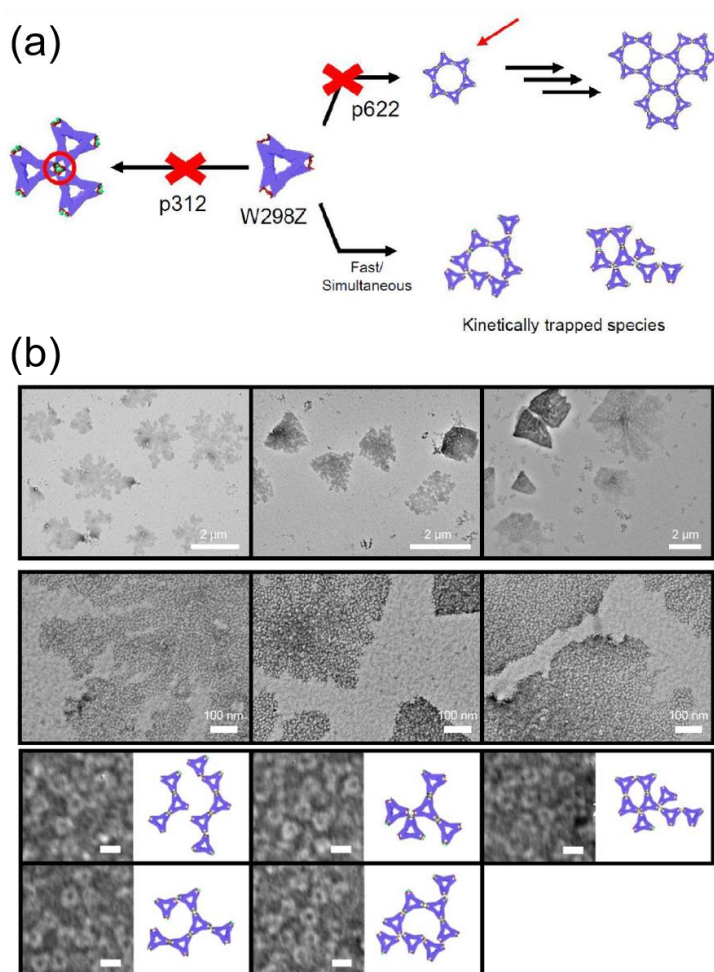


Figure 2.15. Formation of noncrystalline 2D-materials with W298Z with Ni^{2+} . (a) A scheme for 2D-spatial arrangements. Due to the relative location of W298Z, p312 is likely to be disfavored due to the resulting steric hindrance. p622 might be kinetically unfavored, due to the complex nucleation step. (b) TEM images of W298Z protein (5-10 μM) with 10 equiv. of Ni^{2+} at 22 °C. Only kinetically accessible, fractal-shaped 2D-structures were obtained. (Scale bar = 10 nm)

We also designed another mutant whose mutation site is lateral, W298Z, to construct a p622 geometric assembly. Unlike K337Z, W298Z can only generate p622 geometry through $[\text{Ni}(\text{Bpy})_2]$ complex formation as strong steric hindrance at protein-protein interfaces could interrupt the structures with p312 symmetry (Figure 2.15a). The addition of Ni^{2+} to the W298Z-buffer solution yielded aggregated species, which were characterized by TEM to be multibranch

amorphous species similar to K337Z's kinetically trapped species (Figure 2.15b, Appendix 2.14). As discussed above, nucleation for p622 requires high activation energy. As a result, the W298Z protein formed only partial p622-like noncrystalline architectures with irregularities and heterogeneity¹⁰. Notably, two discrete amorphous p622 and crystalline p312 could be generated depending on the mutation site of the Bpy group despite the same driving force for protein assembly, representing that diverse architectures other than those presented here can be constructed by shifting the insertion site of bipyridine due to its easily switchable and predictable characteristics.

2.5. Generation of combinatory and hierarchical structures

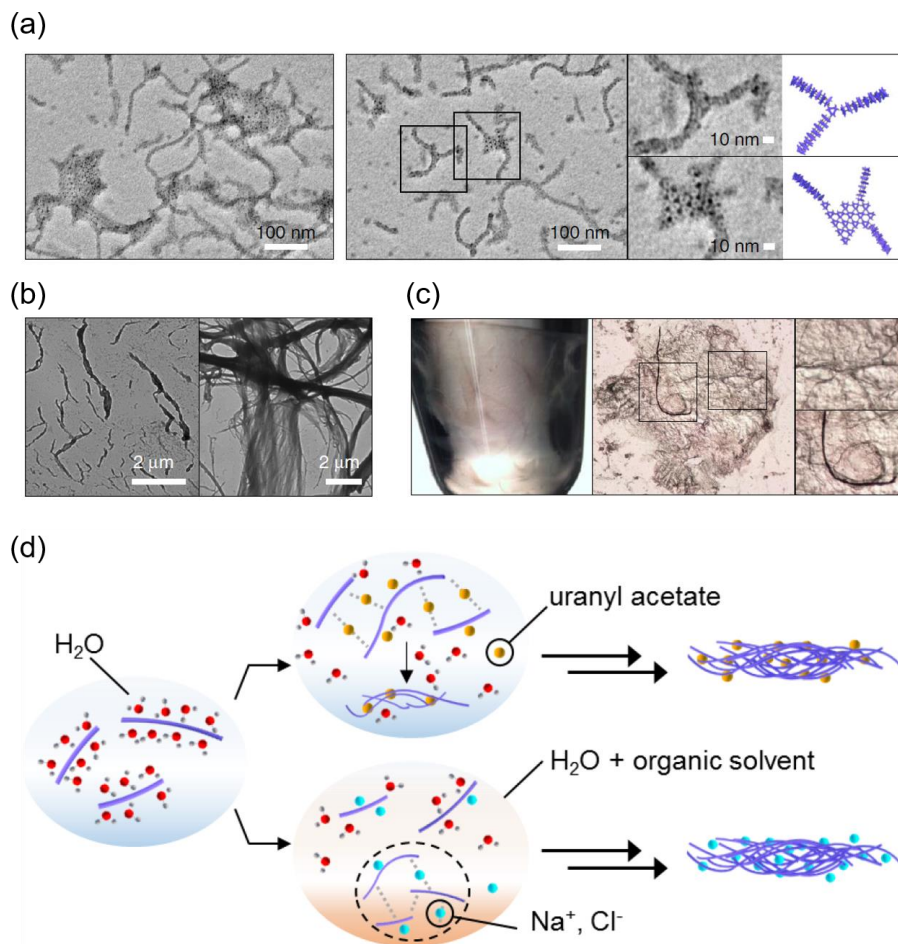


Figure 2.16. Various structures derived from 1D rods and/or 2D planes. (a) Formation of hybrid structures upon the addition of K337Z (2 μM) and 3 equiv. of Ni²⁺ to the pre-formed K44Z-derived rods (10 μM) and 3 equiv. Ni²⁺ at 22 °C for 4 h. TEM images were obtained after 20 h incubation at 22 °C. (b) Addition of uranyl acetate (0.2 wt%) to the K44Z-derived rods. (c) Addition of polar organic solvents such as methanol and acetone to the optimized E13Z/K44E derived rods (fourfold v/v). (d) A scheme for fibril formation with 1D-assembled products.

Directions and degrees of polymerization were dictated by the [Ni(Bpy)₂] formation solely. Therefore, we envisioned that hybrid structures composed of 1D, and 2D assembled species can be generated by mixing 1D and 2D growing

building blocks. 2D structures were pre-formed with K337Z variant and Ni²⁺ followed by the addition of K44Z variant. TEM images represented that triangular p312 planes cross-linked with the nanorods, or multiple rods stretched over a triangular plane were formed, indicating protein assembly originated from the [Ni(Bpy)₂] formation is effectively operative even when two variants with different directionalities were used (Figure 2.16a, Appendix 2.15). Hierarchical fibril structures were also synthesized from the 1D assembled linear products. Addition of excess uranyl acetates induced strong electrostatic interactions between 1D assembled nanorods, generating fibrous structures (Figure 2.16b). When organic solvents such as methanol and acetone were added to the solution containing nanorods derived from E13Z/K44E, analogous changes were also induced, possibly due to increased electrostatic interactions between NaCl salt and nanorods (Figure 2.16c and 2.16d).

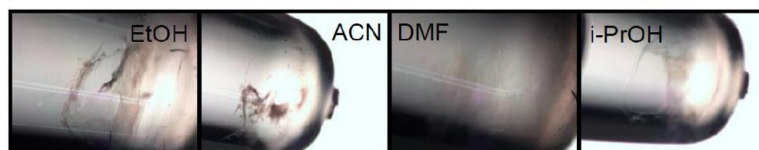
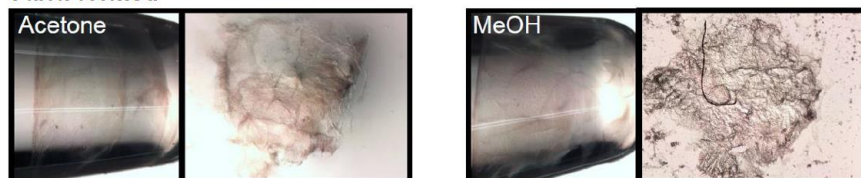
Especially, solvent triggered transformation only occurred when E13Z/K44E variant was used, not K44Z (Figure 2.17). The addition of polar solvent into assembled structures from K44Z yielded aggregated structures, indicating that higher stability of the metal complex caused by coordination environment change played important role in maintaining [Ni(Bpy)₂] complexes and consequent assembly structures. From these experiments, we demonstrate that strong interactions between protein-protein interface could stabilize overall structures and building units even after the introduction of external chemical reagents.

(a) K44Z



(b) E13Z/K44E

Fibril formed



No change



Precipitants

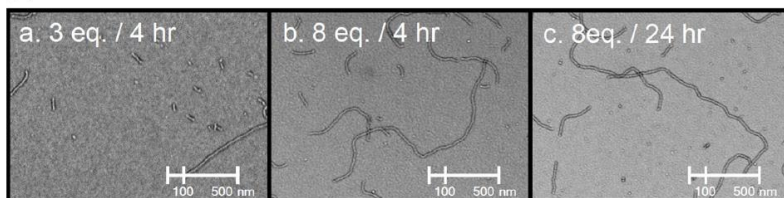


Figure 2.17. Fibril formation with 1D-rods upon solvent addition. Addition of organic solvents (4-fold volume to the buffer) to the pre-formed nanorods with (a) K44Z and (b) E13Z/K44E. K44Z-derived rods were aggregated upon the addition of acetone or methanol. E13Z/K44E-derived rods altered the overall structures depending on the applied solvents.

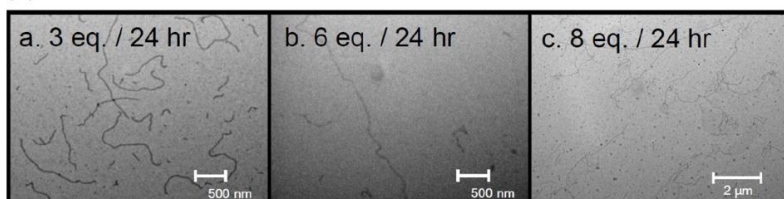
2.6. Stability test of assembled structures

We proposed that stability upon not only chemical, but thermal environment change could be enhanced via assembly, proving protein assembly as a strategy to convert enzymes to more versatile and durable biocatalysts.

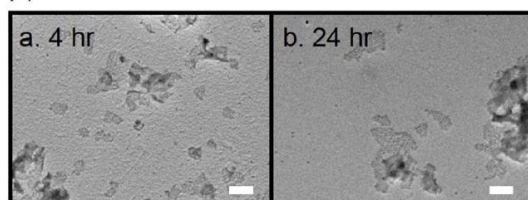
(a) K44Z



(b) E13Z/K44E



(c) K337Z



(d)

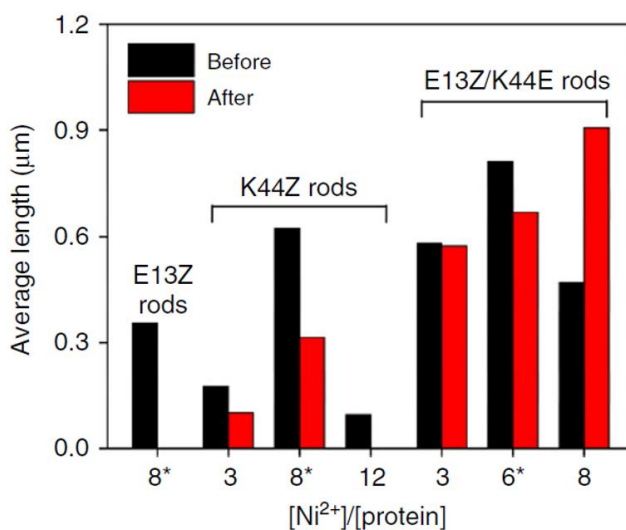


Figure 2.18. TEM images of the 1D and 2D-assembled structures after heating at 55 °C. (a) K44Z (10 μM) rods were assembled with 3 or 8 equiv Ni²⁺ at 37 °C for 24 h and were incubated at 55 °C for 4–24 h. E13Z-derived rods were aggregated (not shown) whereas K44Z-derived rods became considerably shorter. (b) Pre-assembled rods with E13Z/K44E (10 μM) with various Ni²⁺ ratios to protein (3–8 equiv). With 8 equiv. of Ni²⁺, the length of the rods heated at 55 °C was longer than those at 37 °C. (c) K337Z-derived 2D-planes with no considerable structural change upon heating for 4–24 h (scale bar: 100 nm) (d) Changes in the length of rods formed at 37 °C before and after heating at 55 °C. The optimal Ni²⁺ ratios for each variant are shown with asterisks.

Both 1D and 2D assembly at higher than 50°C generated less effectively polymerized structures or precipitates due to the instability of the building unit, as described above. However, once the assemblies were formed, the 1D and 2D structures were maintained even after heating for 24 h at 55 °C, indicating that the assembly process enhances the thermal stability of building units (Figure 2.18). Notably, the changes in structures of nanorods depended on the coordination environment of metal complexes. E13Z- and K44Z-derived rods aggregated or became shorter rods upon heating, respectively, however, E13Z/K44E rods exhibited no distinct changes in the average length of assembled structures (Figure 2.18a and b). Furthermore, when assembled structures from E13Z/K44E with higher than optimal amounts of Ni²⁺ (8 equiv.) were heated, the rods transformed into further extended structures (Figure 2.18d, Appendix 2.16). It is presumably due to enhanced thermal stability for assembled structures to reach the new thermodynamic equilibrium with higher temperatures and sufficient amounts of Ni²⁺. Also when the assembly was constructed via 2-dimensional pathway, discrete destruction upon heating was not observed (Figure 2.18c). No time-dependent degradation in the length of K44Z derived rods were observed, indicating that change in length is not a gradual degradation process during heating, but reach a thermodynamic stable equilibrium in changed condition.

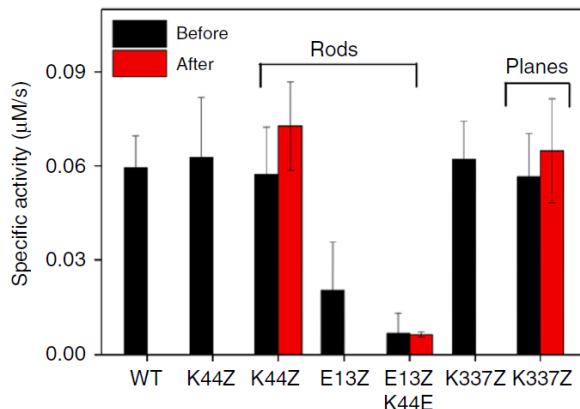
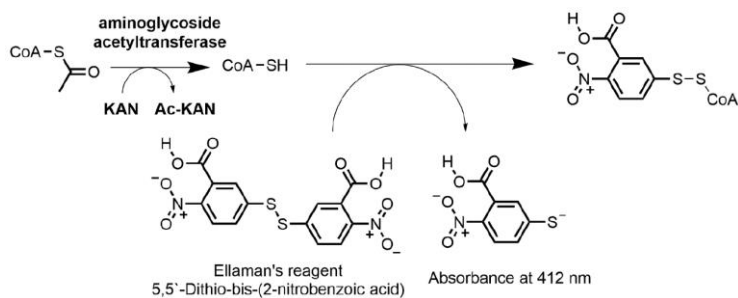


Figure 2.19. The native enzyme activities as acetyltransferases in the reactions with acetyl coenzyme A and kanamycin before and after heating at 55 °C. The error bars for the unheated samples (black columns) indicate the standard deviations of the 11, 23, 12, 5, 4, 11, and 13 runs of kinetic measurements with the wild-type, K44Z, K44Z-rods, E13Z-rods, E13Z/K44E-rods, K337Z, and K337Z-planes, respectively. The error bars for the heated samples (red columns) indicate the standard deviations of the 10, 3, and 9 runs of the experiments with K44Z-rods, E13Z/K44E-rods, and K337Z-planes, respectively.



Scheme 2.2. The colorimetric assay to measure the activity of aminoglycoside acetyl-transferase.

We measured the native enzymatic activities of 3N7Z using the assembled protein materials (Figure 2.19). The building unit selected for assembly in this study is a sort of acetyltransferase that catalyzes the transfer of an acetyl group to an amino group of various aminoglycosides (Scheme 2.2). The steady-state specific activities of the mutant variants (E13Z, E13Z/K44E, K44Z, K337Z) without Ni^{2+} at room temperature were measured, concluding the activities of K44Z and K337Z

were comparable to those of the wild-type homohexameric protein. However, E13Z and E13Z/K44E mutants showed no activities in catalytic reactions, presumably because E13Z mutation might alter the critical factors in catalytic mechanism.

Then, the catalytic activities of the K44Z and K337Z derived nanomaterials were measured at room temperature. Both materials were catalytically active, representing that the changes in overall morphology or protein-protein interfaces created by [Ni(Bpy)₂] did not exert considerable perturbation in the catalytic performance of enzymes. We also measured the catalytic activities of WT protein, variant proteins, or materials at room temperature after heating at 55 °C. WT protein and variant proteins exhibited no catalytic performance after heating, however, the assembled materials maintained their activities even after incubation at elevated temperatures for 24 h. Thus, this demonstrates that the thermally stabilized protein-assembled materials can preserve their native catalytic activities, implying that more natural enzymes can be designed into more stable and versatile biocatalysts by assembly strategy¹¹.

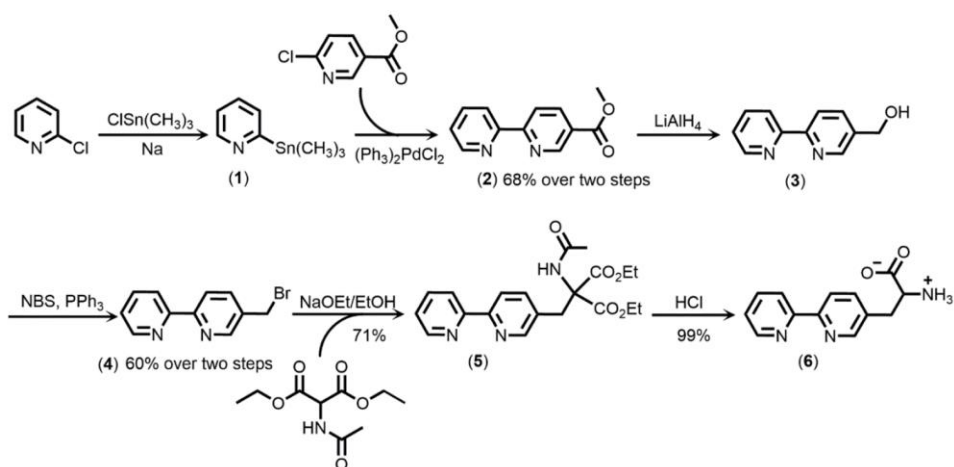
2.7. Conclusion

Genetic incorporation of unnatural chelating amino acids for site-selective metal coordination enabled dynamic and highly controllable protein self-assembly. Interestingly, the sequence of the selected protein was not optimized for self-assembly, and the protein is constituted of 2328 amino acids, including 252 glutamate, 90 aspartate, and 66 histidine residues, which can interact with metal ions and trigger the formation of undesirable products. However, diverse structures ranging from 1D, 2D, hybrid, and fibril structures could be synthesized only by mixing a single protein, ligand, and metal ion. Kinetic and thermodynamic controls of the reversible metal complex formation lead to the manufacturing of diverse architectures with tunability, in terms of shape, length, and stability while retaining native catalytic activity. Therefore, metal-dependent polymerization of protein using bipyridine groups may provide effective methods to tailor structurally and functionally versatile protein-based catalysts and materials. Because the formation of $[\text{Ni}(\text{bpy})_2]$ species is orthogonal to the introduction of other covalent or noncovalent interactions to elicit protein assemblies, we speculate that the scope of target proteins and their concurrent assembled structures can be significantly expanded. Multidimensional or multicomponent protein assemblies can be created, resulting in high levels of structural and functional complexity such as artificial cells or protein compartments for cascade reactions or dynamic motions upon altered chemical environments.

2.8. Experimental section

General procedure

Chemicals or metal salts were purchased from Sigma Aldrich, Acros organics, Alfa Aesar or LPS solution and used without further purification unless described. ^1H -NMR spectra were collected with Varian 500 MHz NMR using CDCl_3 or CD_3OD solvents. All metal salts were prepared by dissolving metal chloride (MnCl_2 , $\text{CoCl}_2 \cdot 6\text{H}_2\text{O}$, $\text{NiCl}_2 \cdot 6\text{H}_2\text{O}$, $\text{CuCl}_2 \cdot 2\text{H}_2\text{O}$, ZnCl_2 , NaCl , LiCl) in ddH_2O . All aqueous solutions were prepared with ddH_2O and filtered with $0.22 \mu\text{m}$ syringe-filters before usage.



Scheme 2.3. Synthesis of Bpy-Ala.

Synthesis of Bpy-Ala amino acids.

The chelating unnatural amino acids were prepared as described previously^{12,13}, and were briefly summarized above (Scheme 2.3).

Synthesis of 2-trimethyltin pyridine (1)

To a suspension of 2 mm metallic sodium (3.03 g) in dimethoxyethane (28 mL),

trimethyltin chloride (8.72 g) dissolved in dimethoxyethane (7 mL) was added dropwise with stirring over 15 min at 0 °C under argon stream. After stirring for 2 h at 0 °C, unreacted sodium was removed from green suspending solution. 2-chloropyridine (3.3 mL) dissolved in dimethoxyethane (21 mL) was added dropwise to green suspending solution at 0 °C under argon stream. The reaction continued for 3 h at 0 °C under argon stream. Dimethoxyethane was removed in vacuum, and the product (1) was obtained via extraction using diethyl ether. The solution (1) was used in next step without further purification.

Synthesis of methyl 2,2'-bipyridine-5-carboxylate (2)

For coupling reaction, m-xylene was purified with molecular sieve prior to distillation. A stirring solution of (1), m-xylene (100 mL), Pd(PPh₃)₂Cl₂ (1.05 g), and 6-chloromethylnicotinate (4.98 g) equipped with reflux condenser was heated to 160 °C. The reaction mixture changed to black color. After 7 h, the reaction mixture was cooled to room temperature and was stirred for 15 min with cellite. After filtration and evaporation, the reaction crude mixture was applied to silica gel flush column chromatography (eluent hexane/ethyl acetate = 3:1 with 5% of triethylamine) to yield the desired product (2) (5.2 g, 68% via two steps).

¹H-NMR (CDCl₃-d₁, 500 MHz) of (2)

(Appendix 2.17): δ 3.99 (s, 3H), 7.37 (s, 1H), 7.86 (t, J = 7.3 Hz, 1H), 8.42 (d, J = 7.9 Hz, 1H), 8.56–8.46 (m, 2H), 8.72 (s, 1H) and 9.28 (s, 1H).

Synthesis of (2,2'-bipyridin-5-yl) methanol (3)

Anhydrous tetrahydrofuran was prepared by distillation with sodium-benzophenone after dehydration with molecular sieve. LiAlH₄ (0.76 g) in THF suspension was added dropwise at -78 °C to a stirring solution of (2) (4.0 g) in 55 mL of anhydrous THF under argon stream. The resulting solution was slowly warmed to -20 °C, and stirred for 1 h. Then, 10% aqueous THF solution (50 mL)

was added very slowly at $-78\text{ }^{\circ}\text{C}$, and warmed to room temperature. Resulting orange solution was treated with celite, stirred for 15 min, and filtered. Red colored oil (3) (3.34 g) was extracted with DCM and was used without further purification.

Synthesis of 5-(bromomethyl) 2,2'-bipyridine (4)

To a stirring solution of (3) in DCM (75 mL), N-bromosuccinimide (3.66 g) and triphenylphosphine (5.18 g) were added at $0\text{ }^{\circ}\text{C}$, and resulting solution was stirred for 1 h at the same temperature. After concentrating the solution to $\sim 7\text{ mL}$, silica column chromatography was applied (eluent hexane: ether = 2:1 to 1:1) to yield white solid (4) (2.67 g, 60% in two steps).

$^1\text{H-NMR}$ ($\text{CDCl}_3\text{-d}_1$, 500 MHz) of (4)

(Appendix 2.18): δ 4.55 (s, 2H), 7.36–7.30 (m, 1H), 7.85 (m, 2H), 8.40 (s, 1H), 8.42 (s, 1H) and 8.69 (s, 2H).

Synthesis of (2,2'-bipyridin-5-yl)diethyl acetacetomalonate (5)

To a stirring solution of acetacetomalonate (3.3 g) and sodium ethanolate (1.03 g) in anhydrous EtOH (90 mL), (4) (2.5 g) was added and refluxed overnight. After evaporation, the crude reaction product was purified by silica gel flush column chromatography (eluent: hexane: EA = 2:1 to 1:1; then, DCM: MeOH = 15:1 to 10:1) to yield (5) (2.7 g, 70%).

$^1\text{H-NMR}$ ($\text{CDCl}_3\text{-d}_1$, 500 MHz) of (5)

(Appendix 2.19): δ 1.32 (dt, $J = 7.1, 4.4\text{ Hz}$, 6H), 2.09 (dd, $J = 4.6, 2.0\text{ Hz}$, 3H), 3.75 (s, 2H), 4.22–4.34 (m, 4H), 6.61 (s, 1H), 7.32 (t, 1H), 7.49 (d, $J = 7.9\text{ Hz}$, 1H), 7.82 (t, $J = 7.6\text{ Hz}$, 1H), 8.33 (dd, $J = 20.6, 7.5\text{ Hz}$, 3H) and 8.68 (s, 1H).

Synthesis of (2,2'-bipyridin-5-yl)alanine or Bpy-Ala (6)

(2,2'-bipyridin-5-yl) diethyl acetacetomalonate (5) (2.7 g) in 37% HCl (75 mL) was heated to reflux overnight. Removing of HCl lead to formation of final product, Bpy-Ala. It was used for incorporation of unnatural amino acid to the selected proteins without further purification.

¹H-NMR (MeOD-d₁, 500 MHz)

(Appendix 2.20): δ 3.49 (ddd, J = 41.0, 14.6, 6.7 Hz, 2H), 3.78 (s, 2H), 4.49 (t, J = 6.7 Hz, 1H), 8.08–8.02 (m, 1H), 8.29 (d, J = 8.2 Hz, 1H), 8.56 (d, J = 8.3 Hz, 1H), 8.64 (t, J = 7.9 Hz, 1H), 8.76 (d, J = 8.2 Hz, 1H) and 8.94–8.87 (m, 2H).

The selection of divalent metal ions for the current work

The related thermodynamic parameters of the first-row divalent transition metal ions with bipyridine ligands were included Table 2.1. We considered following metal binding equilibrium for selection of metal ions. Equilibrium constants of the Eqs. (1)–(3) in Scheme 2.1 were listed in Table 2.1.

Nucleotide sequences
<p>CATATGAGCAATGCCATGAATGTGATTCGCCTGAAAGAAGATAAAATTCGCGAA GCACTGCGTCTGAGCGAATATGCATTCAGTATAAAGTGGATGAAGATCGTCTGC AGCAGCAGATTACCAAAATGAAAGAAAGCCATGAAGTGTATGGC/CATCATGGAA GGTGA/AAATCTGGCAGCAAAACTGCATCTGATCCGTTTCATATCTACATCGGCA AAGAAAAATCAAGATGGGTGGTGTTCGCCGGTGTTCGCAACCTATCCGGAATATC GTCGTAGCGGTTATGTTAAGAAGACTGCTGCAACATAGCCTGCAGACCATGAAAA AAGATGGTTATACCGTTAGCATGCTGCATCCGTTTGCAGTTAGCTTTTATCGTAAA TATGGTTGGGAACTGTGTGCCAATCTGCTGGTTTGTACATGACCAAAAAGCGAT CTGGTTATGAAAAACAGGTTAACGGCACCGTGAAACGCTTTAACAAAGAAAG TCATCCGGAAGAGGTGGAAAACTGTATGAAACCTTTGCAGAACTGTTTAGCG GTATGCTGGTTCGTAATGAAAAATGGTGGCTGCAGGCAGTTTATGATGATCTGAC CCTGGCAATCTATTATGATGAAAATCAGACCGCAGCAGGCTACATGCTGTATAAA ATCGAGA/ACTATAAGATGACCGTGGAAGAATTTGTTCCGCTGCATAATGAAGCA CGTAATGGTCTGTGGAACTTTATTTGT/CAGCATGATAGCATGATCAAAGATCTGG AAATGACCGTGAGCGAAAAATGAACCGCTGCTGTATACCCTGCAAGAACCGCGT GTTAAAACCGAAATTAACCGTATTTTATGGGTCGCATTGTGGATGTTGAACAGT TCCTGAAACAGTATGAACTGAATTGGAATAACGTGCAGCAAGAAGTGATTCTGC ATATCACCGATAGCTTTGCACAGTGGAAATAACATTACCGTTCCGATTGGCAACCA TGAGATTACCATTATTGAAGAACCGATCGACAAAGGCATCAAAC/TGGATATTAAT GCACTGAGCACCATCCTGTTTGGTTATCGTCGTCGCTGGAACTGAATGAATAG AACTGATTAGTGGCAGCGAAGAAGAAATTCGCGCATTGAAAGCGTTGTTCCGG TTCGTAAACCGTTCATCTATGACTTTTTCTAACTCGAG</p> <p>* The cut-sites for restriction enzyme were highlighted in bold letters.</p>
Protein sequences
<p>SNAMNVIRLKEDKFREALRLSEYAFQYKVDEDR/LQQITKMKESHEVYGIMEGEN LAAKLHLIPFHIYIGKEKFKMGGVAGVATYPEYRRSGYVKELLQHS/LQTMKKDGY TVSMLHPFAVSFYRKYGWELCANLLVCHMTKSDLVMKKQVNGTVKRFNKESHPE EVEKLYETFAELFSGMLVRNEKWWLQAVYDDLTLAIYYDENQTAAGYMLYKIENY KMTVEEFVPLHNEARNGLWNFICQHDSMIKDLEMTVSENEPLLYTLQEPVKTEIK PYFMGRIVDVEQFLKQYELNWNVQQEVILHITDSFAQWNNITVRIANHEITIIIEPI DKGIKLDINALSTILFGYRRPLELNELELISGSEEEIRAFESVVPVRKPFYIDFF 388 aa (Molecular weight: 45.7 kDa)</p>

Table 2.2. Sequence of the selected protein for the current work (PDB: 3N7Z).

Mutation	primer sequences (F = Forward, R = Reverse); 5'-sequence-3'
E13Z	F: GTGATTCGCCTGAAATAGGATAAATTCGCG R: CGCGAAATTTATCCTATTTACAGGCGAATCAC
Q37Z	F: GAAGATCGTCTGTAGCAGCAGATTACC R: GGTAATCTGCTGCTACAGACGATCTTC
K44Z	F: CAGATTACCAAAAATGTAGGAAAGCCATGAAGTG R: CACTTCATGGCTTTCCTACATTTTGGTAATCTG
K44E	F: CAGATTACCAAAAATGGAGGAAAGCCATGAAGTG R: CACTTCATGGCTTTCCTCCATTTTGGTAATCTG
W298Z	F: CAGTATGAACTGAATTAGAATAACGTGCAGCAAG R: CTTGCTGCACGTTATTCTAATTCAGTTCATACTG
N299Z*	F: GTATGAACTGAATTGGTAGAACGTGCAGCAAGAAG R: CTTCTTGCTGCACGTTCTACCAATTCAGTTCATAC
N300Z*	F: GTATGAACTGAATTGGAATTAGGTGCAGCAAGAAGTG R: CACTTCTTGCTGCACCTAATTCCAATTCAGTTCATAC
V301Z*	F: CTGAATTGGAATAACTAGCAGCAAGAAGTGATTCTG R: CAGAATCACTTCTTGCTGCTAGTTATTCGAATTCAG
H326Z*	F: GTTCGTATTGCCAACTAGGAGATTACCATTATTG R: CAATAATGGTAATCTCCTAGTTGGCAATACGAAC
E332Z*	F: GAGATTACCATTATTTAGGAACCGATCGACAAAG R: CTTTGTCGATCGGTTCCATAAATAATGGTAATCTC
E333Z*	F: GATTACCATTATTGAAATAGCCGATCGACAAAG R: CTTTGTCGATCGGCTATTCATAAATAATGGTAATC
D336Z*	F: GAAGAACCGATCTAGAAAGGCATCAAACCTG R: CAGTTTGATGCCTTTCIAGATCGGTTCTTC
K337Z	F: GAAGAACCGATCGACTAGGGCATCAAACCTGG R: CCAGTTTGATGCCCTAGTCGATCGGTTCTTC

Table 2.3. Primer sequences used for site-directed mutagenesis.

Incorporation of bpy-Ala to the selected proteins

The sequence of the selected protein (PDB code 3N7Z) was obtained from RCSB website and included in Table 2.2. The gene fragment was synthesized after codon optimization for Escherichia coli heterologous expression (Gene Universal Inc.) and incorporated into pET-28(a) vector using Nde1 and Xho1 restriction cut-sites. All PCRs were conducted using KOD plus neo polymerase kit purchased from Toyobo. Amber codon was used for the incorporation of Bpy-Ala to the selected residue using the custom-designed primers (Table 2.3). The plasmid for Bpy-Ala incorporation, pEVOL, was a kind gift from prof. Hak Joong Kim at Korea University. Plasmids were extracted by using DNA purification kit (Labopass). Custom-designed primer synthesis and plasmid sequencing were carried out in Macrogen. For gene cloning and heterologous protein expression, DH5 α and BL21

(DE3) *E. coli* strains (NEB) were used, respectively. For protein expression, plasmids were transformed to BL21(DE3) *E. coli* competent cells (NEB), containing pEVOL plasmid for the incorporation of Bpy-Ala³⁵. A single colony grown in the LB/agar plate containing kanamycin/chloramphenicol were inoculated in TB culture (20 mL) containing kanamycin and chloramphenicol at 37 °C. After 9 h, the cell cultures (7.5 mL) were added to 0.75 L

TB media containing kanamycin (50 mg/mL) and chloramphenicol (35 mg/L) at 37 °C and were grown in orbital shaker, 170 rpm at 37 °C for 4 h. When OD₆₀₀ reached ~1.0–1.2, 1mM Isopropyl β-D-1-thiogalactopyranoside (IPTG), 1mM Bpy-Ala, and 0.2% arabinose were added at final concentrations at 30 °C. After 12 h, cell pellets were harvested by centrifugation at 4715×g, 4 °C and kept at –80 °C. Incorporation of the chelating amino acid and expression of full-length proteins was confirmed by sodium dodecyl sulfate-poly acrylamide gel electrophoresis (SDS-PAGE) (Figure 2.20a).

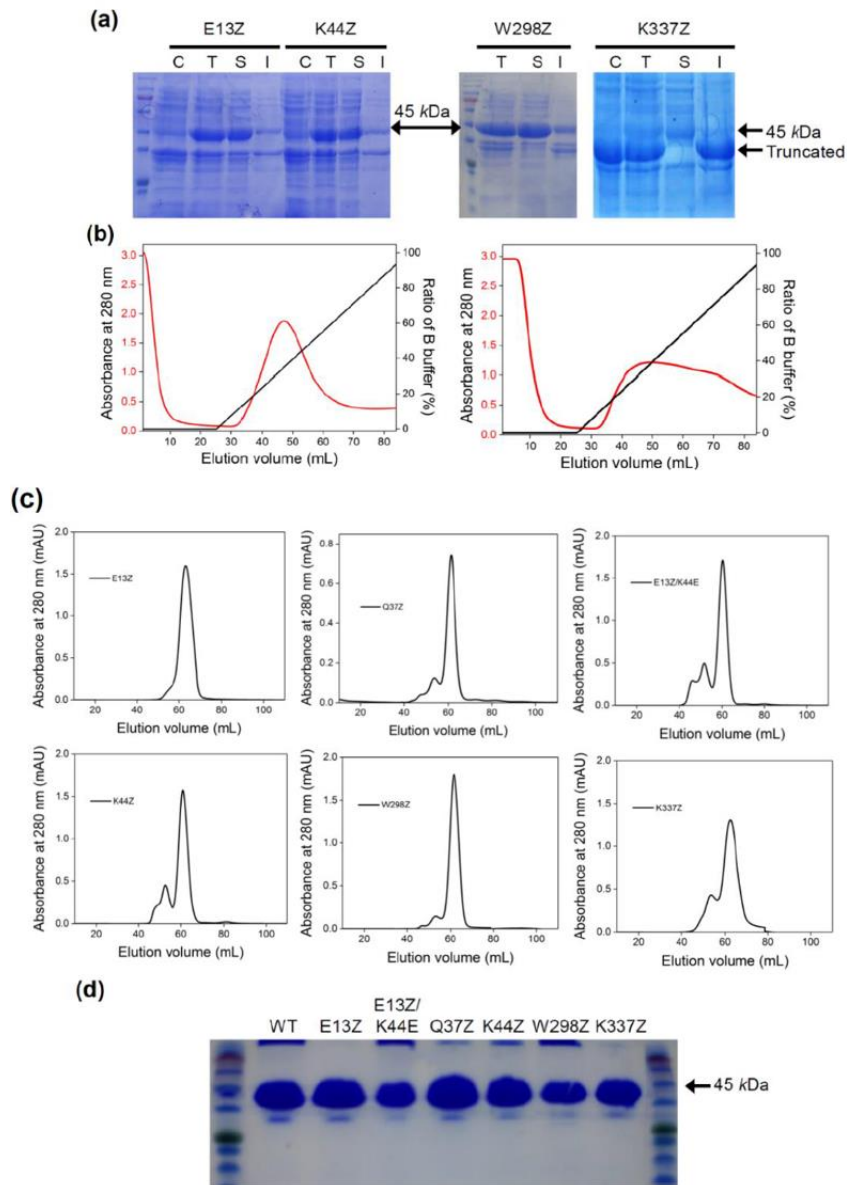


Figure 2.20. Expression and purification of bpy-Ala variants. (a) 15% SDS-PAGE analysis of protein expression. C, T, S, and I indicate whole cells, lysates, soluble fractions, and inclusion body, respectively. (b) Purification of the bpy-Ala variants with Ni-NTA column chromatography. Representative elution traces of (left) K44Z and (right) E13Z/K44E (c) Size-exclusion chromatography (S200) of the apo proteins treated with EDTA. The native hexameric protein was eluted at ~60 mL, and residual higher molecular species were observed due to the metal impurities. (d) SDS-PAGE of the purified samples.

Purification of the selected proteins

The harvested cells from 1.5 L of TB media were resuspended in lysis buffer (pH 8.0, [HEPES] = 50 mM, [NaCl] = 500 mM, [2-mercaptoethanol] = 10 mM, [Imidazole] = 5 mM, 10% w/v glycerol) at 4 °C, sonicated in iced bath (on/off = 1.0 s/1.5 s for 30 min). After centrifugation at 18,800×g at 4 °C for 35 min and syringe filtration, the soluble fraction was directly applied to 5mL His Trap-FF (GE Healthcare Life Sciences) with ÄKTA pure protein purification system at 4 °C (Figure 2.20b). Eluted samples were treated by thrombin with 20mM EDTA at 22 °C overnight to delete the His-6 tag prior to the N-terminus. The resulting samples were purified by His Trap-FF and Superdex 200 gel filtration columns (GE Healthcare Life Sciences) with the following buffer, [Tris-HCl] = 50 mM, [NaCl] = 150 mM, pH 8.0, at 4 °C (Figure 2.20c). Then, the samples were used for the reactions with metal ions after buffer exchange with salt-free buffer. All purified proteins were characterized by SDS-PAGE (Figure 2.20d). Protein concentration was determined by measuring the absorbance at 280 nm (UV-vis spectrophotometer, Agilent Technologies Cary 8454 UV-vis) by using the epsilon values of protein and bipyridine at 280 nm⁷.

Sample preparations

Reactions of the bpy-variants with Ni²⁺ were carried out with 50mM Tris, 150mM NaCl, pH 7.1 buffer at 37 °C for 24 h. It is noteworthy that depending on the temperature, the pH value of the Tris buffer changes as 8.0, 7.5, 7.1 at 4, 22, 37 °C, respectively. To monitor pH-dependent formation of protein-assembly, 50mM MES pH 6, 50mM Tris at pH 7–8, 50mM CHES pH 9 buffers were prepared and applied at 37 °C.

Transmission electron microscopy

TEM grid and uranyl acetate were purchased from Electron Microscopy Sciences.

Carbon-coated 200-mesh copper grids (CF200-Cu) were applied to glow discharge using PELCO easy glow (Ted Pella Inc.). For nanorods, each sample was diluted with the buffer used for sample preparation to 0.05 μM at final concentration just before loaded to TEM grid. For 2D-planes, the sample was loaded without dilution. After incubation for 1 min, any remaining liquid was removed by filter paper, washed with ddH₂O, and stained with 1 wt % uranyl acetate solution. After drying, TEM was operated at HITACHI H-7600 (HITACHI-Science & technology, 120 kV), using a software AmtV542. The focal point was set in a manner that the rods were seemingly a hollow tube-like material because it enables us to distinguish singly aligned tubes from interweaved multi-stranded fibrils (Figure 2.21).

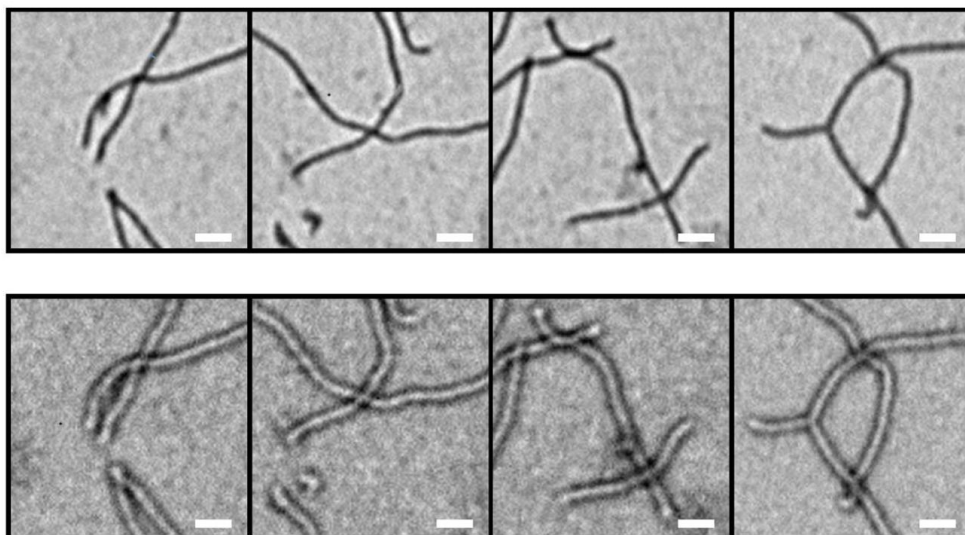


Figure 2.21. TEM images of the linear rods collected with different focal points (scale bar: 50 nm).

TEM images were analyzed using an image analysis software, Digimizer. The lengths of at least 100 protein-rods were measured to estimate the number average length (L_n), weight average length (L_w), and PDI for each condition as,

$$L_n = \frac{\sum_{i=1}^N N_i L_i}{\sum_{i=1}^N N_i},$$

$$L_w = \frac{\sum_{i=1}^N N_i L_i^2}{\sum_{i=1}^N N_i L_i},$$

$$\text{PDI} = L_w / L_n,$$

where N is the total number of rod-species examined from TEM images, L_i is the length of each rod, and N_i is the number of species of which length is L_i . To examine the effects of reactions conditions on the 1D-rod growths, we plotted the number average length (L_n) values as a function of metal to protein ratios, temperatures, and protein concentrations. To depict the length distributions of the 1D-rods, the measured length values were binned into 50 nm ranges and the frequency of each range was plotted into the bar charts.

UV–vis spectroscopy

The Ni^{2+} binding to bpy-anchored proteins were monitored by UV–vis spectrophotometer (Agilent Technologies Cary 8454 UV–VIS). To detect the time-dependent spectral changes, 6 equiv. of Ni^{2+} were add to protein (5 μM) in 50mM Tris-HCl, 150 mM NaCl, 400 μL at final volume at 25 °C.

Size exclusion chromatography

The oligomeric states of the assembled proteins were determined by size exclusion chromatography using Superdex 200 gel filtration columns (GE Life Sciences) ([Tris-HCl] = 50 mM, [NaCl] = 150 mM, pH 8.0 buffer at 4 °C) with Ä KTA pure protein purification system at 4 °C.

Cryo-TEM

Protein sample (3 μL , 5–10 μM K337Z) reacted with metal ions were loaded on glow-discharged quantifoil (R 2/2, 400 mesh holey-carbon grid, Quantifoil Micro

Tools), blotted for 2 s at 4 °C and frozen using Vitrobot (Thermo Fisher Scientific, USA) in liquid ethane. The samples were analyzed using Talos L120C TEM (Thermo Fisher Scientific, gun type: Lab6, 120 kV) at National Instrumentation Center for Environmental Management (NICEM) at Seoul National University.

Atomic force microscope (AFM)

For acquiring AFM image, total 50 µL of premade rods (10 µM) were prepared and buffer was exchanged to ddH₂O to eliminate remaining salts using centrifugal minispin-column (Merck Millipore). Diluted samples were loaded to piranha solution treated silicon wafer with SiO₂ thin layer and dried in the air. AFM images were acquired with park systems XE-70 AFM using an AFM tip non-contact cantilever (PPP-NCHR 10M, Park SYSTEMS) with tapping mode.

Catalytic activity assays

Natively, the selected protein is an aminoglycoside acetyltransferase, which acetylate amines of aminoglycosides, such as kanamycin upon the reaction with acetyl coenzyme A, acetyl-S-CoA. As a result, CoA-SH is generated as a product, of which concentrations can be quantitatively determined by the addition of Ellman's reagent with the absorption changes at 412 nm. We used 96-well plate reader (SYNERGY H1 microplate reader, BioTek) to monitor the absorption changes at 412 nm at the intervals of 15 s for 10–15 min upon the addition of acetyl CoA (0.5 mM at final concentration) to the solution ([Tris-HCl] = 50 mM, pH 8.0 buffer at 4 °C) containing proteins or protein-assembled structures (0.5 µM hexamer at final concentration), kanamycin (KAN) (0.5 mM), and Ellman's reagents (2 mM) at 25 °C.

2.9. References

1. H. S. Lee and P. G. Schultz, *J. Am. Chem. Soc.* 2008, **130**, 13194.
2. C. Kaes, A. Katz, and M. W. Hosseini, *Chem. Rev.* 2000, **100**, 3553.
3. R. M. Simth and A. E. Martell, *Critical Stability Constants*, 1974, Plenum Press.
4. K. D. Green, T. Biswas, C. Chang, R. Wu, W. Chen, B. K. Janes, D. Chalupska, P. Gornicki, P. C. Hanna, O. V. Tsodikov, A. Joachimiak, and S. G. Tsodikova, *Biochemistry* 2015, **54**, 3197.
5. R. D. Hancock and A. E. Martell, *Chem. Rev.* 1989, **89**, 1875.
6. H. G. Seisdedos, C. E. Mot, N. Elad, and E. D. Levy, *Nature* 2017, **548**, 244.
7. K. Nakamoto, *J. Phys. Chem.* 1960, **64**, 1420.
8. Z. S. Derewenda and P. G. Vekilov, *Acta Cryst.* 2006, **62**, 116.
9. A. Winter and U. S. Schubert, *Chem. Soc. Rev.* 2016, **45**, 5311.
10. N. E. Hernandez, W. A. Hansen, D. Zhu, M. E. Shea, M. Khalid, V. Manichev, M. Putnins, M. Chen, A. G. Dodge, L. Yang, I. M. Berrios, M. Banal, P. Rechani, T. Gustafsson, L. C. Feldman, S. H. Lee, L. P. Wackett, W. Dai, and S. D. Khare, *Nat. Chem.* 2019, **11**, 605.
11. J. D. Brodin, J. R. Carr, P. A. Sontz, and F. A. Tezcan, *Proc. Natl. Acad. Sci. USA.* 2014, **111**, 2897.
12. Y. Yamamoto and A. Yanagi, *Chem. Pharm. Bull.* 1982, **30**, 1731.
13. C. A. Panetta, H. J. Kumpat, N. E. Heimer, M. C. Leavy, and C. L. Hussey, *J. Org. Chem.* 1999, **64**, 1015.

Chapter 3. Application of redox-active porous organic polymers in electrochemical energy storage materials

3.1. Redox-active porous organic polymers

Porous organic polymers (POPs) are an emerging class of nanoporous materials with a fascinating array of different chemistries. POPs are normally classified into several subtypes according to the synthetic procedure; top-down and bottom-up methods. Among them, designing POPs via bottom-up approaches have several advantages over other strategies. Covalent interactions between multi-branched organic molecules can generate micro- or mesoporous materials with high stability¹⁻³. Furthermore, the chemical and structural nature of POPs can be easily tuned by judicious consideration of building blocks. Modified with diverse functional groups, the POPs are extensively applied in various fields such as gas separation⁴, sensing⁵, catalysis⁶, proton/electron conduction^{7,8}, molecular separation^{9,10}, drug delivery¹¹, and release¹².

The diversity of organic synthesis enabled the enormous possible design strategies for POPs. Especially, diverse redox-active backbones, such as carbonyl compounds (e.g. quinone, anhydride, imide), nitrogen-containing compounds (e.g. amine, pyridine), sulfur-containing heterocycles, and radical compounds have been utilized in synthesizing redox-active POPs. Building blocks with electron-donating or withdrawing groups generate electron-rich or deficient polymers, respectively¹³. The modified highest occupied molecular orbital (HOMO) levels or lowest unoccupied molecular orbital (LUMO) levels of polymers can facilitate surface redox reactions and control the redox potential of the reactions. Taking the advantage of redox-active characteristics and highly porous structures, redox-active POPs are extensively used as electrode materials, facilitating redox-active catalytic reactions such as hydrogen evolutions^{14,15} or water oxidations^{16,17}, and serving as efficient energy storage¹⁸ and converting¹⁹ devices.

3.2. Redox-active POPs for high energy/power density energy storage materials

Resource depletion and environmental pollution issues urged the development of alternative and sustainable energy production systems such as wind, solar, geothermal, bio, and hydraulic energy systems²⁰⁻²². Accordingly, many efforts have been made to develop efficient energy storage and conversion systems. Electrochemical energy storage systems (EESSs) can effectively convert, store, and supply energy produced, making them the major part of portable electronic devices.

The characteristic features of EESSs differ depending on the constituting electrode materials involving metal/metal oxide^{23,24}, polymers^{25,26}, and small organic molecules^{27,28}. The structural and chemical properties of electrode materials determine the charge storage mechanism (faradaic, non-faradaic), and mass transfer kinetics²⁹. Based on this classical point, the EESSs can be classified into battery-type electrodes, which store the charge through redox-active reactions with slow mass transfer, and electric double-layer capacitors (EDLCs)-type systems where the charge storage occurs solely by the accumulation of electrolytes with fast mass transfer. Thus, battery-type electrode materials can store higher charges compared to the EDLC, while the electrode with capacitive behavior can facilitate fast charge storage²⁹.

With the development of nanostructured materials, however, the behavior of classical mechanisms became indistinguishable. Nanostructured redox-active materials enable redox-active reactions and facilitate fast ion transfer on the electrode surface^{30,31}. These ‘in-between’ type materials, called pseudocapacitors, can potentially become promising electrode materials that can exhibit high energy and power density at the same time.

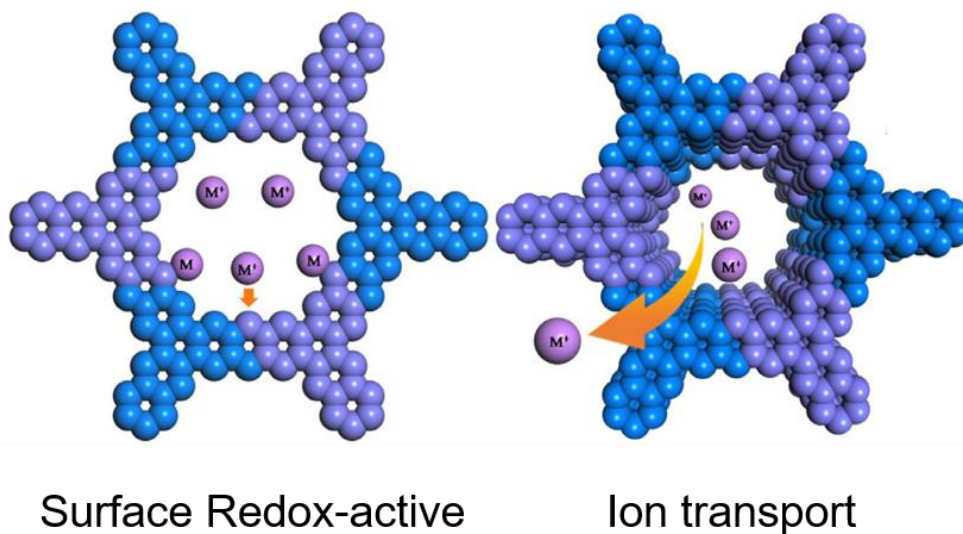


Figure 3.1. Characteristics of redox-active POPs. Copyright © 2021 WILEY-VCH Verlag GmbH & Co. KGaA, Weinheim.

With an increasing demand for environmental-friendly, metal-free, flexible, high-specific energy and power density materials, redox-active POPs are gaining enormous attention from material and energy scientists. Facile functionalization of building blocks makes POPs have a broad range of redox potential, enabling them to be utilized in both positive and negative electrode materials³². Furthermore, POPs from highly redox-active molecules can store high charge capacity comparable to classical metal or metal oxide-based materials³³. From the point of mass transfer, POPs have intrinsic porosity which can facilitate fast ion transport at the electrode surface. Strategies for nanostructuring POPs such as exfoliations and fragmentations are also extensively applied to enhance ion mobility^{34,35}. Thus, numerous POPs have been utilized for supercapacitors that show pseudocapacitive behavior in energy-converting devices, which combine the optimal properties of batteries and electric double-layer capacitors, resulting in high specific energy and power density³⁶.

3.3. Configurations for organic electrode materials in EESSs

The utilization of organic molecules or organic polymers in EESSs starts in the 1960s when the molecules with carbonyl moiety were used as a cathode for Li-ion batteries³⁷. Subsequently, organic molecules with diverse functional groups involving nitrile, sulfur, radicals, imine, and azo compounds were used as organic electrode materials for batteries. Polymeric networks of these units were also enormously investigated for electrode applications since the polymerized building units have superior stability to monomeric ones and low solubility toward electrolytes³⁸.

Organic moiety for electrode materials can be largely classified into three types, involving n-type, p-type, and bipolar-type, according to redox-active functional groups. p-Type organic materials are often functionalized with electron-donating groups, endowing them with high HOMO levels. Thus, p-type organic electrode materials normally first undergo oxidation with anion binding. Electron-rich compounds such as organosulfur heterocycles or tertiary amine-functionalized N-heterocycles are normally used as cathodes for batteries. Conversely, for n-type organic electrode materials, the reduction reaction first occurs with the binding of metal cations in electrolytes. Organic molecules functionalized with electron-withdrawing groups have low LUMO levels and operate in this behavior. Diverse molecules involving carbonyl, imine, nitrile, and azo groups are used as both cathodes and anodes for batteries and pseudocapacitors. Bipolar-type organic electrode materials can undergo both oxidation and reduction reactions first, indicating that bipolar-type materials have properties of p-type and n-type materials, simultaneously.

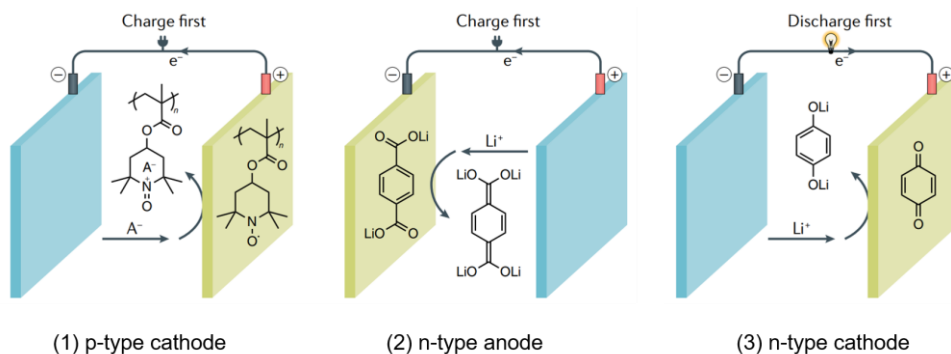


Figure 3.2. Configurations for organic electrode materials in Li batteries. Copyright © 2020, Nature Publishing Group.

The organic electrode materials have been mostly applied in Li-ion batteries among diverse EESSs. There are three possible application scenarios in Li-battery configurations for organic electrode materials. As mentioned above, p-type organic materials are normally utilized as cathodes in battery systems. The electron-rich organic molecules are first charged by oxidation and anion binding. n-Type materials can be used as both cathode and anode due to their broad range of redox potentials. Compounds with low redox potential or that can undergo overlithiation are useful candidates for anode materials of Li-ion batteries. The anode of this configuration should be charged first, during which organic compounds such as carboxyl or azo compounds accept electrons with cations. There is another configuration for n-type organic electrode materials, in which the organic electrodes are utilized as cathodes. The organic electrodes containing carbonyl or imine groups are first discharged by accepting electrons.

The application of n-type organic materials in cathodes of Li-batteries is mostly investigated among other configurations. Many reported organic electrodes from highly redox-active carbonyl and imine-based organic compounds exhibit high energy density values closed to those of commercial inorganic materials³³. Organic molecules with highly redox-active properties and low-lying LUMO levels are enormously investigated for applications in EESSs with high charge capacity and cell voltage, respectively. However, supercapacitors assembled from solely

organic materials have underperformed compared to their inorganic counterparts^{39,40}. Especially, the utilization of electron-accepting materials in organic supercapacitors still has plenty of room for development.

3.4. Demands for organic materials with highly permeable structures

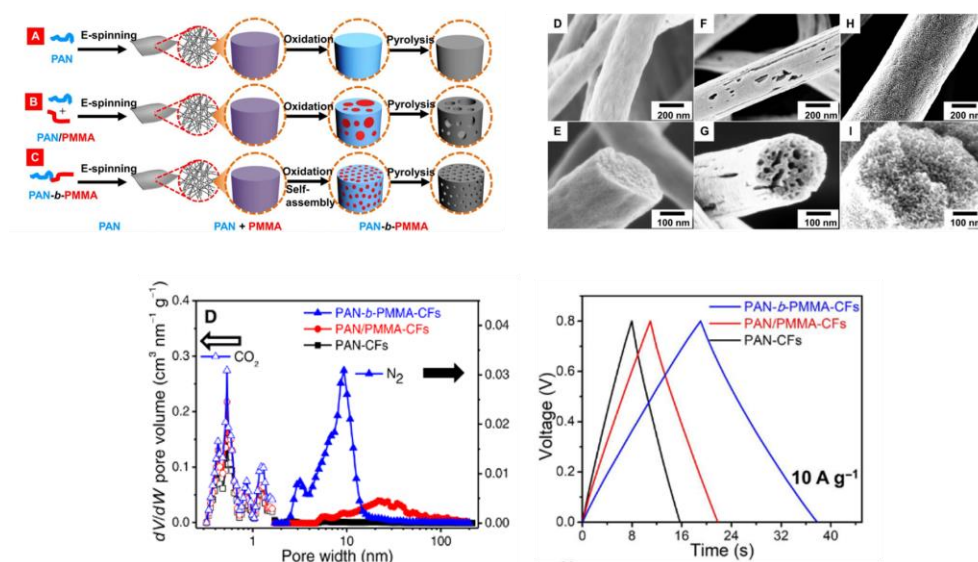


Figure 3.3. Effect of Hierarchical structures on ion permeability and power density of supercapacitors. Copyright © 2020, The American Association for the Advancement of Science.

The requirements for fast charge storage devices have urged the manufacturing of materials with diverse structures. One of the primary strategies for developing novel POPs involves redesigning the composite monomers, subsequently altering their morphologies and porosity. Alternatively, the formation of hierarchical architectures by the rearrangement of their spatial locations may yield POPs suitable for electrochemical devices⁴¹. preparing hierarchical pores ensuring interconnectivity between micropores is necessary for high flux and rapid mass transport because mesopores act as ion transport pathways and reservoirs, reducing the ion diffusion distances from the bulk electrolyte to micropores^{42,43}.

Numerous organic polymers exhibiting hierarchical porous structure with enhanced rate capability were reported; among these, porous organic nanofibers are envisioned as promising electrode materials due to their lightweight, superior flexibility, and feasibility⁴⁴⁻⁴⁶. Most porous polymer nanofibers were fabricated mainly by electrospinning of polymers, followed by post-synthetic modifications such as chemical activations or chemical exfoliations⁴⁷. With the development of synthetic methods, fiber electrode materials with superior capacitance have been reported^{48,49}; however, mostly reported as porous carbon fibers with limited functional groups and require multiple steps for preparing. Even though quite a few kinds of research about the direct generation of fibers with diverse functional groups and pores have been published, more applications taking advantage of porous and fibrous structures are still demanding.

3.5. References

1. S. Das, P. Heasman, T. Ben, and S. Qiu, *Chem. Rev.* 2017, **117**, 1515.
2. Y. Li, W. Chen, G. Xing, D. Jiang, and L. Chen, *Chem. Soc. Rev.* 2020, **49**, 2852.
3. S. Y. Ding and W. Wang, *Chem. Soc. Rev.* 2013, **42**, 548.
4. Y. Zhao, K. X. Yao, B. Teng, T. Zhang, and Y. Han, *Energy Environ. Sci.* 2013, **6**, 3684.
5. C. Pei, T. Ben, S. Xu, and S. Qiu, *J. Mater. Chem. A* 2014, **2**, 7179.
6. M. Liras, M. Iglesias, and F. Sánchez, *Macromolecules* 2016, **49**, 1666.
7. H. Xu, S. Tao, and D. Jiang, *Nat. Mater.* 2016, **15**, 722.
8. Z. Meng, R. M. Stolz, and K. A. Mirica, *J. Am. Chem. Soc.* 2019, **141**, 11929.
9. J. H. Zhang, S. M. Xie, L. Chen, B. J. Wang, P. G. He, and L. M. Yuan, *Anal. Chem.* 2015, **87**, 7817.
10. Sm. M. Xie, J. H. Zhang, N. Fu, B. J. Wang, L. Chen, and L. M. Yuan, *Anal. Chim. Acta* 2016, **903**, 156.
11. Q. Fang, J. Wang, S. Gu, R. B. Kaspar, Z. Zhuang, J. Zheng, H. Guo, S. Qiu, and Y. Yan, *J. Am. Chem. Soc.* 2015, **137**, 8352.
12. N. Singh, S. Son, J. An, I. Kim, M. Choi, N. Kong, W. Tao, and J. S. Kim, *Chem. Soc. Rev.* 2021, **50**, 12883.
13. D. D. Medina, T. Sick, and T. Bein, *Adv. Energy. Mater.* 2017, **7**, 1700387.
14. R. S. Sprick, J. X. Jiang, B. Bonillo, S. Ren, T. Ratvijitvech, P. Guiglion, M. A. Zwijnenburg, D. J. Adams, A. I. Cooper, *J. Am. Chem. Soc.* 2015, **137**, 3265.
15. V. S. Yas, F. Haase, L. Stegbauer, G. Savasci, F. Podjaski, C. Ochsenfeld, and B. V. Lotsch, *Nat. Commun.* 2015, **6**, 8508.
16. S. A. Bhat, C. Das, and T. K. Maji, *J. Mater. Chem. A* 2018, **6**, 19834.
17. C. Xu, W. Zhang, J. Tang, C. Pan, and G. Yu, *Front. Chem.* 2018, **6**, 592.
18. S. Kandambeth, V. S. Kale, O. Shekhah, H. N. Alshareef, and M. Eddaoudi, *Adv. Energy Mater.* 2021, 2100177.
19. L. Ma, S. Wang, X. Feng, and B. Wang, *Chin. Chem. Lett.* 2016, **27**, 1383.
20. M. Armand, J.M. Tarascon, *Nature* 2008, **451**, 652.

21. S. Chu and A. Majumdar, *Nature* 2012, **488**, 294.
22. Z. Yang, J. Zhang, M. C. W. Kintner-Meyer, X. Lu, D. Choi, J. P. Lemmon, and J. Liu, *Chem. Rev.* 2011, **111**, 3577.
23. O. M. Magunussen, *Chem. Rev.* 2002, **3**, 679.
24. P. Albertus, S. Babinec, S. Litzelman, and A. Newman, *Nat. Energy*, 2018, **3**, 16.
25. W. Du, X. Du, M. Ma, S. Huang, X. Sun, and L. Xiong, *Adv. Funct. Mater.* 2022, **32**, 2110871.
26. Q. Meng, K. Cai, Y. Chen, and L. Chen, *Nano Energy* 2017, **36**, 268.
27. J. J. Shea and C. Luo, *ACS Appl. Mater. Interfaces*, 2020, **5**, 5361.
28. Y. Lu, Q. Zhang, L. Li, Z. Niu, and J. Chen, *Chem* 2018, **4**, 2786.
29. T. S. Mathis, N. Kurra, X. Wang, D. Pinto, P. Simon, and Y. Gogotsi, *Adv. Energy Mater.* 2019, 9, 1902007.
30. Y. Jiang and J. Liu, *Energy Environ. Mater.* 2019, 2, 30.
31. C. Choi, D. S. Ashby, D. M. Butts, R. H. DeBlock, Q. Wei, J. Lau, and B. Dunn, *Nat. Rev. Mater.* 2020, 5, 5.
32. X. Li, H. Wang, Z. Chen, H. Xu, W. Yu, C. Liu, X. Wang, K. Zhang, K. Xie, and K. P. Loh, *Adv. Mater.* 2019, **31**, 1905879.
33. C. Peng, G. H. Ning, J. Su, G. Zhong, W. Tang, B. Tian, C. Su, D. Yu, L. Zu, J. Yang, M. F. Ng, Y. S. Hu, Y. Yang, M. Armand, and K. P. Loh, *Nat. Energy* 2017, **2**, 17074.
34. S. Wang, Q. Wang, P. Shao, Y. Han, X. Gao, L. Ma, S. Yuan, X. Ma, J. Zhou, X. Feng and B. Wang, *J. Am. Chem. Soc.* 2017, **139**, 4258.
35. Y. Yusran, H. Li, X. Guan, D. Li, L. Tang, M. Xue, Z. Zhuang, Y. Yan, V. Valtchev, S. Qiu and Q. Fang, *Adv. Mater.* 2020, **32**, e1907289.
36. M. Li, J. Liu, T. Zhang, X. Song, W. Chen, and L. Chen, *Small* 2021, **17**, 2005073
37. D. I. Williams, J. J. Byrne, and J. S. Driscoll, *J. Electrochem. Soc.* 1969, **116**, 2.
38. H. Shirakawa, E. J. Louis, A. G. MacDiarmid, C. K. Chiang, A. J. Heeger, *J. Chem. Soc. Chem. Commun.* 1977, **16**, 578.

39. M. Boota and Y. Gogotsi, *Adv. Energy Mater.* 2019, **9**, 1802917.
40. A. M. Bryan, L. M. Santino, Y. Lu, S. Acharya, and J. M. D'Arcy, *Chem. Mater.* 2016, **28**, 5989.
41. T. Liu, G. Liu, *Nat. Commun.* 2020, **11**, 4984.
42. G. Wang, H. Wang, X. Lu, Y. Ling, M. Yu, T. Zhai, Y. Tong, and Y. Li, *Adv. Mater.* 2014, **26**, 2676.
43. W. Li, J. Liu, and D. Zhao, *Nat. Rev. Mater.* 2016, **1**, 16023.
44. X. Li, X. Chen, Z. Jin, P. Li and D. Xiao, *Mater. Chem. Front.* 2021, **5**, 1140.
45. S. T. Senthilkumar, Y. Wang and H. Huang, *J. Mater. Chem. A* 2015, **3**, 20863.
46. L. Chen, X. Zhu, Y. Zhang, G. Gao, W. Xue, S. Zhang, X. Wang, Q. Zhang and X. He, *J. Mater. Chem. A* 2021, **9**, 18506.
47. Z. Zhou, T. Liu, A. U. Khan, and G. Liu, *Sci. Adv.* 2019, **5**, eaau6852
48. M. M. Abolhasani, M. Naebe, M. Hassanpour Amiri, K. Shirvanimoghaddam, S. Anwar, J. J. Michels and K. Asadi, *Adv. Sci.* 2020, **7**, 2000517.
49. T. Liu, Z. Zhou, Y. Guo, D. Guo, and G. Liu, *Nat. Commun.* 2019, **10**, 675.

Chapter 4. One-pot two-step synthesis of micro- and mesoporous organic fibrils for efficient pseudocapacitors

*The part of this chapter is accepted in the Journal of Material Chemistry A, as
M.W. Yang, W. J. Song, J. Mater. Chem. A (Accepted)

4.1. Design strategy

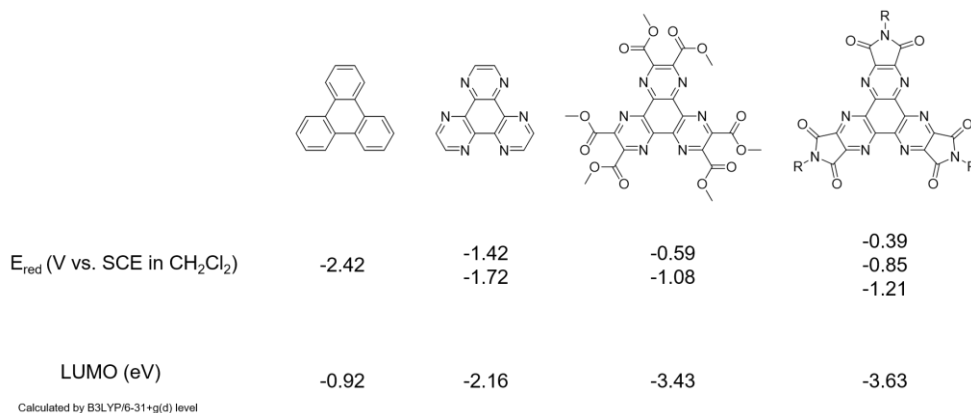


Figure 4.1. Reported reduction potentials and LUMO levels of triphenylene and hexaazatriphenylene derivatives

Polycyclic aromatic hydrocarbons (PAHs) with heteroatom-rich fused rings are utilized as versatile building blocks in POPs because of their redox activity, structural rigidity, and tendency to form π - π stacking interactions. Hexaazatriphenylene is a PAH moiety that has been extensively used in semiconducting energy-storage materials^{1,2}. However, a polyimide-containing hexaazatriphenylene triimide has not yet been reported despite the potential for an imide group to enhance redox activity. Hexaazatriphenylene triimide group can be a good candidate for electron-accepting electrode due to its highly redox-active property with low lying LUMO levels. (Figure 4.1).

Recently, increased reports about organic materials with contorted structures were published. Arrangement of intrinsically distorted building blocks constructed apertures between molecules, resulting in mesoporous channels inside materials³⁻⁵. As described in previous research, these characteristics enabled high-performance energy storage⁶ or molecular separator systems⁷ with an enhanced flux of ions or gas molecules. Herein, we synthesized porous polyimides using hexaazatriphenylene carboxylic acid (HATCO₂H) and melamine, generating inherently distorted pores inside materials due to repulsion between carbonyl

groups (Figure 4.2).

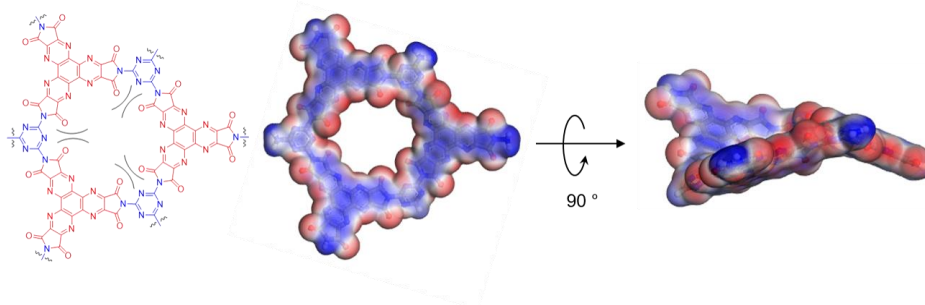
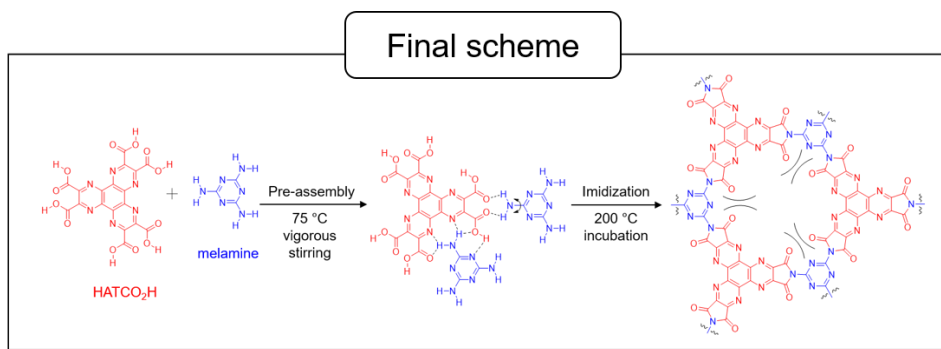


Figure 4.2. Illustration and DFT-calculated structural model of the building unit of desired structures (grey: carbon, blue: nitrogen, and red: oxygen).

Polyimides are generally formed by the condensation of anhydrides and amines⁸. However, such a combination may not be feasible for the generation of fully imidized polymers comprising contorted macrocycles; the instant and irreversible reaction between these functional groups in multi-branched building blocks may yield heterogeneous polymers. We surmised that the substantially lower and slower reactivity of carboxylic acids than anhydride could be beneficial for selective imidization with amines. Thereafter, the pair of these monomers may form pre-assembled hydrogen bonds rather than covalent amic acid bonds under mild conditions. The step preceding imidization would facilitate homogeneous polymerization (Scheme 4.1).



Scheme 4.1. Schematic illustration of porous polyimide generation.

4.2. Synthesis and morphological studies of PI-Fiber

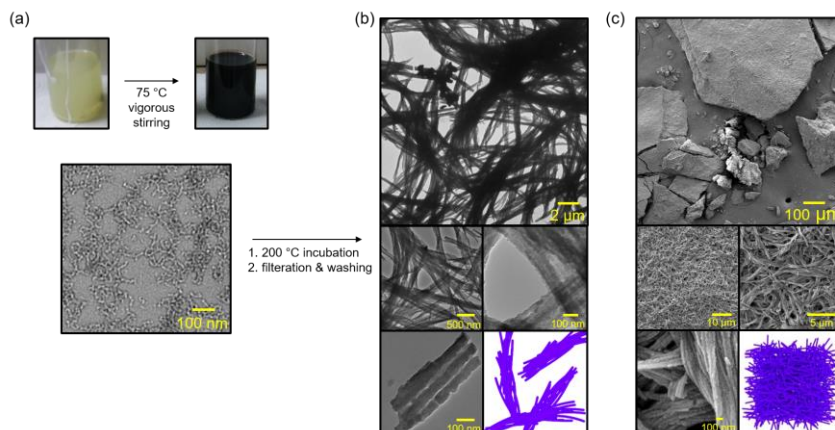


Figure 4.3. Structures of pre-organized and reacted species of PI-Fiber. (a) Dissolution of HATCO₂H and melamine salt via vigorous stirring and heating, and transmission electron microscopy (TEM) image of self-assembled building blocks dissolved in NMP. (b) TEM images and a schematic illustration of the fibrous structures. (c) Scanning electron microscopy (SEM) image and a schematic illustration of PI-Fiber.

The mixture of HATCO₂H and melamine in N-methyl pyrrolidone (NMP) was stirred at 75 °C for 24 h to drive self-assembly. Light yellow colored precipitant, salt adduct between two building blocks, first formed and gradually solubilized to form darkened solution (Figure 4.3a). With the addition of isoquinoline and mesitylene⁹, further 2–3 d incubation of the solution at 200 °C induced precipitation of dark-colored powders, which were then filtered, washed, and dried to yield **PI-Fiber**. These powders were insoluble in any of the solvents (NMP, EtOH, DCM, Acetone, EA, Hexane, MeOH), indicating the formation of large molecular weight polymers. The formation process was characterized by observing transmission electron microscope (TEM) images of self-assembled solution and time-dependent TEM images of incubated samples, demonstrating that linearly self-assembled species with 4–5 nm of width transformed into micrometer-long nanorods with a uniform width of 40–50 nm (Figure 4.3b, Appendix 4.1). The precipitated solid formed via congregation of these nanorods without thickening the width, as also can be observed in scanning electron microscope (SEM) images

of precipitated powders (Figure 4.3c, Appendix 4.2).

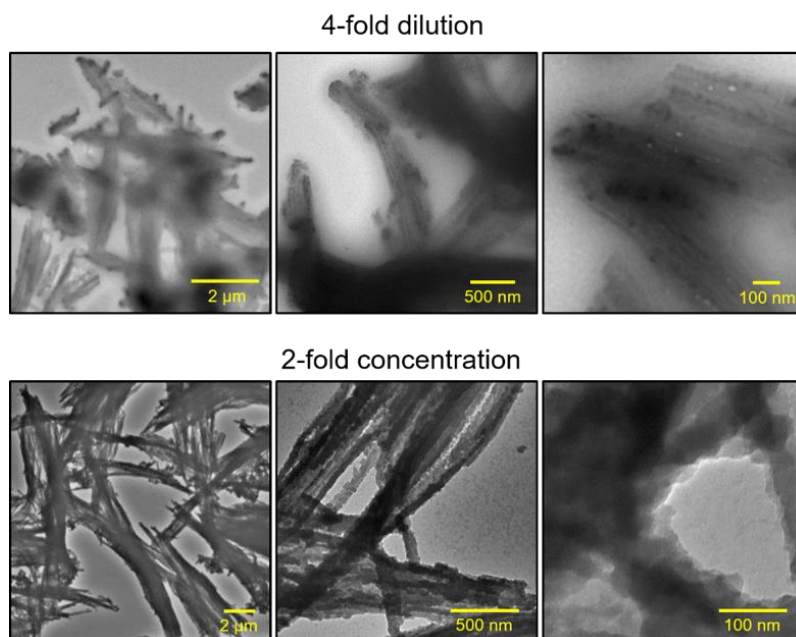
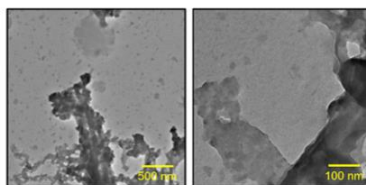
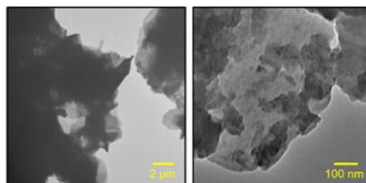
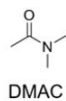
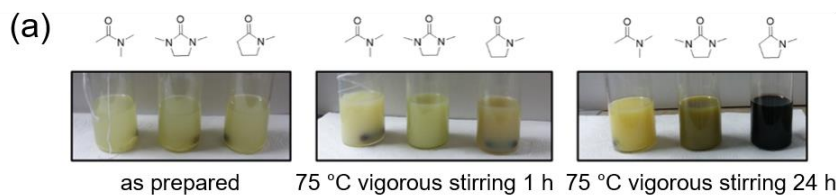
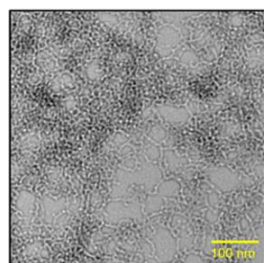


Figure 4.4. TEM images of fibrils synthesized with various concentrations of monomers. Either 4-fold diluted (25 mg of HATCO₂H and 6.3 mg of melamine) or 2-fold concentrated (200 mg of HATCO₂H and 50.4 mg of melamine) monomers were reacted in 16 ml NMP.

Some variations such as concentration, solvent, and temperatures were also tested. The concentrations of HATCO₂H and melamine altered the width of the coalesced fibrils to some extent; the 4-fold dilution of monomers yielded thinner fibrils, and no further thickening was observed when the concentrations of the two monomers were increased by 2-fold (Figure 4.4). Analogous solvents such as dimethylacetamide and dimethyl imidazolidinone were also tried to elucidate the role of solvent (Figure 4.5a). However, these solvents could not solubilize salt adduct, which yielded heterogeneous structures when heated. DMSO with small amounts of ddH₂O yielded similar fibrous structures; nonetheless, these fibers easily solubilized any solvents due to thin diameters and reduced cohesiveness (Figure 4.5b).



(b)



DMSO + ddH₂O
40 °C vigorous stirring

200 °C
incubation

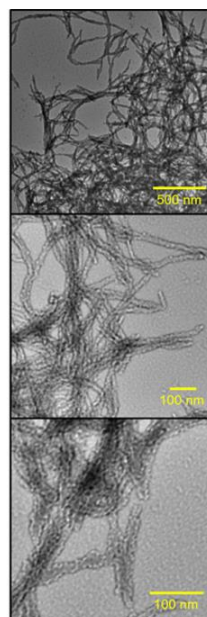


Figure 4.5. Effects of solvent on polymer synthesis. (a) TEM images of samples synthesized in solvents other than NMP. HATCO₂H (100 mg) and melamine (25.2 mg) in 16 ml of each solvent (DMAC or DMI) were mixed. They failed to solubilize pre-assembled monomers, resulting in the formation of heterogeneous precipitants after imidization. (b) TEM images of pre-assembled and imidized samples in DMSO solvent. HATCO₂H (100 mg) and melamine (25.2 mg) were dissolved in 16 ml of DMSO with 40 μ L of ddH₂O for the subsequent reactions.

Heated samples of non-stirred monomers, salt adducts, and mixtures with different ratios or samples heated at less elevated temperatures yielded complete amorphous or partial fibril structures, indicating that self-assembly, accurate ratio, and high temperature for imidization are necessary for yielding uniform fibril structures (Figure 4.6).

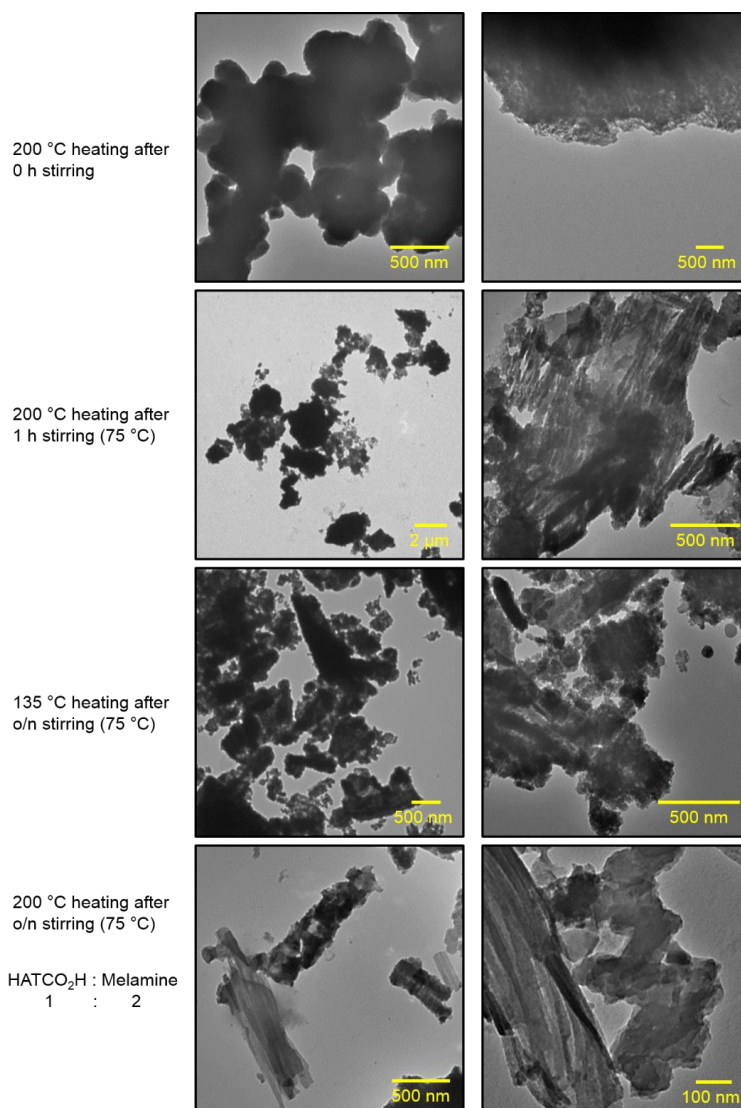


Figure 4.6. TEM images of samples prepared under unoptimized conditions. The modification of temperature for imidization, incubation time for pre-assembly, or the ratio of two monomers, as described on the left, led to heterogeneous or partially fibril structures.

4.3. Characterization of imide bond formation in PI-Fiber

Fourier Transform Infrared Spectrum (FTIR) of PI-Fiber showed the appearance of the peaks at 1680 cm^{-1} , 1380 cm^{-1} , corresponding to amide carbonyl stretching, and C–N–C stretching respectively, and decreased broad bands of –NH_2 (around 3200 cm^{-1}) and $\text{–CO}_2\text{H}$ (around 3200 cm^{-1}), indicating that formation of five-membered imide ring¹⁰ (Figure 4.7a).

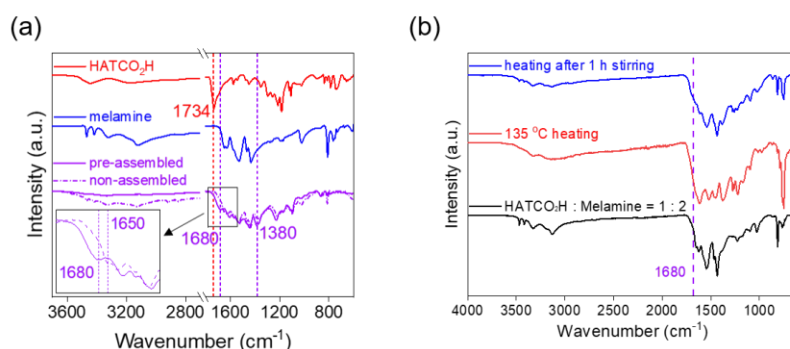


Figure 4.7. Fourier transform infrared spectroscopy (FTIR) spectra of building units and samples synthesized via above conditions. (a) Fourier transform infrared spectroscopy (FTIR) spectra of HATCO₂H, melamine, and samples synthesized from pre-assembled (PI-Fiber) and non-assembled species. (b) FT-IR spectrum of samples generated from the conditions in figure 4.6. Broad peaks around $3000\text{--}3500\text{ cm}^{-1}$, negatively-shifted carbonyl peaks at 1650 cm^{-1} , and absence at 1680 cm^{-1} indicate incompletely reacted polyamic acid due to incomplete imidization of two monomers

The FTIR spectrum of PI-Fiber differs from that of the samples synthesized via a non-assembled pathway; the peaks at 1650 cm^{-1} for amide carbonyl stretching and at approximately 3200 cm^{-1} for amide N–H are indicative of residual poly(amic acid), due to incomplete imidization. Other samples synthesized from conditions not satisfying the above factors also showed similar patterns of FTIR spectrums with non-assembled species, indicating that self-assembly and high-temperature conditions are crucial for conversion of functional groups to desired imide bonds (Figure 4.7b).

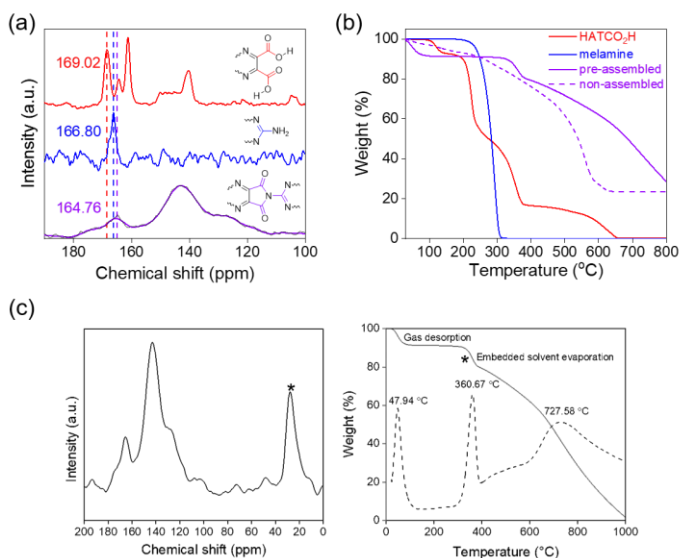


Figure 4.8. Chemical analysis of bond formation in PI-Fiber. (a) ^{13}C nuclear magnetic resonance (NMR) spectra, and (b) Thermogravimetric analysis (TGA) curves of HATCO₂H, melamine, and samples synthesized from pre-assembled (PI-Fiber) and non-assembled species. (c) The residual NMP solvent shown in both spectra is denoted as asterisks.

Solid-State ^{13}C cross polarized magic angle spinning/total sideband suppression (CP-MAS/TOSS) Nuclear Magnetic Resonance (NMR) spectrum also confirmed the generation of imide bonds (Figure 4.8a). Carboxyl carbon peak at 169.02, amine peak at 166.80 ppm decreased, and a new peak at 164.76 ppm, comparable to the imide ring's signal of previously reported polyimides, was appeared¹⁰. The thermal stability of PI-Fiber was tested via Thermogravimetric Analysis (TGA) (Figure 4.8b). Compared to unreacted monomers, and non-fibrous species, PI-Fiber exhibited improved thermal stability, which showed no weight loss between 50 and 350 °C. Aromatic polyimide-based porous organic polymers showed different degrading temperatures depending on morphologies, and PI-Fiber had similar stability with non or partially stacked polyimides¹¹. Elemental analysis of PI-Fibers demonstrated that carbon, nitrogen, and hydrogen weight percentages deviated slightly from the theoretical values (calculated for C₂₁N₁₂O₆: C 48.85, N 32.55, O 18.59; found: C 55.05, H 3.46, N 23.44). This is consistent with the presence of the embedded NMP solvent, as depicted in the ^{13}C solid-state NMR

and TGA curves (Figure 4.8c).

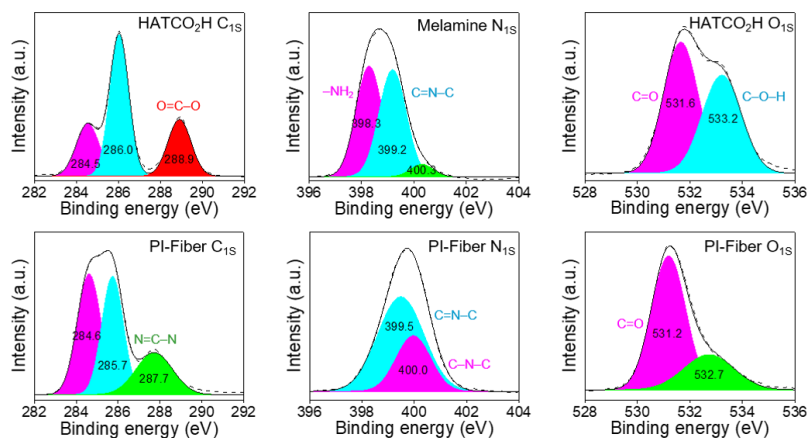


Figure 4.9. High-resolution XPS spectra and C_{1s}, O_{1s} profile of HATCO₂H; N_{1s} profile of melamine; and C_{1s}, N_{1s}, and O_{1s} profile of PI-Fiber.

X-ray photoelectron spectroscopy (XPS) analysis demonstrates that the chemical environments of carbon, nitrogen, and oxygen atoms are significantly altered by the formation of PI-Fibers (Figure 4.9, Appendix 4.3). The C_{1s} peak at 288.9 eV corresponding to the carboxyl group (O=C-O) in HATCO₂H, is diminished by imidization. Additionally, an amine peak (-NH₂) at 398.3 eV in the N_{1s} profile of melamine is shifted to 400.0 eV (C-N-C), implying that all carboxyl and amine groups are consumed into the five-membered imide rings. The O_{1s} profile is also consistent with the complete conversion of the carboxyl moiety (C=O, 531.6 eV and C-O-H, 533.2 eV) to a carbonyl bond in the imide rings (C=O, 531.2 eV).

4.4. Structural characterization of PI-Fiber

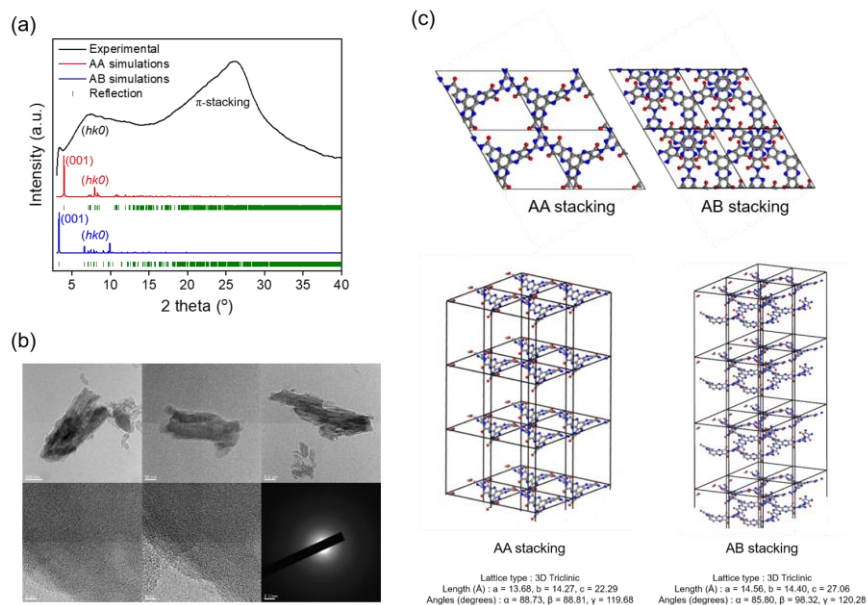


Figure 4.10. Structural analysis of PI-Fiber (PXRD and HR-TEM). (a) Experimental powder X-ray diffraction (PXRD) patterns of PI-Fiber and spectra from the simulated patterns of two stacking models (grey: carbon, blue: nitrogen, and red: oxygen) (b) HR-TEM images of PI-Fiber. No discrete crystallinity was observed as shown in PXRD data. (c) Simulated structures of AA stacking and AB stacking models (grey: carbon, blue: nitrogen, and red: oxygen). The lattice parameter of each model is indicated below. Both structures show desymmetrized (100) and (010) facets and extended layer-layer distance along with z-axis due to the innate distorted shape of the building block.

Powder X-ray Diffraction (PXRD) and N_2 sorption measurements at 77 K determined the structural characteristics of PI-Fiber. The powder samples decomposed into short fibrils via sonication to obtain discrete PXRD peaks (Appendix 4.4). PXRD data of PI-Fiber showed two broad peaks centered at $2\theta = 7.53^\circ$ and 26.14° , reflecting intrinsically poor crystallinity (Figure 4.10a). High-Resolution Transmission Electron Microscope (HR-TEM) images also showed no crystalline patterns in fibril structures (Figure 4.10b). Simulated patterns of two stacking modes (AA stacking and AB stacking models, Figure 4.10c, part above) indicated that diffraction peaks from (hk0) facets in both simulated patterns were well matched with the experimental pattern, representing the formation of designed

microporous structures. The peak at $2\theta = 26.14^\circ$ in experimental patterns, corresponding to the value of about 0.33 nm, agreed with the formal π stacking distance, illustrating that π - π interactions between aromatic groups existed in PI-Fiber. However, when calculated with regularly ordered layers, unstable stacking conformations due to distorted structures caused the extended layer-layer distance in simulated structures (Figure 4.10c, part lower), resulting in the generation of peaks assigned to (001) facets far apart from experimental patterns. From the above data, it could be considered that PI-Fiber constitutes randomly arranged micropores, resulting in fibers without three-dimensional long-range order.

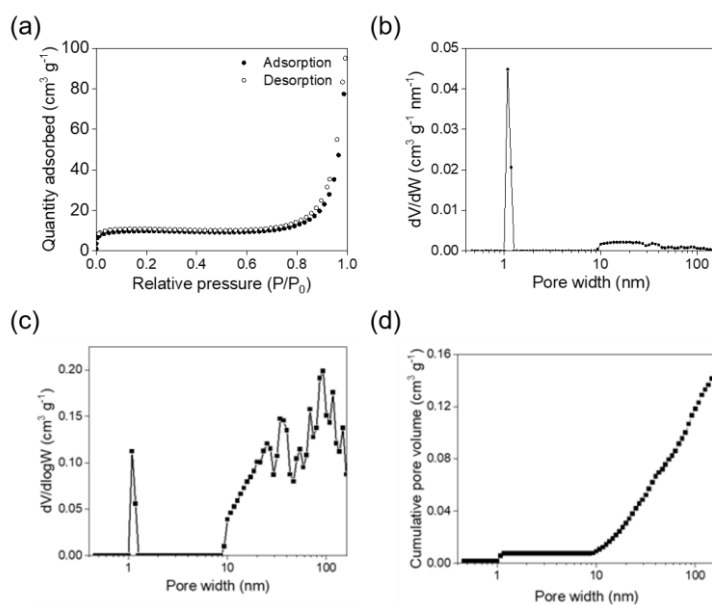


Figure 4.11. Structural analysis of PI-Fiber (micropore analysis). (a) Nitrogen adsorption/desorption isotherms of PI-Fiber at 77K. (b) Pore size distribution analysis of PI-Fiber. (c) Incremental and (d) Cumulative pore volume of PI-Fiber

In addition, pore size distribution data from N₂ sorption measurements demonstrated random packing of intrinsic microporous structures. The nitrogen adsorption isotherm was a type II pattern indicating micro-and mesoporous structures¹² (Figure 4.11a). PI-fiber had a Brunauer-Emmett-Teller (BET) surface

area of $38 \text{ m}^2 \text{ g}^{-1}$, which was calculated in the linear range of $P/P_0 = 0.01$ to 0.1 . Due to irregular packing and consequent decreased ratios of micropores exposed, PI-fiber had a relatively smaller surface area than previously reported porous organic polymers. Pore size distribution estimated from dV/dW showed one prominent peak around 1.1 nm , consistent with the size of the calculated pore size (1.3 nm) (Figure 4.11b). It is worthy to note that the size distribution of micropores is relatively narrow, although they are derived from distorted and non-stackable polymers. The PI-Fiber also shows pores with diameters greater than 9 nm and a large cumulative volume at those regions (Figure 4.11c and 4.11d), suggesting that the fibrils form mesoporous channels that interconnect micropores as illustrated in figure 4.12. As we know, this type of polymer fibrils with inherent porous structures has not been published before, indicating the effectiveness of self-assembly for synthesizing unique and homogeneous systems via bottom-up approaches.

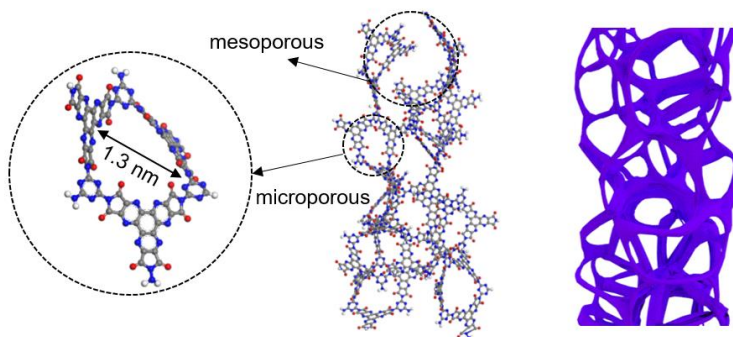


Figure 4.12. The expected structure of protofilaments constituting PI-Fiber and its schematic illustration.

4.5. Electrochemical characterization and application of PI-Fiber for pseudocapacitors

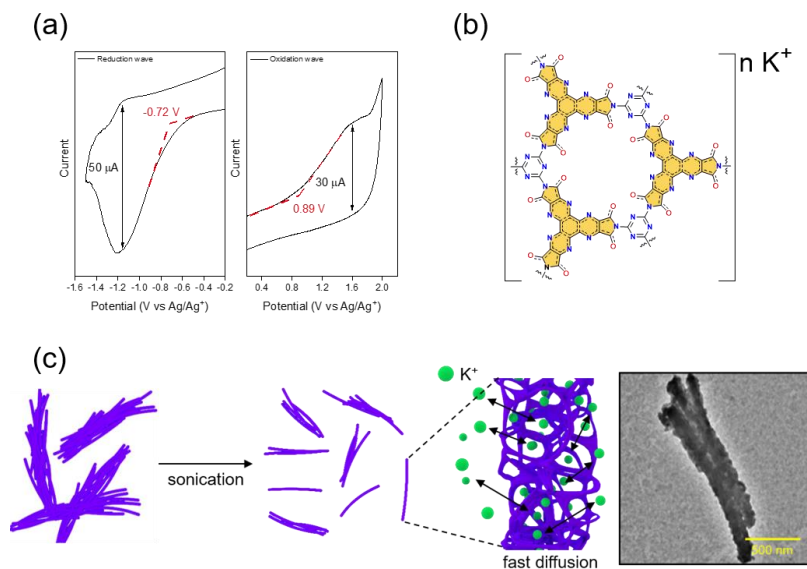


Figure 4.13. Electrochemical application of PI-Fiber and electrode preparation process. (a) The cyclic voltammograms of PI-Fiber. The slurry mixture of active materials, carbon black, and PVDF in ACN was deposited onto a glassy carbon electrode and was used as working electrode. Pt wire and Ag/Ag⁺ electrode (10 mM AgNO₃) were used as counter and reference electrodes, respectively. As electrolytes, 100 mM NBu₄ClO₄ was used in ACN. (b) The molecular structure highlighting conjugated redox-active groups (yellow) composed of heteroatoms (red, blue) (c) Schematic illustration of fibril fragmentation and the expected high ion permeable structure of PI-Fiber (left), TEM image of fragmented PI-Fiber (right).

To explore the suitability of PI-Fiber as an energy storage material, we examined its electrochemical properties. A slurry of PI-Fiber, with carbon black as a conducting agent, and polyvinylidene fluoride (PVDF) as a binder, was sonicated in NMP and deposited onto a glassy carbon electrode. Cyclic voltammetry in acetonitrile showed that the onset potential of the reduction wave was detected at -0.72 V (vs Ag/Ag⁺) (Figure 4.13a). Therefore, the lowest unoccupied molecular orbital (LUMO) level of PI-Fiber is estimated to be -3.99 eV versus the vacuum level. The value is comparable to those of electron-deficient porous organic polymers ($E_{\text{LUMO}} < -3.59$ eV^{13,14}) and hexaazatriphenylene triimide-containing

molecules ($E_{LUMO} = -3.63 \text{ eV}^{15}$). These data suggest that the PI-Fiber can be adapted for electron-accepting negative electrodes (Figure 4.13b). The micro- and mesoporous architectures may facilitate fast diffusion of cations for accepting electrons, which is essential for high power density materials. In addition, several efforts, such as fragmentations or exfoliations, have recently attempted to achieve faster ion diffusion in organic materials^{16,17}. We also anticipated that the nanostructured fibrils (Appendix 4.5) with hierarchical structure may enhance the mobility of internal ions for fast charge and discharge process (Figure 4.13c).

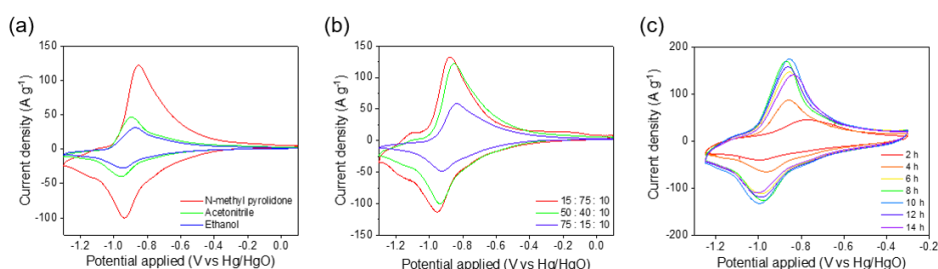


Figure 4.14. CV curves of working electrodes prepared by sonication under various conditions. (a) Solvent effects. The slurry mixture of active materials, carbon black, and PVDF was sonicated for 4–5 h in the specified solvents. (b) The various ratio of the active materials, carbon black, and PVDF. Sonication was conducted in NMP solvent for 4–5 h. The high fraction of the active materials up to 75% reduced charge capacity presumably due to low conductivity of PI-Fiber. Thus, the ratio of 50: 40: 10 was selected as the optimal condition for further measurements. (c) Sonication time. The highest current density was observed after 8–10 h of sonication. All curves were acquired at 100 mV s^{-1} .

The PI-Fibers were fragmented by sonication, and the active materials were mixed with a conducting agent (carbon black) and binder (polyvinylidene fluoride, PVDF). The slurry of the mixture was then drop-casted onto graphitic foil. Using it as a working electrode, we conducted cyclic voltammetry (CV) in a 6 M KOH solution between -0.3 V and -1.25 V vs Hg/HgO. Distinctive reversible peaks were detected at approximately -1.0 V , and the best performance was observed when the active material, conductive agent, and binder were mixed at the ratio of 50: 40: 10, sonicated in NMP solvent for 8–9 h, and deposited onto 1 cm^2 of current collectors (Figure 4.14).

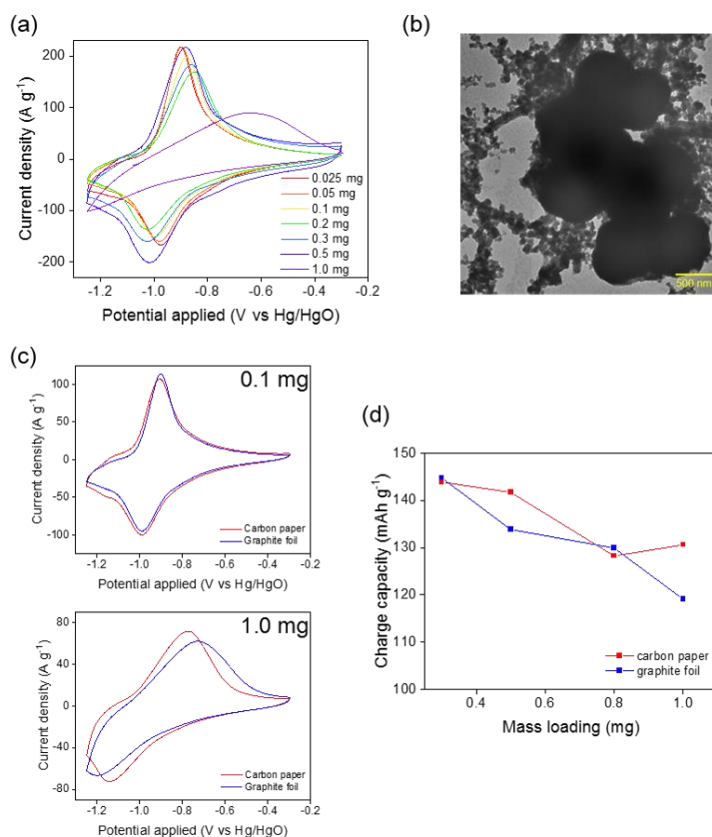


Figure 4.15. Mass loading optimization. The mixture of active materials, carbon black, PVDF at the ratio of 50: 40: 10 was sonicated in NMP for 8–9 h before loading. (a) CV curves measured at 100 mV s^{-1} in the variation of the loaded amounts of the mixtures. The shape of curves and charge capacity retained analogously up to 0.5 mg of loading, but not with 1.0 mg of loading. (b) TEM image of the agglomerated species. (c) The overlaid CV curves recorded with carbon paper (red) or graphite foil (blue) as the substrate. The measurements were conducted at the sweep rate of 50 mV s^{-1} . (top) When 0.1 mg of the samples were loaded, no distinct change was observed. (bottom) With 1.0 mg of loading, significant changes in reversibility and charge capacity were observed with graphite foil, but not with carbon paper. The relatively reversible and high charge capacity with carbon paper might be associated with the high surface area and morphology of carbon paper. (d) Charge capacity against various mass loading and the substrates.

The active material loaded onto graphite foil retained its reversibility and charge capacity up to 0.5 mg loading (Figure 4.15a). Although the higher mass of loading led to a drastic decrease in its capacity, possibly due to the formation of agglomerated species and consequently increased sample thickness (Figure 4.15b). The reversibility and capacity was improved with 1.0 mg of loading when carbon

paper was used as a highly porous electrode (Figure 4.15c). Further optimizations in the selection of substrates, ratio, conducting agents, sonicating conditions, and deposition conditions for high mass loading are under investigation.

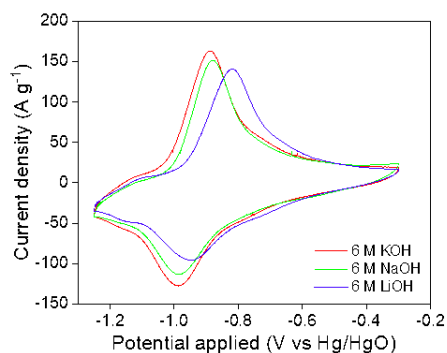


Figure 4.16. CV curves measured at 100 mV s⁻¹ in various electrolytes.

We further conducted the measurements using the graphite foil electrode with 0.5 mg of loading to explore the electrochemical behavior and full capacity of PI-Fiber. Herein, we used potassium-ion instead of sodium or lithium ion because the electrolyte may enhance the charge capacities of PI-Fiber as reported previously¹⁸ (Figure 4.16). All three curves were measured from the same electrode in the order from KOH to LiOH. To avoid any complexity and experimental errors associated with the preparation of the electrode, we re-used the electrode after washing and incubation for 1 h in the solution with electrolytes of our interest prior to the next measurements.

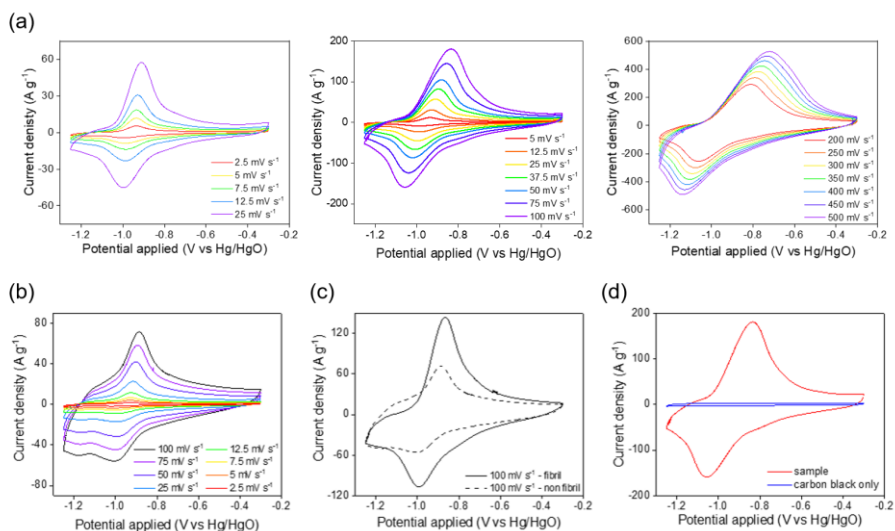


Figure 4.17. CV curves of working electrodes constructed from PI-Fiber or samples synthesized from non-assembled building units. (a) CV curves of working electrodes in a three-electrode system (6 M KOH) at different sweep rates. The curves were measured at the rates of 2.5–500 mV s^{-1} , and only the representative data are shown in figure 4c for clarity. Although the peak shift (V) increased with the faster sweep rates, a distinctive redox couple was observed even at the rate of 500 mV s^{-1} . Comparison of CV curves between fibrous and non-fibrous species. (b) CV curves of non-fibril samples in various sweep rates (2.5–100 mV s^{-1}). (c) The overlaid CV curves with fibril or non-fibril samples after cycling at the sweep rate of 100 mV s^{-1} . These samples were cycled 500 times in the range of -0.1 V and -1.1 V vs Hg/HgO before the CV measurements. (d) CV curves of fibril and carbon black only loaded on the graphitic foil.

The CV curves of PI-Fibrils at different scan rates (2.5–500 mV s^{-1}) showed distinct reversible peaks and only small peak shifts even at high sweep rates (0.2 V with 100 mV s^{-1}) (Figure 4.17a). The electrochemical properties indicate that PI-Fiber functions like a pseudocapacitor, which facilitates surface-controlled process at low sweep rates and diffusion-controlled process at high sweep rates. The current density was significantly reduced when non-fibrous materials or pure carbon black were applied instead (Figure 4.17b to d), representing that conversion to imide networks and fibrinous architecture of PI-Fiber is essential for high energy density materials.

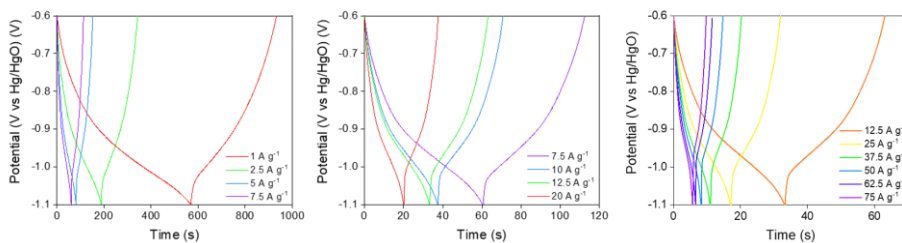


Figure 4.18. Galvanostatic charge and discharge (GCD) curves of working electrodes in three-electrode systems.

Current density (A g ⁻¹)	Specific capacity (mAh g ⁻¹)	Columbic efficiency (%)
1	101.0	63.8
2.5	107.3	82.0
7.5	108.5	85.8
12.5	104.0	89.8
20	98.1	87.6
25	97.2	81.4
37.5	98.4	85.9
50	91.7	79.5
62.5	85.1	74.2
75	83.3	70.2

Table 4.1. Specific capacities and columbic efficiencies at different current densities.

Galvanostatic charge and discharge (GCD) measurements at different current densities (1–75 A g⁻¹) also demonstrated that PI-Fiber operates as a pseudocapacitor (Figure 4.18). Symmetrical GCD curves with plateaus at -0.9 V vs Hg/HgO were consistent with the CV redox peaks. Due to non-linear charge-discharge behavior, we could not calculate the specific capacitance (F g⁻¹) of our materials¹⁹; instead, charge capacity was estimated up to 107.3 mAh g⁻¹ at 2.5 A g⁻¹ between -0.6 V and -1.1 V. The high charge capacity was retained even at higher current densities of 83.3 mAh g⁻¹ at 75 A g⁻¹ (Table 4.1), which is comparable to the values of recently developed high-performance organic pseudocapacitors in the works of literature.

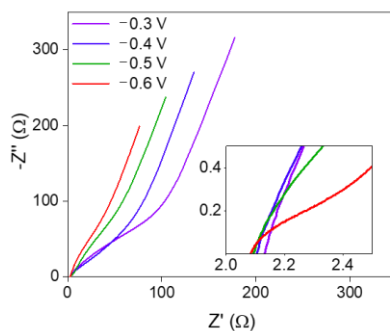


Figure 4.19. Nyquist plot from 10 kHz to 20 mHz at different offset voltages (inset: high resolution image of semicircle region).

We also carried out electrochemical impedance spectroscopy (EIS) measurements in a 6 M KOH solution to explore the charge storage mechanism (Figure 4.19). In the Nyquist plot, a semicircle was generated at high-frequency domain with an increasing applied voltage, indicating that it is converted from electronic double-layer capacitor (EDLCs) to redox-active pseudocapacitor. The small radius of a semicircle combined with a large slope at a low-frequency regime represented that our system exhibited low charge-transfer resistance and fast diffusion of potassium ion, proving its fast kinetics at the electrode/electrolyte interface.

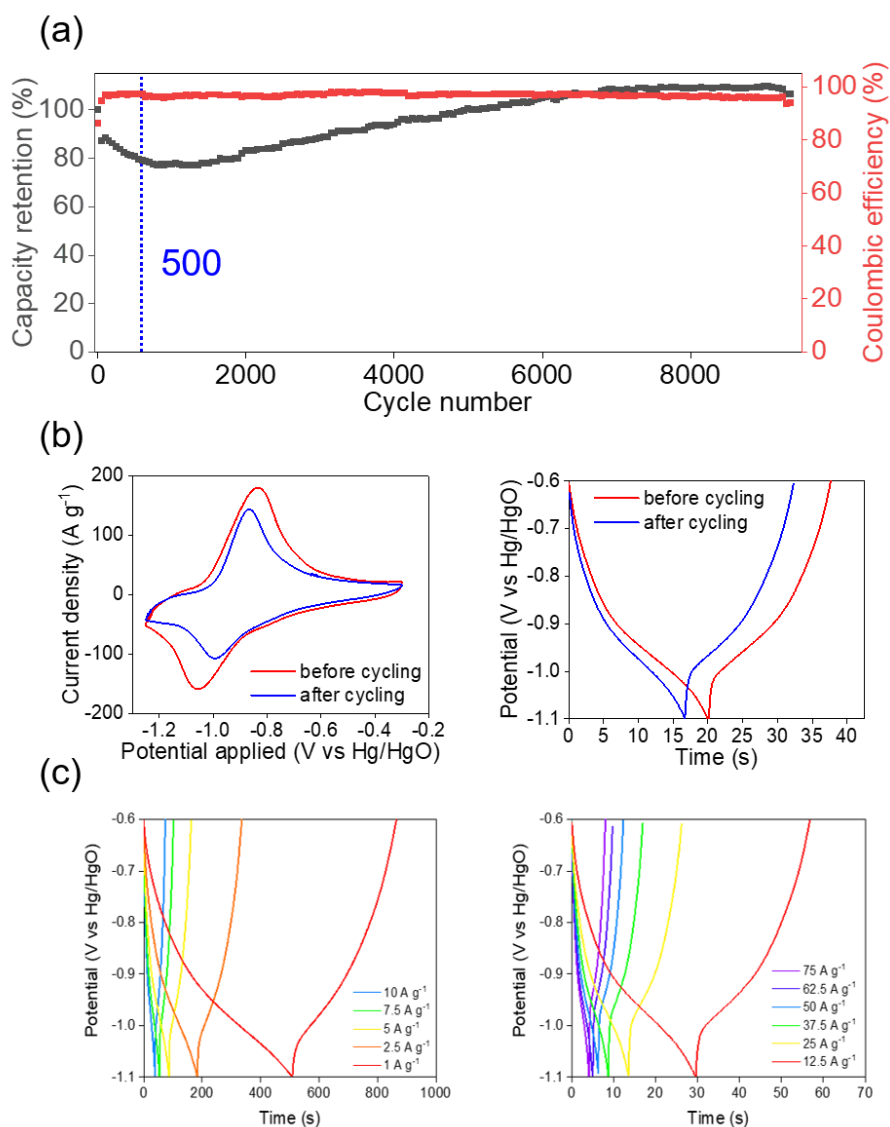


Figure 4.20. Stability test and electrochemical properties of PI-Fiber before and after cycling. (a) Cyclability test of PI-Fiber at $20\ A\ g^{-1}$. (b) (Left) CV and (right) GCD curves after 500 cycles. (c) GCD curves of the cycled electrode at different current densities ($1\text{--}75\ A\ g^{-1}$).

We tested the stability of PI-Fiber by repeating multiple cycles of charging/discharging in the range of $-0.1\ V$ and $-1.1\ V$ vs Hg/HgO at the current density of $20\ A\ g^{-1}$ (Figure 4.20a). The cycling test represented PI-Fiber exhibited fast decrease in capacity and retained about 80 % of total capacity after 500 cycles repeated; then, maintained its stability for further cycling with a slight increase, presumably due to surface reconstruction. The CV curves of the 500 time-cycled

electrode at a scan rate of 100 mV s^{-1} showed a slight reduction in the charge capacity and narrower redox peaks as compared to the freshly prepared electrode (Figure 4.20b). The GCD curves of the cycled electrode over 0.5 V (-1.1 V to -0.6 V vs Hg/HgO) were also marginally perturbed with lower charge capacity than the non-cycled one (Figure 4.20c). However, the cycled electrodes still exhibited remarkably high charge capacity at high current densities; 86.7 mAh g^{-1} at 20 A g^{-1} and 81.3 mAh g^{-1} at 75 A g^{-1} over 0.5 V with enhanced coulombic efficiency, which is comparable to the values of recently developed high-performance organic pseudocapacitors in the works of literature. (Figure 4.20d, Table 4.2 and Table 4.3).

Current density (A g^{-1})	Specific capacity (mAh g^{-1})	Coulombic efficiency (%)
1	99.0	70.2
2.5	106.5	84.2
5	105.1	87.5
7.5	100.4	90.3
10	97.8	91.4
12.5	94.4	91.9
20	86.7	93.4
25	88.2	94.1
37.5	85.4	94.3
50	83.3	95.2
62.5	81.6	94.0
75	81.3	95.1

Table 4.2. Specific capacities and coulombic efficiencies of the cycled electrode at different current densities.

Species	Current density (A g ⁻¹)	Applied potential (voltage range)	Electrolyte	Charge capacity (mAh g ⁻¹)	Capacitance (F g ⁻¹)	Reference
PI-Fiber (Freshly-prepared)	2.5	-1.1 V ~ -0.6 V (vs Hg/HgO) (0.5 V)	6.0 M KOH	107.3	773	This work
	20			98.1	706	
	75			83.3	600	
PI-Fiber (500 times cycled)	2.5	-1.1 V ~ -0.6 V (vs Hg/HgO) (0.5 V)	6.0 M KOH	106.5	737	This work
	20			86.7	624	
	75			81.3	585	
AAm-TPB	1	0.2 V ~ 0.9 V (vs Ag/AgCl) (0.7 V)	1.0 M H ₂ SO ₄	52.7	271	20
CNT/NKCOF-2	0.5	-0.1 V ~ 1.0 V (vs Ag/AgCl) (1.1 V)	2.0 M H ₂ SO ₄	134.4	440	21
	20			66	216	
CNT/NKCOF-8	1	-0.2 V ~ 0.9 V (vs Ag/AgCl) (1.1 V)	2.0 M H ₂ SO ₄	72.7	238	21
	20			45.8	150	
PHATN	0.5	-1.1 V ~ -0.6 V (vs Hg/HgO) (0.5 V)	6.0 M KOH	95.7	689	22
	20			80.1	577	
	75			60	432	
4KT-TpCOF	0.2	0 V ~ 0.6 V (vs Ag/AgCl) (0.6 V)	1.0 M H ₂ SO ₄	97.2	583	23
	1			45.7	274	
	10			25.3	152	
TPT-DAHQ COF	0.5	-1.0 V ~ -0.1 V (vs Ag/AgCl) (0.9 V)	1.0 M KOH	78.2	313	24
	20			40	160	
Porous-1	0.2	-0.85 V ~ -0.35 V (vs Ag/AgCl) (0.5 V)	1.0 M Na ₂ SO ₄	49	353	25
	1			29.7	214	
	10			10	72	
Porous-2	0.2	-0.9 V ~ -0.45 V (vs Ag/AgCl) (0.45 V)	1.0 M Na ₂ SO ₄	29.8	238	25
	1			26.6	213	
	10			17.3	138	
TaPa-(OH) ₂	0.5	-0.2 V ~ 0.5 V (vs SCE) (0.7 V)	1.0 M Phosphate	80.9	416	26
TPDA-1	0.5	0 V ~ 1.0 V (vs SCE) (1.0 V)	1.0 M H ₂ SO ₄	96.7	348	27
	5			48.6	175	
TDFP-1	0.5	-0.5 V ~ 0.5 V (vs SCE) (1.0 V)	0.1 M H ₂ SO ₄	116.1	418	28
DAAQ-TFP-COF	0.1	-0.3 V ~ 0.3 V (vs Ag/AgCl) (0.6 V)	1.0 M H ₂ SO ₄	8	48	29
N-MPC	0.5	-1.0 V ~ 0 V (vs SCE) (1.0 V)	6.0 M KOH	140.3	505	30
	1			58.6	211	
	10			28.1	101	
HM-COF	0.5	0 V ~ 0.5 V (vs SCE) (0.5 V)	6.0 M KOH	20.1	145	31
	10			9.7	70	
POF-800	0.25	-1.0 V ~ -0.1 V (vs Ag/AgCl) (0.9 V)	6.0 M KOH	12.5	50	32
	10			2.8	11	
CPP	1	0 V ~ 0.45 V (vs Hg/HgO) (0.45)	6.0 M KOH	71.4	571	33
	10			39.6	317	
	1			39.5	316	
c-CNT@COF	0.2	-0.3 V ~ 0.3 V (vs Ag/AgCl) (0.6 V)	0.5 M H ₂ SO ₄	69.8	419	34
	0.5			62.7	376	
BIBDZ	0.5	0 V ~ 1.0 V (vs SCE) (1.0 V)	1.0 M H ₃ PO ₄	24.6	89	35
	10			11.9	43	

Table 4.3. Comparison of charge capacity (mAh g⁻¹), and capacitance (F g⁻¹) between PI-Fiber and materials in previously reported literature.

BPY-CTF				109.3	393	
CTF-1				61.2	220	
DCE-CTF	0.5	-1.0 V ~ 0 V (vs Hg/HgO)	1.0 M KOH	77.8	280	36
DCP-CTF		(1.0 V)		90.1	324	
PyrOxin POP	1	0 V ~ 0.45 V (vs Hg/HgO)	6.0 M KOH	65.2	522	
	5	(0.45 V)		52.6	421	37
	10			42.8	342	
An-CPOP-1		-1.0 V ~ 0.5 V (vs Hg/HgO)	1.0 M KOH	30.1	73	
An-CPOP-2	0.5	(1.5 V)		41	98	38
TFP-NDA-COF	0.5	0 V ~ 1.0 V (vs SCE)	1.0 M H ₂ SO ₄	96.7	348	39
		(1.0 V)				
FCTF	1	0 V ~ 0.8 V (vs Ag/AgCl)	1.0 M H ₂ SO ₄	70.9	319	
	5	(0.8 V)		66.7	300	40
	10			58.4	263	
PPrGO-2				80.1	360	
PPrGO-1		-0.2 V ~ 0.6 V (vs Ag/AgCl)	1.0 M KOH	59.2	266	
PPrGO-3	3	(0.8 V)		55.9	252	41
PPrGO-4				52.4	236	
CAP-1		0 V ~ 1.0 V (vs SCE)	2.0 M KCl	66.7	240	
CAP-2	1	(1.0 V)		22.2	80	42
PAQTA	1	0.2 V ~ 0.8 V (vs Ag/AgCl)	0.5 M H ₂ SO ₄	96	576	
	10	(0.8 V)		68.3	410	43
TPA-COFs	0.1	0 V ~ 1.0 V (vs SCE)	1.0 M H ₂ SO ₄	73.1	263	
	5	(1.0 V)		45.3	163	44
TNNs-550	0.2	-0.2 V ~ 0.8 V (vs Ag/AgCl)	1.0 M H ₂ SO ₄	82.8	298	
	10	(1.0 V)		48.1	173	45
PYBDA	0.5	-0.2 V ~ 0.6 V (vs SCE)	2.0 M H ₂ SO ₄	101.3	456	46
		(0.8 V)				
POPM-TFP	0.5	0 V ~ 0.5 V (vs Hg/HgO)	2.0 M KOH	24.7	178	
	8	(0.5 V)		10.7	77	47
TPPDA-TPTPE COF		-0.92 V ~ 0.18 V (vs Hg/HgO)	1.0 M KOH	72.4	237	
TPPDA-TPPyr COF	2	(1.0 V)		57.7	189	48
Pyrene-CTF-10		-1.0 V ~ 0 V (vs Hg/HgO)	1.0 M KOH	105.6	380	
Pyrene-CTF-20	0.5	(1.0 V)		138.9	500	49
CC-DAQ-CMP	1	-1.2 V ~ -0.5 V (vs SCE)	6.0 M KOH	35.8	184	
	10	(0.7 V)		17.2	88	50
DAAQ-COFs/GA	1	-0.5 V ~ 0.5 V (vs SCE)	1.0 M H ₂ SO ₄	105	378	
	20	(1.0 V)		89.4	322	51
	70			85.6	308	
TAT-CMP-1	1			39.2	141	
	10	-1.0 V ~ 0 V (vs Hg/HgO)	1.0 M Na ₂ SO ₄	27.5	99	
TAT-CMP-2	1	(1.0 V)		50.8	183	52
	10			38.1	137	
PDC-MA-COF	1	0 V ~ 0.6 V (vs Ag/AgCl)	6.0 M KOH	37.2	335	
	10	(0.6 V)		27.6	248	53

Table 4.3. Comparison of charge capacity (mAh g⁻¹), and capacitance (F g⁻¹) between PI-Fiber and materials in previously reported literature. Capacitance values represented are all calculated by following equations;

$$\text{Capacitance (F g}^{-1}\text{)} = \text{Charge capacity (A s g}^{-1}\text{)} / \text{Applied potential (V)}.$$

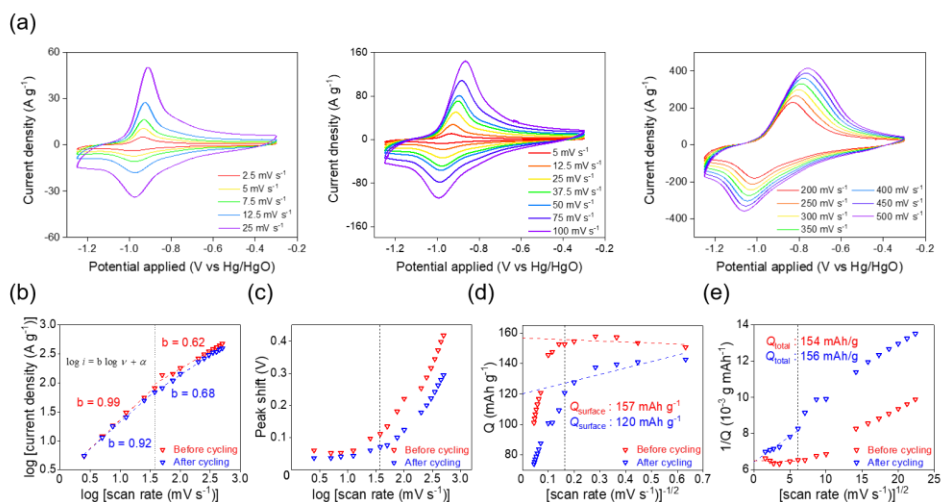


Figure 4.21. Electrochemical properties of PI-Fiber before and after cycling. (a) CV curves of cycled electrode at different scan rates (2.5–500 mV s⁻¹). All other experimental conditions were the same as above. (b) logarithm of anodic current density versus logarithm of scan rate. (c) Peak shift of redox couples ($E_{p,a} - E_{p,c}$) versus log (scan rate). (d) Plot of charge capacity (Q) calculated from CV versus (scan rate)^{-1/2}, with extrapolation to estimate outer charge storage. (e) Q⁻¹ versus (scan rate)^{1/2}, with extrapolation to calculate overall charge storage. All experiments were conducted at scan rates between 2.5 and 500 mV s⁻¹ to compare the as-prepared and 500-times cycled electrodes. The scan rate corresponding to 37.5 mV s⁻¹ is shown as a dashed line in figures (b)–(e).

The electrochemical performance of the stabilized electrode was also tested via CV at different scan rates (2.5 – 500 mV s⁻¹, Figure 4.21a) to understand the remarkable kinetics of charge storage and the mechanism of fast decay. Variables acquired from CV data were compared between primary and cycled electrodes. Peak current value in a CV curve is relative to scan rate (v) by the following equation: $i \propto v^b$ or $\log i = b \log v + \alpha$. Log-log plot of oxidative current density (A g⁻¹) and scan rate (mV s⁻¹) was described in figure 4.21b. The b values, the slope of the linear fit, were close to 1 in both electrodes at low sweep rates, meaning surface-controlled kinetics in charge storage. As increasing the sweep rate, b values approached 0.5, indicative of diffusion-limited processes. Figure 4.21c showed changes of peak shifts (V) in redox couples ($E_{p, \text{anodic}} - E_{p, \text{cathodic}}$) as a function of log v . Low peak separation values at slow sweep rates in both electrodes indicated that both electrodes behaved in surface-controlled mechanism

as mentioned above. More significant peak shifts (V) with increasing sweep rates implied conversion to the diffusion-controlled mechanism. From figure 4.21b and 4.21c, scan rates where the transition from surface-controlled kinetics to diffusion-controlled kinetics occurred were relatively high in both electrodes, demonstrating pseudocapacitive behavior with fast charge storage kinetics.

We also could notice relatively higher peak separation values with the pristine electrode, which could be attributable to broad peaks in CV. Peak broadening is attributed to increased lateral interaction between the surface adsorbates⁵⁴ and narrowed peaks observed in the cycled electrodes indicated changes in the surface environment during cycling. The contributions of external charge storage and internal charge storage to the total charge storages were compared among electrodes to identify its internal structural change^{6,19} (Figure 4.21d and 4.21e). Surface charge capacity (Q_{surface}) was estimated by extrapolating the plot of Q (charge capacity) values from CV curves versus $v^{-1/2}$ to infinite scan rate ($v \rightarrow \infty$). Total charge capacities were calculated from extrapolation of inversed plots (Q^{-1} vs $v^{1/2}$) to zero scan rate ($v \rightarrow 0$). Interestingly, the total charge values of both electrodes were the same, meaning no discrete chemical decomposition of the electrode during cycling (154 mAh g⁻¹, 156 mAh g⁻¹, respectively). However, the surface charge value of the cycled electrode was decreased to 120 mAh g⁻¹ (77 %), whereas the new electrode retained its capacity (157 mAh g⁻¹). This indicated that the hierarchical pores in PI-Fiber enabled 100 % of active materials to be in electrolyte-accessible regions. However, profoundly intercalated potassium ions could not be reversibly deintercalated with continuous cycling, preventing mass transfer at high sweep rates. The charge capacity values were not reduced prominently at low sweep rates (< 12.5 mV s⁻¹), verifying the above assumptions. Together, taking advantage of the unique structure of PI-Fiber, the material exhibiting fast charge storage ability was created. Despite its drastic decrease in capacity by surface morphology change, the stabilized electrodes still had high charge capacity at the high current densities, which exceeds most of the

other previously reported organic pseudocapacitors.

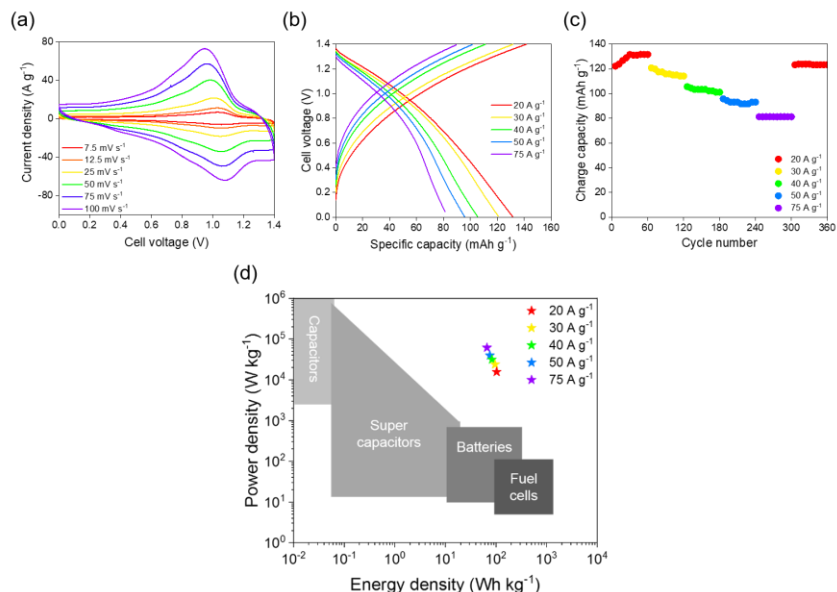


Figure 4.22. Electrochemical analysis of PI-Fiber in two-electrode system. (a) CV curves of the AC//PI-Fiber two-electrode cell at different scan rates. (b) GCD curves and specific charging and discharging capacities of two-electrode cell at high current densities. (c) The retention of charge capacity from the cycling test of the AC//PI-Fiber. (d) Ragone plot of AC//PI-Fiber. Specific energy densities and power densities were calculated by using the mass of the active material, not a whole device.

We assembled an asymmetric supercapacitor cell in a two-electrode system using our active materials as a negative electrode and activated carbon (AC) as a positive electrode to test PI-Fiber's potential application in practical devices. Stability is an important issue for practical applications; thus, 500 times cycled electrode were considered suitable species for two-electrode device manufacturing. The electrochemical properties of the AC//PI-Fiber device were tested with CV in the cell voltage range of 1.4 V (Figure 4.22a). CV curves at different sweep rates (7.5–100 mV s⁻¹) had similar aspects with three-electrode measurements, showing one prominent and reversible redox pairs. The charge-discharge profiles were tested only at high current densities (20–75 A g⁻¹) considering our material's low columbic efficiencies at low current densities and practical application of pseudocapacitor (Figure 4.22b). Current densities were calculated by dividing

applied currents into the mass of active materials, not the whole device. A charge capacity of 131.7 mAh g⁻¹ at 20 A g⁻¹ was estimated at 1.4 V of operating voltage, and the cell still exhibited a high capacity of 81.3 mAh g⁻¹ even at 75 A g⁻¹. The device nearly recovers its maximum capacity of 124.1 mAh g⁻¹ at a current density of 20 A g⁻¹, even after multiple cycles with changing current density (Figure 4.22c). Furthermore, the maximum energy density of 103.2 Wh kg⁻¹ (at 20 A g⁻¹) and the maximum power density of 61.2 kW kg⁻¹ (at 75 A g⁻¹) were calculated from discharge curves (Figure 4.22d, Table 4.4). These data demonstrate that the PI-Fiber in the two-electrode system retain high performance, similar to that of a three-electrode system, indicative of a prospective electrochemical material for practical applications.

Current density (A g ⁻¹)	The energy density (Wh kg ⁻¹)	Power density (kW kg ⁻¹)
20	103.2	15.7
30	96.0	23.8
40	83.3	31.6
50	75.9	39.6
75	66.3	61.2

Table 4.4. The electrochemical performance of AC//PI-Fiber.

4.6. Conclusion

In summary, we have successfully synthesized redox-active polyimide, PI-Fiber, using melamine and hexaazatriphenylene carboxylic acid, which was an unprecedented combination for making porous organic polymers. Two-step synthesis was critical for generating uniform fibrous structures both in chemically and morphologically. PI-Fiber constituted of uniform micropores connected with mesoporous channels indicating its hierarchical structures. Due to highly permeable and fibrous structures, our materials achieved a high charge capacity even at ultra-high current density, testified by nearly 100 % of estimated $Q_{\text{outer}}/Q_{\text{total}}$ value. Despite its slight decrease in capacity after hundreds of cycles, high capacity was maintained over thousands of cycles and recovered with surface reconstruction. The two-electrode cell, AC//PI-Fiber, was also constructed and tested, verifying its high power and energy density at high current density, as demonstrated in a three-electrode system. This high and fast charge storage can be attributable to the unique hierarchical structure of PI-Fiber, which could not be generated without two step synthesis. In particular, our work reveals the possible versatility of hexaazatriphenylene triimide moieties as a promising skeleton for energy-storage materials. Conjugation of HATCO₂H with various amine molecules containing highly redox-active groups could potentially diversify the structure and function of POPs; thus, other types of hierarchical materials may enrich the field of energy storage and related applications. This study showed the importance of structures and morphologies in designing energy storage materials and the effectiveness of self-assembly methods for generating unique structures not considered or tested unprecedentedly.

4.7. Experimental section

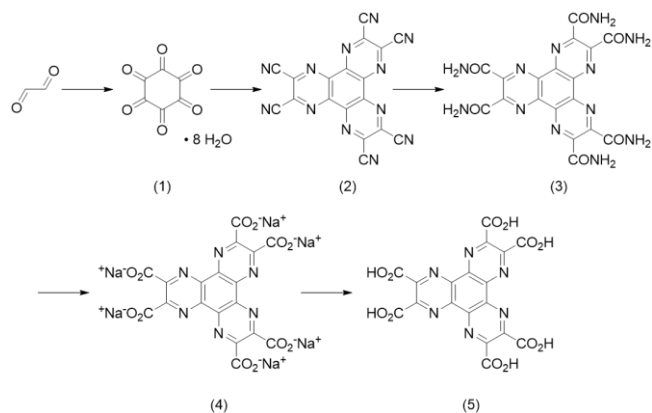
Materials

Melamine, glyoxal, potassium hydroxide (KOH), sodium hydrogen carbonate (NaHCO_3), sodium sulfite (Na_2SO_3), diaminomaleonitrile, sodium nitrite (NaNO_2), glacial acetic acid, mesitylene, isoquinoline, N-methyl-2-pyrrolidone (NMP), dimethylacetamide (DMAC), 1,3-dimethyl-2-imidazolidinone (DMI), dimethylsulfoxide (DMSO), graphitic foil, carbon black, and activated carbon were purchased from Thermo Fischer scientific. Concentrated hydrogen chloride (HCl), sulfuric acid (H_2SO_4), trifluoroacetic acid, and activated charcoal were supplied from the DAEJUNG chemical. Ethyl alcohol (EtOH), methyl alcohol (MeOH), ethyl acetate (EA), dichloromethane (DCM), diethyl ether, acetone, and hexane were purchased from SAMCHUN chemical and DAEJUNG chemical in analytical grades. Silver nitrate (AgNO_3) and tetrabutylammonium perchlorate (NBu_4ClO_4) were supplied from Sigma-Aldrich. All chemicals were used without further purification unless noted.

Commercially available electrodes (Ag/Ag⁺ reference electrode, Hg/HgO reference electrode, glassy carbon electrode) were provided by Qrins. Pt wires were purchased from 4science.net. All solutions used in electrochemical experiments were made in the laboratory and filtered through a 0.22 μm size filter before usage.

Synthesis and characterization of 1,4,5,8,9,12-hexaazatriphenylene hexacarboxylic acid (HATCO₂H)

The synthesis of HATCO₂H was according to previously published procedures with slight modifications^{55,56}.



Scheme 4.2. Synthesis of 1,4,5,8,9,12-hexaazatriphenylene hexacarboxylic acid.

Synthesis of hexaketocyclohexane octahydrate (**1**) was carried out by following the previously reported procedure⁵⁷. NaHCO₃ (60 g) and Na₂SO₃ (160 g) dissolved in 1200 ml of ddH₂O were heated to 40 °C. The solution described above was stirred and mixed with 192 ml of glyoxal while air bubbling. After 1 h stirring, the darkened suspension was heated to 90 °C at a rate of 1 °C min⁻¹. Then, air bubbling stopped, and the resulting suspension was further incubated at 120 °C for 15 min, then cooled to room temperature. After overnight incubation, the dark suspension was filtered, and the resulting precipitant was washed with ddH₂O and MeOH. After drying under air, the precipitant was added portionwise into 80 ml of 25 % aqueous HNO₃ solution at 0 °C. Further incubation at -20 °C resulted in the precipitation of white solid. After filtration, 6 g of the desired product was obtained.

The mixture of 5 g of (**1**) and 13 g of diaminomaleonitrile in 600 ml of glacial acetic acid was refluxed for 3 h. The resulting suspension was cooled to room temperature, filtered, and washed with acetic acid. Absolute drying under vacuum condition yielded 4.8 g of dark-colored precipitant (**2**), which was used without further purification.

A solution of 4.8 g of (**2**) in 150 ml of 98 % H₂SO₄ was vigorously stirred for 3 d at room temperature. The suspension was then poured into 2 L of ice-cold ddH₂O, then centrifuged at 5000 rpm. The pelletized sample was collected, washed with

ddH₂O, and dried at 100 °C to yield 6.2 g of **(3)** as gray-black solid.

To a stirring suspension of 6.2 g of **(3)** in 190 ml of trifluoroacetic acid, 8.8 g of NaNO₂ was added portionwise for 15 min at 0 °C. The reaction mixture turned to reddish color with gas generation. Glacial acetic acid (190 ml) was further added to the suspension, then stirred for 18 h at room temperature. The reaction mixture was treated with 370 ml of ddH₂O, and the colloidal suspension was centrifuged at 5000 rpm. After removing the supernatant, the remaining solid was dissolved in aqueous NaHCO₃ solution (24 g in 180 ml ddH₂O), and the resulting reddish suspension was filtered. The filtrate was treated with activated charcoal, heated to 100 °C, and stirred for 30 min. The mixture was then filtered, and the filtrate was added to NaOH solution (24 g in 120 ml ddH₂O). After that, addition of 30 ml of EtOH to the cooled mixture precipitated light yellow colored solids, which was then filtered to yield 6.2 g of sodium salts of hexaazatriphenylene hexacarboxylate **(4)**.

The aqueous suspension of sodium hexaazatriphenylene hexacarboxylate salts (5 g in 150 ml) were heated to 50 °C, acidified by adding 150 ml of concentrated HCl and stirred for 1 h at 90 °C. After cooling the solution, the crude mixture was filtered and washed with ddH₂O to yield 3.7 g of HATCO₂H **(5)** as a white powder.

The ¹³C NMR spectra of HATCO₂H was recorded on a Varian 500 (Varian), and the data are consistent with the previously reported values (Figure 4.23)⁵⁸

Liquid Chromatography Electrospray Ionization Mass Spectroscopy (LC-ESI-MS) spectra were recorded on 1260 Infinity LC/6120 Quadrupole LC-MS (Figure 4.24); Calculated for C₁₈H₆N₆O₁₂, 498.27; Observed: [M + H]⁺ = 499.0, [M + H₂O]⁺ = 516.0.

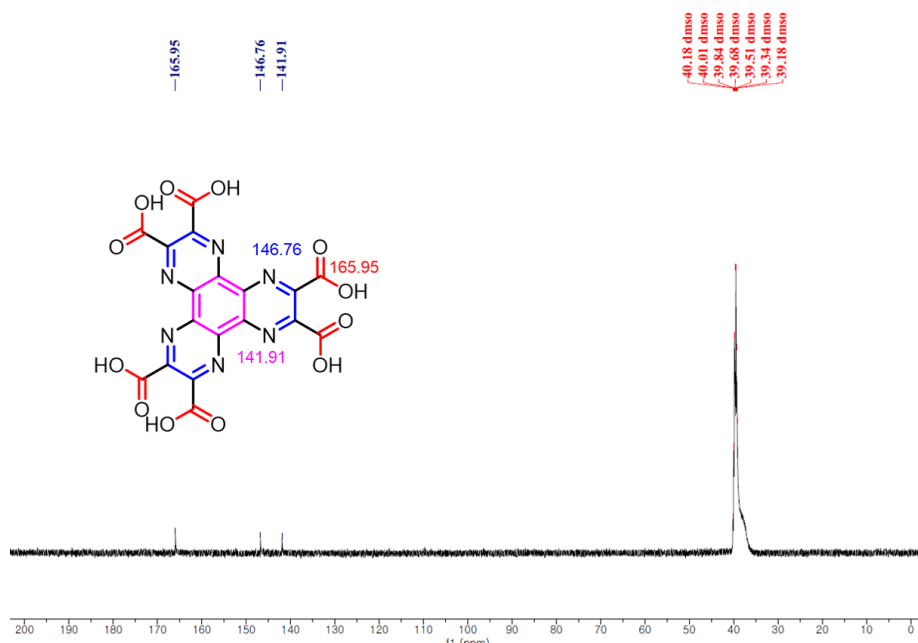


Figure 4.23. ^{13}C NMR spectrum of HATCO₂H (500 MHz, [D₆]DMSO): δ =165.95 ppm (CO₂H), 146.76 ppm (external Ar), 141.91 ppm (internal Ar).

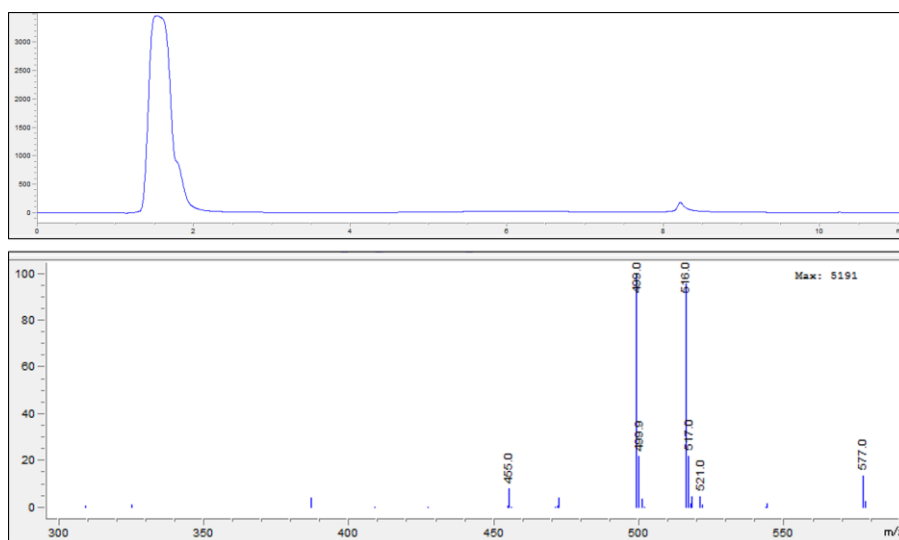


Figure 4.24. Liquid chromatography and mass spectroscopy spectrum of HATCO₂H. MS (EI) m/z calculated for C₁₈H₆N₆O₁₂, 498.27 m/z (%): 498.0 (100), 499 (19.5), 500 (2.5). Found: 499.0 (100), 499.9 (22.5), 500 (3.6) [M + H]⁺, 516.0 (100), 517.0 (22.5), 518 (2.6) [M + H₂O].

Synthesis of PI-Fiber

The mixture of HATCO₂H (100 mg) and melamine (25.2 mg) in 16 ml of anhydrous N-methyl-2-pyrrolidone (NMP) was vigorously stirred for 24 h at 75 °C under Ar. Pale yellow precipitant was initially formed and slowly solubilized to form a dark-colored solution as shown in figure 1c. After the addition of 1 ml of mesitylene and isoquinoline, the resulting solution was incubated for 2–3 days at 200 °C. After filtration, washing with NMP, ethanol, dichloromethane, acetone, ethyl acetate, hexane, and methanol, and drying under vacuum at 200 °C, dark-colored solids (**PI-Fiber**) were isolated (46.3 mg, 37 %).

TEM and SEM images of PI-Fiber

Carbon-coated 200-mesh copper grids (CF200-Cu) were purchased from Electron Microscopy Sciences and were directly applied to sample preparation without any treatment. TEM was operated at HITACHI H-7600 (HITACHI-Science & technology, 120 kV), using AMTV542 software. Field-effect scanning electron microscopy (FE-SEM) images were acquired using HSM-6700F (JEOL Ltd, Japan) installed at the national center for inter-university research facilities (NCIRF) at Seoul national university (SNU) at an accelerating voltage of 5 kV. Before each measurement, samples loaded onto carbon tapes were sprayed by the platinum ion beam.

FT-IR, ¹³C NMR, XPS and TGA of PI-Fiber

Fourier Transform Infrared (FT-IR) experiments were conducted using Spectrum Two (PerkinElmer) in reflection mode in the range of 600–4000 cm⁻¹.

Solid-State ¹³C Cross-Polarization Magic Angle Spinning/Total suppression Of Spinning Sidebands (CP-MAS/TOSS) NMR spectra were acquired between -20 ppm and 240 ppm using 500 MHz Bruker Avance III HD (Bruker, German) installed at NCIRF at SNU at the spinning rate of 5 kHz.

The C, H, N element ratio was analyzed by Micro CHNS (TruSpec) installed at Seoul National University Chemical & Biological Engineering Research Facilities.

X-ray Photoelectron Spectroscopy (XPS) was conducted by screening pelletized samples using AXIS SUPRA (Kratos, UK) installed at NCIRF at SNU at a base pressure under 5×10^{-8} Pa.

The thermal stability of samples was examined using Discovery TGA (TA Instruments, USA) installed at National Instrumentation Center for Environmental Management (NICEM) at SNU. Temperature between 25 °C and 800 °C was applied at the heating rate of 10 °C min⁻¹ under dinitrogen conditions.

PXRD and N₂ adsorption of PI-Fiber

Powder X-ray Diffraction (PXRD) patterns were measured using SmartLab (Rigaku) installed at NCIRF at SNU with a 3kW of X-ray generator (Cu target) and D/teX Ultra250 detector. The pore structure of PI-Fiber calculated from Density Functional Theory (DFT) was determined by Accelrys Materials Studio 8.0 software package. DFT calculation for geometry optimization was conducted by using GGA PBE (General Gradient Approximation applying Perdew-Burke-Ernzerhof) functional with Dmol3 tools. The simulated structures of AA and AB stacking models were acquired from Castep tools in Accelrys Materials Studio 8.0 software package. Castep geometry optimization with fixed basis quality was carried out using GGA PBE functional to optimize unit cell.

Brunauer-Emmett-Teller surface area and micropore size analysis were measured from N₂ adsorption-desorption kinetics conducted at 77 K by Micromeritics (3Flex) installed at KAIST analysis center for research advancement (KARA). The pore size distribution was calculated from the nonlocal density functional theory (NLDFT) method. The samples were degassed at 200 °C for more than 8 h under vacuum.

High-resolution transmission electron microscopy (HR-TEM) images were acquired using JEM-3010 (HEOL Ltd, Japan) installed at NCIRF at SNU with an acceleration electron voltage of 300 kV.

Electrode fabrication and electrochemical properties in three electrode system

Cyclic voltammetry and galvanostatic charge and discharge measurements were performed using Autolab PGSTAT101 and were analyzed with a NOVA software. Three electrode-setup was assembled using the hand-made graphitic foil electrode as a working electrode, Pt wire or hand-made activated carbon electrode as a counter electrode, and Hg/HgO electrode in 20 % (w/v) aqueous KOH solution as a reference electrode. Electrochemical experiments were conducted under argon atmosphere.

Hand-made graphite foil electrodes were prepared as follows; 3 mg of the mixture containing active material, carbon black, and polyvinylidene fluoride was suspended in 0.6 ml of NMP and sonicated. The resulting slurry was then drop cast onto graphitic foil and dried overnight at room temperature. 0.5 mg of sample in total was loaded, and the rest of the electrode surface was sealed with adhesives (Loctite@Hankel).

Electrochemical impedance spectroscopy was carried out with VSP-300 potentiostat (BioLogic). The Nyquist diagram was plotted against the indicated offset voltage in the frequency range of 10 kHz and 20 mHz with a sinus amplitude of 10 mV.

The asymmetric two-electrode cell was made using the above working electrode as a negative electrode and an activated carbon electrode as a positive electrode in aqueous 6 m KOH solution.

We calculated HOMO, LUMO levels of PI-Fiber by using $E_{\text{oxi, onset}}$, $E_{\text{red, onset}}$ values of PI-Fiber and $E_{1/2}$ value of ferrocene (0.09 V vs Ag/Ag⁺) at the same conditions.

Onset potentials were acquired by estimating the intersection between the base line and tangent at the highest of the slope ($E_{\text{oxi, onset}} = 0.89 \text{ V vs Ag/Ag}^+$, $E_{\text{red, onset}} = -0.72 \text{ V vs Ag/Ag}^+$). HOMO and LUMO levels vs vacuum were calculated by following equations³⁵;

$$E_{\text{LUMO}}(\text{eV}) = -[E_{\text{red, onset}} - E_{1/2}(\text{ferrocene}) + 4.8]$$

$$E_{\text{HOMO}}(\text{eV}) = -[E_{\text{oxi, onset}} - E_{1/2}(\text{ferrocene}) + 4.8]$$

The current densities (I) were calculated by dividing current (i) into the loaded mass of active materials (m_a);

$$I (\text{A g}^{-1}) = \frac{i}{m_a}$$

The charge capacities from cyclic voltammetry curves were calculated by integrating CV curves (A) and using the following equation, where ν indicates scan rate;

$$Q (\text{C g}^{-1}) = \frac{A}{2m_a\nu}$$

The charge capacities from galvanostatic charge and discharge experiments were calculated by multiplying the applied current density, $I (\text{A g}^{-1})$, with discharging time, t (s),

$$Q (\text{C g}^{-1}) = I \times t$$

Specific energy densities (E) and power densities (P) from two electrode charge-discharge experiments were calculated from the following equations,

$$E = I \int_0^t V dt, \quad P = \frac{E}{t}$$

Coulombic efficiencies were calculated by dividing discharging time by charging time from galvanostatic experiments.

4.8. References

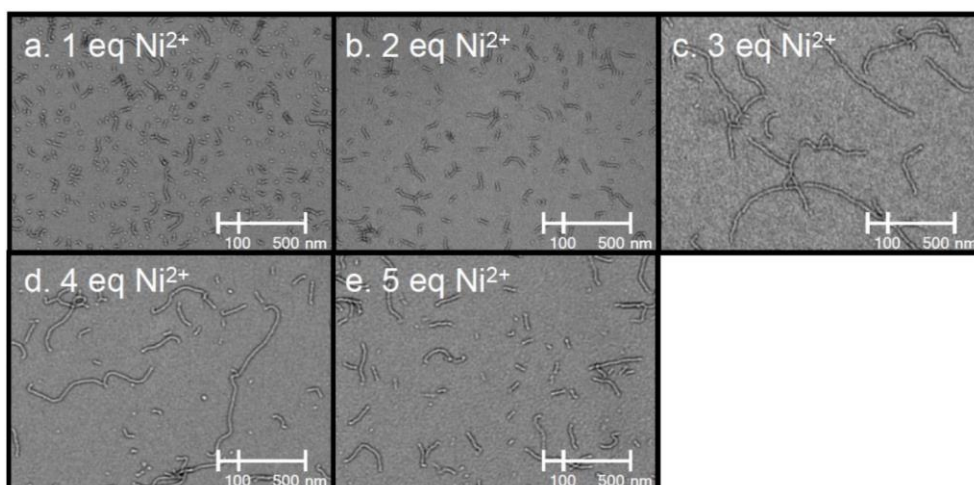
1. J. L. Segura, R. Juarez, M. Ramos and C. Seoane, *Chem. Soc. Rev.* 2015, **44**, 6850.
2. X.Y. Yan, M.D. Lin, S.T. Zheng, T.G. Zhan, X. Zhang, K.D. Zhang and X. Zhao, *Tetrahedron Lett.* 2018, **59**, 592.
3. M. Martinez-Abadia, C. T. Stoppiello, K. Strutynski, B. Lerma-Berlanga, C. Marti-Gastaldo, A. Saeki, M. Melle-Franco, A. N. Khlobystov and A. Mateo-Alonso, *J. Am. Chem. Soc.* 2019, **141**, 14403.
4. S. R. Peurifoy, J. C. Russell, T. J. Sisto, Y. Yang, X. Roy and C. Nuckolls, *J. Am. Chem. Soc.* 2018, **140**, 10960.
5. M. Ball, Y. Zhong, Y. Wu, C. Schenck, F. Ng, M. Steigerwald, S. Xiao and C. Nuckolls, *Acc. Chem. Res.* 2015, **48**, 267.
6. C. Russell, V. A. Posey, J. Gray, R. May, D. A. Reed, H. Zhang, L. E. Marbella, M. L. Steigerwald, Y. Yang, X. Roy, C. Nuckolls and S. R. Peurifoy, *Nat. Mater.* 2021, **20**, 1136.
7. G. Deng, J. Luo, S. Liu, Y. Wang, X. Zong, Q. Wu and S. Xue, *Sep. Purif. Technol.* 2020, **248**, 117088.
8. Y. Zhang, Z. Huang, B. Ruan, X. Zhang, T. Jiang, N. Ma and F. C. Tsai, *Macromol. Rapid. Commun.* 2020, **41**, e2000402.
9. Q. Fang, Z. Zhuang, S. Gu, R. B. Kaspar, J. Zheng, J. Wang, S. Qiu and Y. Yan, *Nat. Commun.* 2014, **5**, 4503.
10. K. Liu, H. Qi, R. Dong, R. Shivhare, M. Addicoat, T. Zhang, H. Sahabudeen, T. Heine, S. Mannsfeld, U. Kaiser, Z. Zheng and X. Feng, *Nat. Chem.* 2019, **11**, 994.
11. H. Duan, P. Lyu, J. Liu, Y. Zhao and Y. Xu, *ACS Nano* 2019, **13**, 2473.
12. K. V. Kumar, S. Gadipelli, B. Wood, K. A. Ramisetty, A. A. Stewart, C. A. Howard, D. J. L. Brett and F. Rodriguez-Reinoso, *J. Mater. Chem. A* 2019, **7**, 10104.
13. X. Li, Q. Gao, J. Aneesh, H.-S. Xu, Z. Chen, W. Tang, C. Liu, X. Shi, K. V. Adarsh, Y. Lu and K. P. Loh, *Chem. Mater.* 2018, **30**, 5743.

14. R. Wang, Q. Cai, Y. Zhu, Z. Mi, W. Weng, Y. Liu, J. Wan, J. Hu, C. Wang, D. Yang and J. Guo, *Chem. Mater.* 2021, **33**, 3566.
15. T. Aoki, H. Sakai, K. Ohkubo, T. Sakanoue, T. Takenobu, S. Fukuzumi and T. Hasobe, *Chem. Sci.* 2015, **6**, 1498.
16. S. Wang, Q. Wang, P. Shao, Y. Han, X. Gao, L. Ma, S. Yuan, X. Ma, J. Zhou, X. Feng and B. Wang, *J. Am. Chem. Soc.* 2017, **139**, 4258.
17. Y. Yusran, H. Li, X. Guan, D. Li, L. Tang, M. Xue, Z. Zhuang, Y. Yan, V. Valtchev, S. Qiu and Q. Fang, *Adv. Mater.* 2020, **32**, e1907289.
18. R. R. Kapraev, I. S. Zhidkov, E. Z. Kurmaev, K. J. Stevenson and P. A. Troshin, *J. Mater. Chem. A* 2019, **7**, 22596.
19. T. S. Mathis, N. Kurra, X. Wang, D. Pinto, P. Simon and Y. Gogotsi, *Adv. Energy Mater.* 2019, **9**, 1902007.
20. Z. Yang, J. Liu, Y. Li, G. Zhang, G. Xing, and L. Chen, *Angew. Chem. Int. Ed.* 2021, **60**, 20754.
21. Y. Yang, P. Zhang, L. Hao, P. Cheng, Y. Chen, and Z. Zhang, *Angew. Chem.* 2021, **133**, 2.
22. M. Li, J. Liu, Y. Li, G. Xing, X. Yu, C. Peng, and L. Chen, *CCS Chem.* 2021, **3**, 696.
23. A. F. M. El-Mahdy, Y. H. Hung, T. H. Mansoure, H. H. Yu, T. Chen, and S. W. Kuo, *Chem. Asian. J.* 2019, **14**, 1429.
24. S. R. Peurifoy, J. C. Russell, T. J. Sisto, Y. Yang, X. Roy, and C. Nuckolls, *J. Am. Chem. Soc.* 2018, **140**, 10960.
25. S. Chandra, D. Roy Chowdhury, M. Addicoat, T. Heine, A. Paul, and R. Banerjee, *Chem. Mater.* 2017, **29**, 2074.
26. P. Bhanja, S. K. Das, K. Bhunia, D. Pradhan, T. Hayashi, Y. Hijikata, S. Irle, and A. Bhaumik, *ACS Sustainable Chem. Eng.* 2017, **6**, 202.
27. P. Bhanja, K. Bhunia, S. K. Das, D. Pradhan, R. Kimura, Y. Hijikata, S. Irle, and A. Bhaumik, *ChemSusChem* 2017, **10**, 921.
28. C. R. DeBlase, K. E. Silberstein, T. T. Truong, H. D. Abruna, and, W. R. Dichtel, *J. Am. Chem. Soc.* 2013, **135**, 16821.

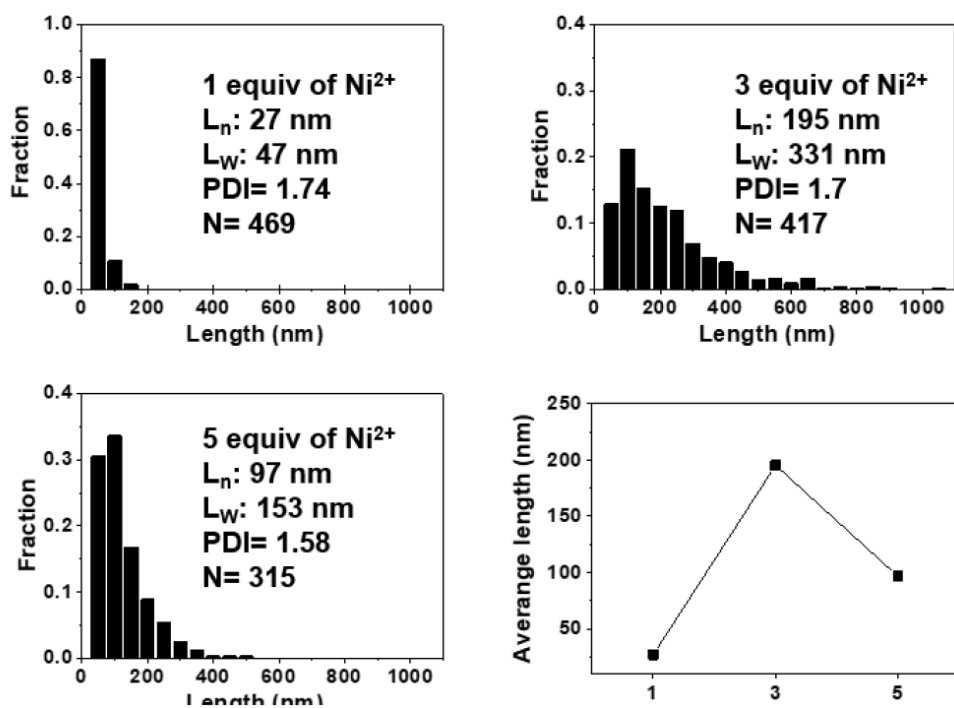
29. S. Vargheese, R. T. R. Kumar, and Y. Haldorai, *Mater. Lett.* 2019, **249**, 53.
30. R. Xue, Y.P. Zheng, D.Q. Qian, D.Y. Xu, Y.S. Liu, S.L. Huang, G.Y. Yang, *Mater. Lett.* 2021, **308**, 131229.
31. R. Vinodh, C. V. V. Muralee Gopi, Z. Yang, C. Deviprasath, R. Atchudan, V. Raman, M. Yi, and H. J. Kim, *J. Energy Storage* 2020, **28**, 101283.
32. Y. Zhang, L. Cheng, L. Zhang, D. Yang, C. Du, L. Wan, J. Chen, and M. Xie, *J. Energy Storage* 2021, **34**, 101786.
33. X. Kong, S. Zhou, M. Strømme, and C. Xu, *Carbon* 2021, **171**, 248.
34. A. Roy, S. Mondal, A. Halder, A. Banerjee, D. Ghoshal, A. Paul, and S. Malik, *Eur. Polym. J.* 2017, **93**, 448.
35. Y. Zhang, B. Zhang, L. Chen, T. Wang, M. Di, F. Jiang, X. Xu, and S. Qiao, *J. Colloid. Interface. Sci.* 2022, **606**, 1534.
36. J. Chen, C. Du, Y. Zhang, W. Wei, L. Wan, M. Xie, and Z. Tian, *Polymer* 2019, **162**, 43.
37. M. G. Mohamed, X. Zhang, T. H. Mansoure, A. F. M. El Mahdy, C. F. Huang, M. Danko, Z. Xin, S. W. Kuo, *Polymer* 2020, **205**, 122857.
38. S. K. Das, K. Bhunia, A. Mallick, A. Pradhan, D. Pradhan, and A. Bhaumik, *Microporous Mesoporous Mater.* 2018, **266**, 109.
39. Y. Gao, C. Zhi, P. Cui, K. A. I. Zhang, L.P. Lv, and, Y. Wang, *Chem. Eng. J.* 2020, **400**, 124071.
40. M. Sajjad, R. Tao, K. Kang, S. Luo, and L. Qiu, *ACS Appl. Energy Mater.* 2021, **4**, 828.
41. W. Liu, M. Ulaganathan, I. Abdelwahab, X. Luo, Z. Chen, S. J. Rong Tan, X. Wang, Y. Liu, D. Geng, Y. Bao, J. Chen, and K. P. Loh, *ACS Nano* 2018, **12**, 852.
42. Y. Liao, H. Wang, M. Zhu, and A. Thomas, *Adv. Mater.* 2018, **30**, e1705710.
43. S. Xiong, J. Liu, Y. Wang, X. Wang, J. Chu, R. Zhang, M. Gong, and B. Wu, *J. Appl. Polym. Sci.* 2021, **139**, e51510.
44. L. Hao, B. Luo, X. Li, M. Jin, Y. Fang, Z. Tang, Y. Jia, M. Liang, A. Thomas, J. Yang, and L. Zhi, *Energy Environ. Sci.* 2012, **5**, 9747.
45. S. Bandyopadhyay, C. Singh, P. Jash, M. D. W. Hussain, A. Paul, and A. Patra,

- Chem. Commun.* 2018, **54**, 6796.
46. L. Xu, R. Liu, F. Wang, S. Yan, X. Shi, and J. Yang, *RSC Adv.* 2019, **9**, 1586.
47. A. F. M. El-Mahdy, M. G. Mohamed, T. H. Mansoure, H.-H. Yu, T. Chen, and S.-W. Kuo, *Chem. Commun.* 2019, **55**, 14890.
48. M. G. Mohamed, A. F. M. El-Mahdy, Y. Takashi, and S.-W. Kuo, *New J. Chem.* 2020, **44**, 8241.
49. B. Luo, Y. Chen, Y. Zhang, and J. Huo, *New J. Chem.* 2021, **45**, 17278.
50. N. An, Z. Guo, J. Xin, Y. He, K. Xie, D. Sun, X. Dong, and Z. Hu, *J. Mater. Chem. A* 2021, **9**, 16824.
51. X.-C. Li, Y. Zhang, C.-Y. Wang, Y. Wan, W.-Y. Lai, H. Pang, and W. Huang, *Chem. Sci.* 2017, **8**, 2959.
52. L. Li, F. Lu, R. Xue, B. Ma, Q. Li, N. Wu, H. Liu, W. Yao, H. Guo, and W. Yang, *ACS Appl. Mater. Interfaces* 2019, **11**, 26355.
53. B. E. Conway and E. Gilea, *Trans. Faraday Soc.* 1962, **58**, 2493.
54. K. Kanakarajan and A. W. Czarnik, *J. Org. Chem.* 1986, **51**, 5241.
55. T. Aoki, H. Sakai, K. Ohkubo, T. Sakanoue, T. Takenobu, S. Fukuzumi, and T. Hasobe, *Chem. Sci.* 2015, **6**, 1498.
56. A. J. Fatiadi and W. F. Sager, *Org. Synth.* 1962, **42**, 90.
57. J. T. Rademacher, K. Kanakarajan, and A. W. Czarnik, *Synthesis* 1994, **4**, 378.

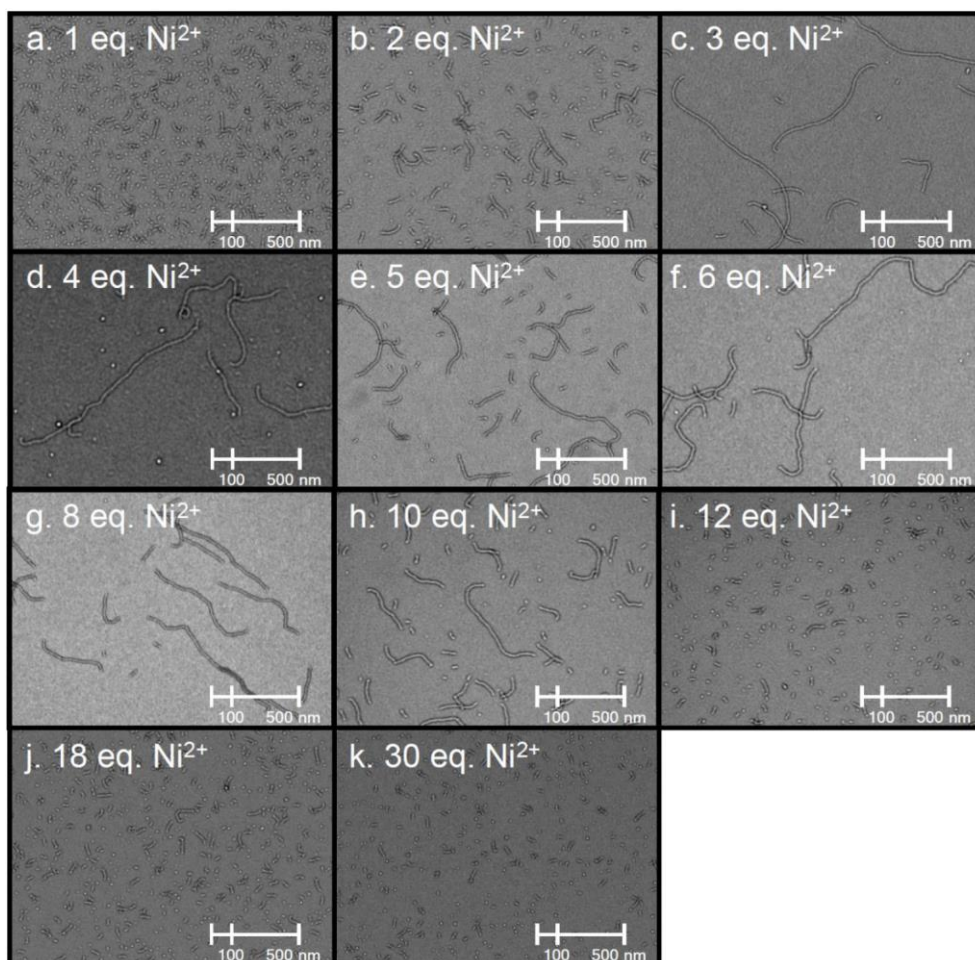
Appendix



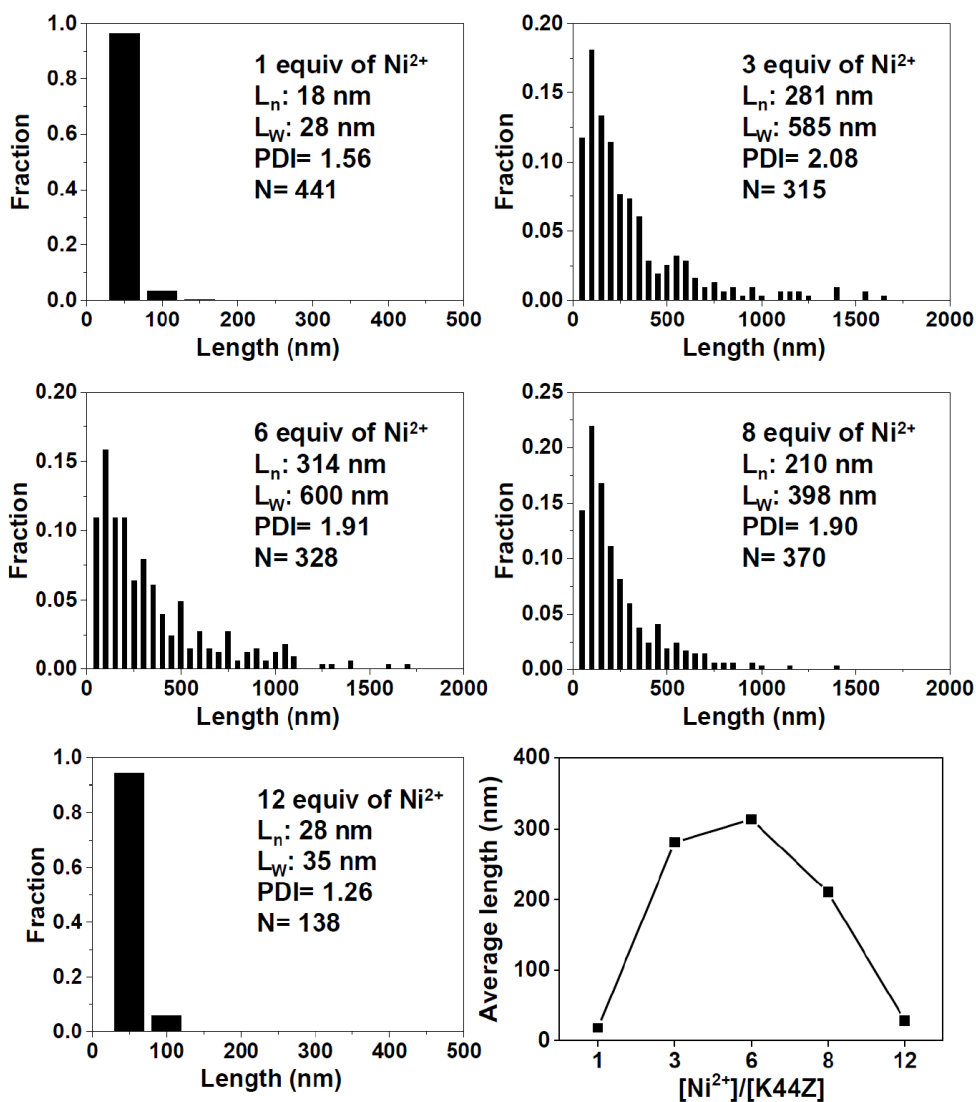
Appendix 2.1. (1) K44Z (10 μ M) with various ratios of Ni^{2+} at 4 $^{\circ}\text{C}$ for 24 h.



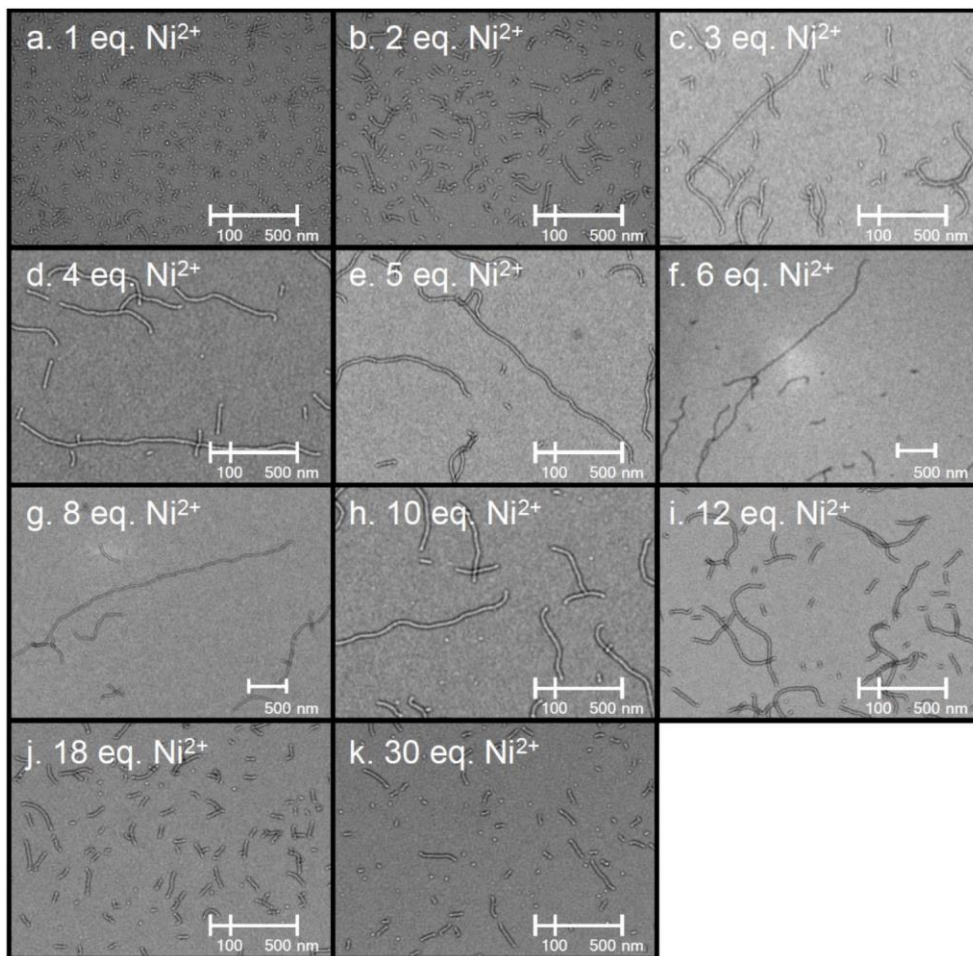
Appendix 2.1. (2) Distributions of the 1D-rods in (a) and the number average length (L_n) of the rods as a function of Ni^{2+} to protein ratio. The L_n , L_w , PDI, and N values indicate number average length, weight average length, polydispersity index, and the number of counted 1D-assembled rods, respectively.



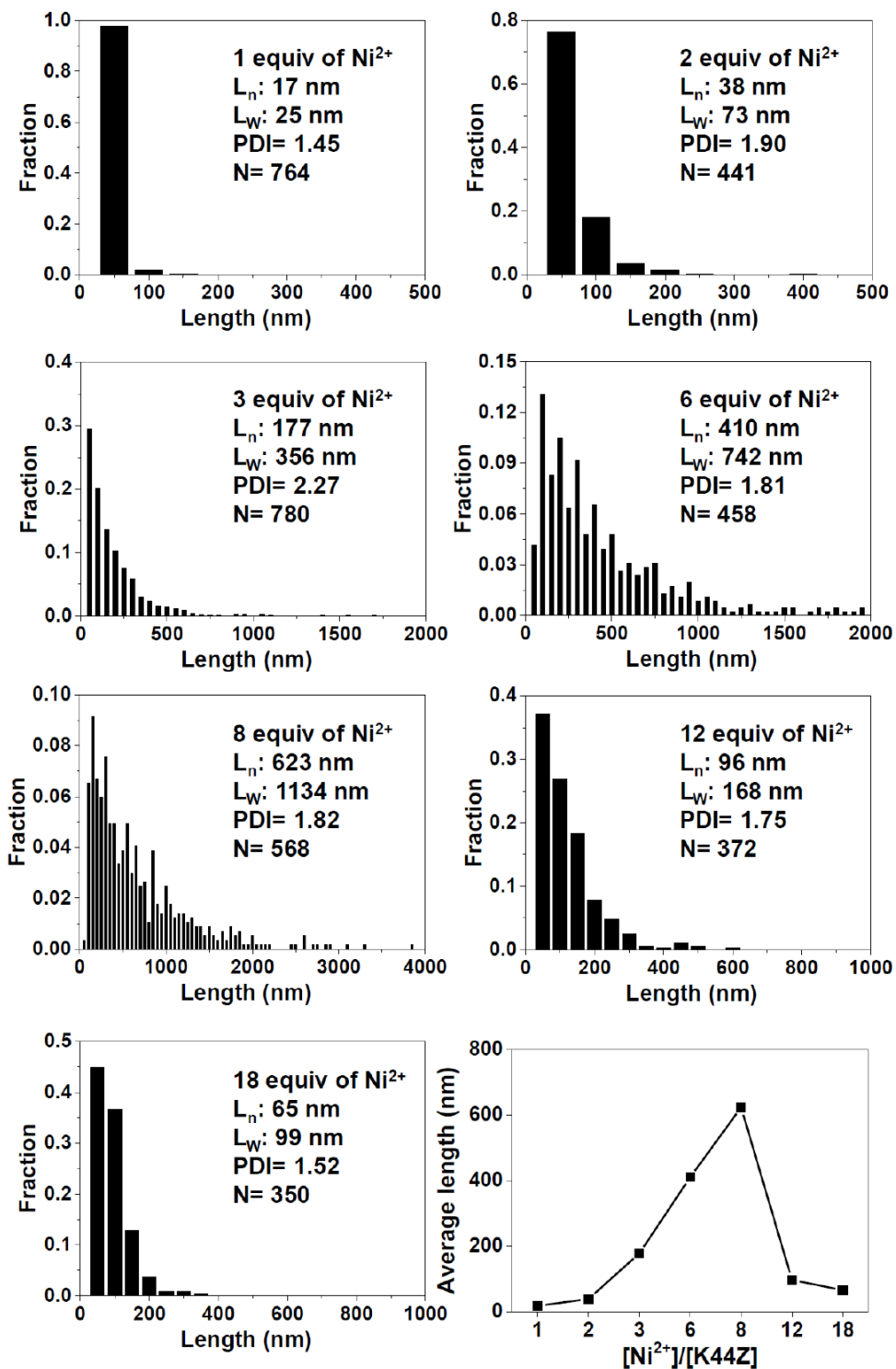
Appendix 2.2. (1) TEM images of 1D-rods formed with K44Z protein (10 μM) and (a) 1 (b) 2 (c) 3 (d) 4 (e) 5 (f) 6 (g) 8 (h) 10 (i) 12 (j) 18 (k) 30 equiv of Ni²⁺ at 22 °C. The longest rod-shaped materials were observed when 3–6 equiv of Ni²⁺ to 1 equiv of protein was added.



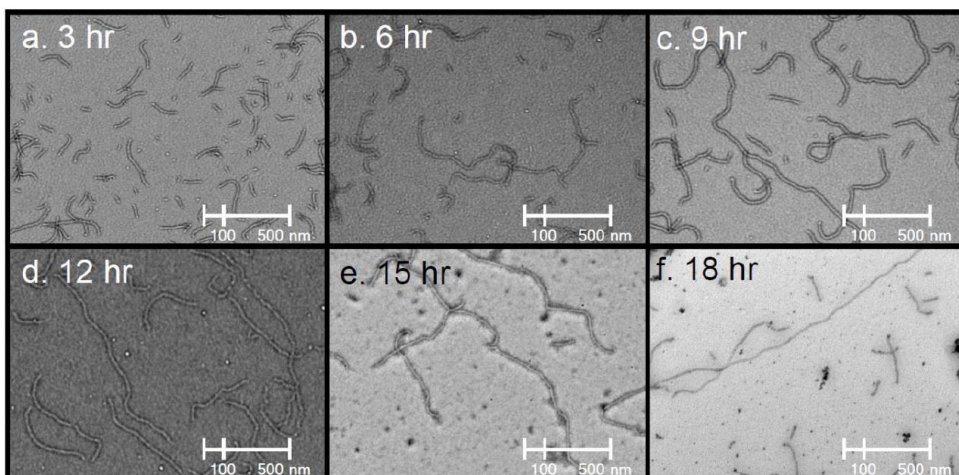
Appendix 2.2. (2) Distributions of 1D rods shown in Appendix 2.2 (1) and the average length (L_n) of the rods as a function of Ni^{2+} to protein ratio. The optimal ratio of metal to protein was determined to be 3–6 equiv at 22 °C.



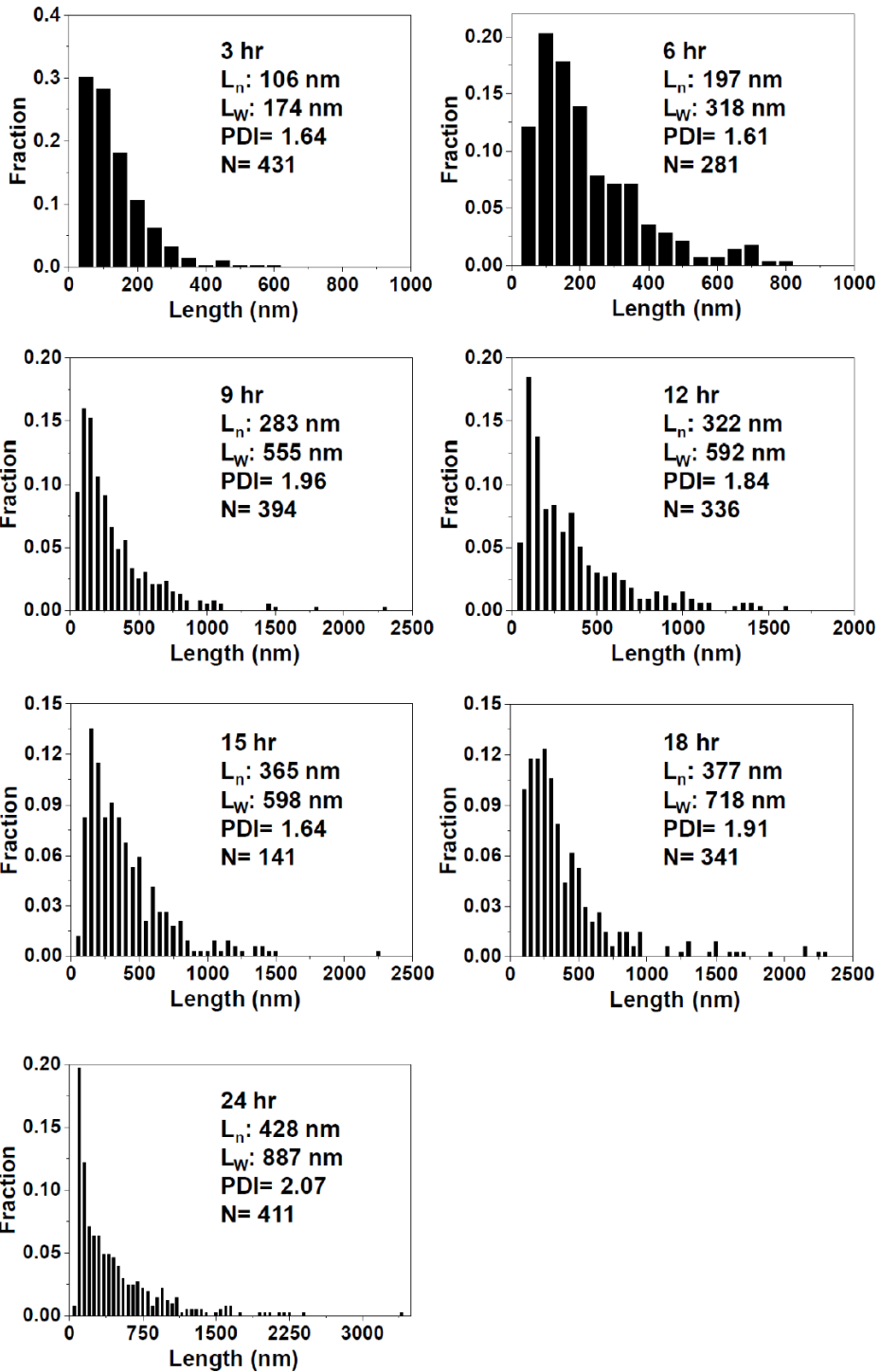
Appendix 2.3. (1) TEM images of 1D rods formed upon the addition of various concentrations of Ni^{2+} to K44Z protein ($10 \mu\text{M}$) at 37°C . (a) 1 (b) 2 (c) 3 (d) 4 (e) 5 (f) 6 (g) 8 (h) 10 (i) 12 (j) 18 (k) 30 equiv of Ni^{2+} . The optimized ratio of metal to protein was determined to be 8 equiv of Ni^{2+} at 37°C , higher than the values observed at lower temperatures.



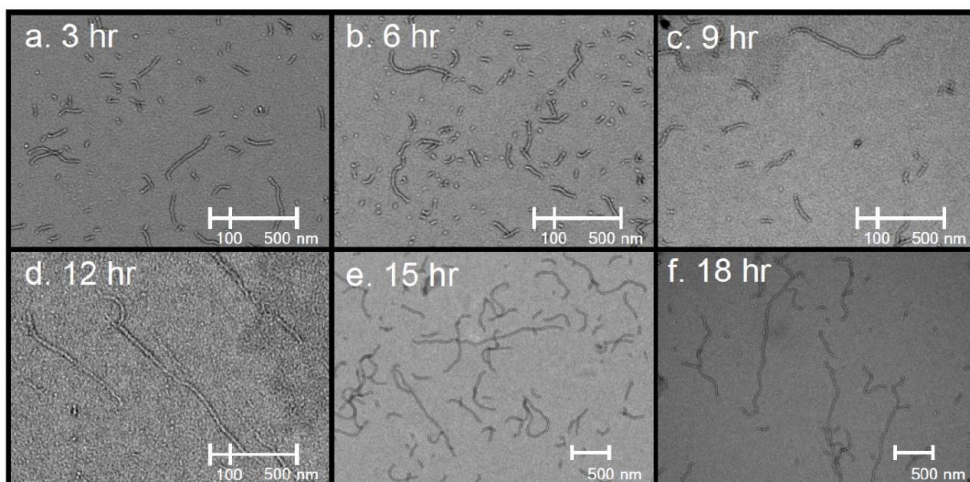
Appendix 2.3. (2) Distributions of K44Z (10 μ M) 1D-rods assembled at 37 $^{\circ}$ C and the average length (L_n) of the rods as a function of Ni²⁺ to protein ratio. The optimal ratio of metal to protein is 8 at 37 $^{\circ}$ C.



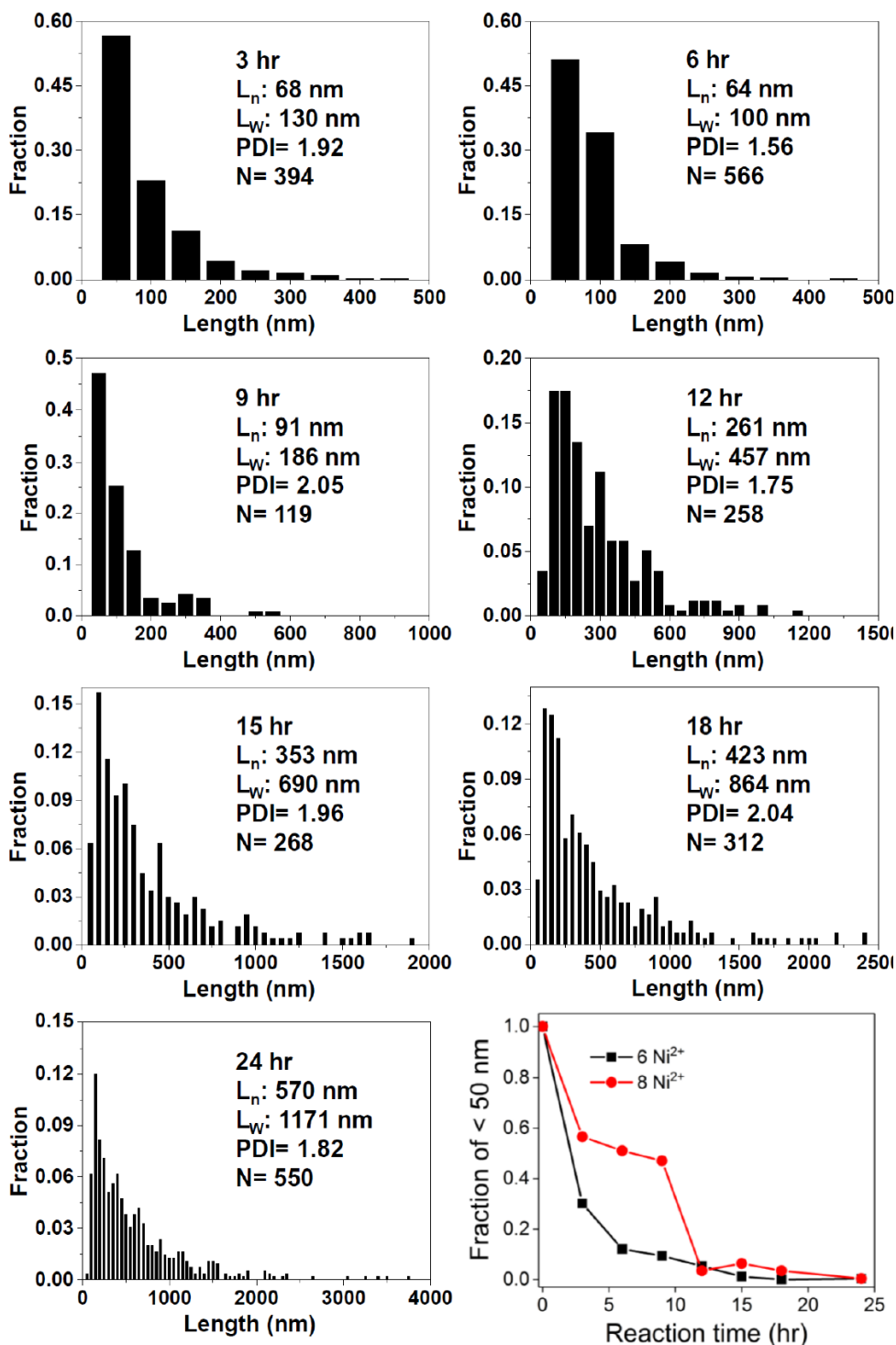
Appendix 2.4. (1) Formation kinetics of 1D rod formation with K44Z protein with 6 equiv Ni^{2+} . TEM images were acquired after the incubation of K44Z ($5 \mu\text{M}$) with 6 equiv Ni^{2+} at $37 \text{ }^\circ\text{C}$ for (a) 3 h (b) 6 h (c) 9 h (d) 12 h (e) 15 h (f) 18 h. Protein rods with various lengths were observed, implying that 1D assembly of K44Z proceeds via step-growth polymerization mechanism.



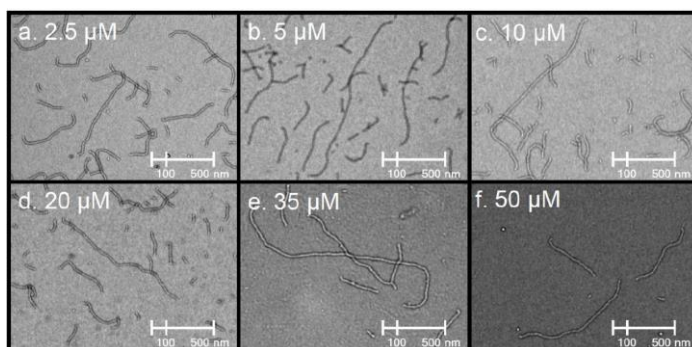
Appendix 2.4. (2) Time-dependent length changes determined from the TEM images in Appendix 2.4. (1).



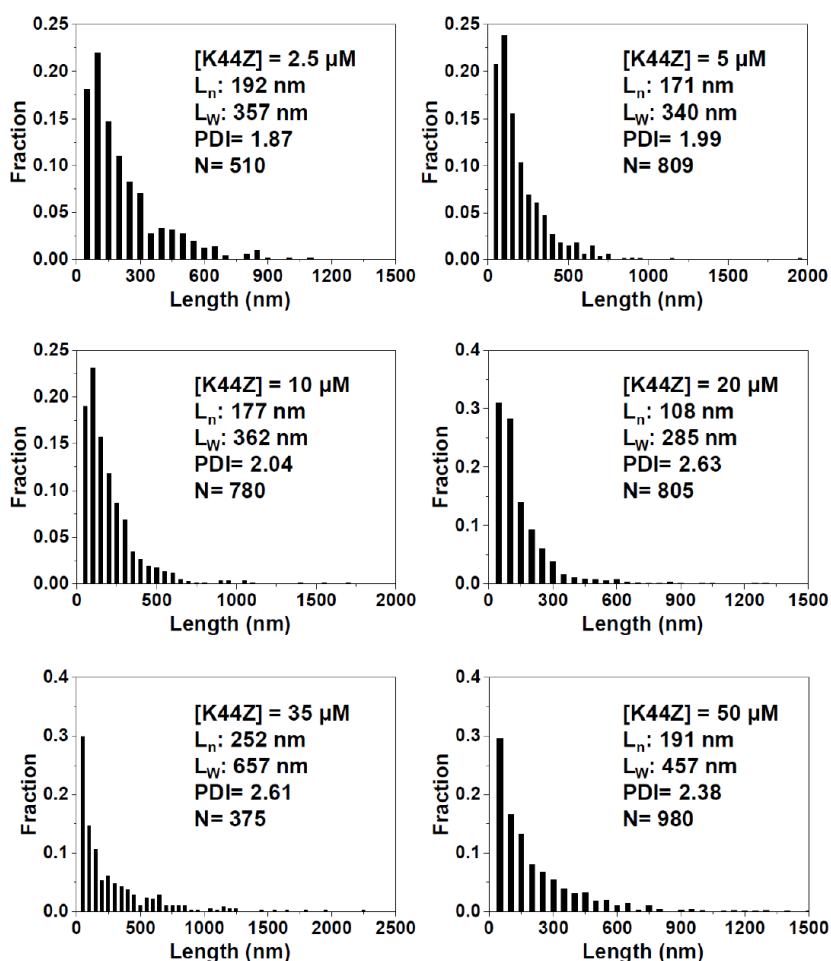
Appendix 2.5. (1) Formation kinetics of 1D rod formation with K44Z protein with 8 equiv. Ni^{2+} . TEM images were acquired after the incubation of K44Z (5 μM) with 8 equiv Ni^{2+} at 37 $^{\circ}\text{C}$ for (a) 3 h (b) 6 h (c) 9 h (d) 12 h (e) 15 h (f) 18 h. Similar to the data in Appendix 2.4, the protein rods with various lengths were observed, indicating that the step-growth polymerization mechanism is operative.



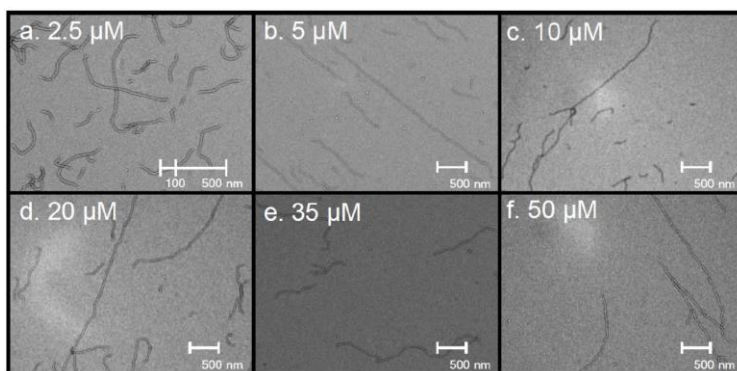
Appendix 2.5. (2) Time-dependent distributions of 1D-rods shown in Appendix 2.5. (1) and the average length (L_n) as a function of reaction time.



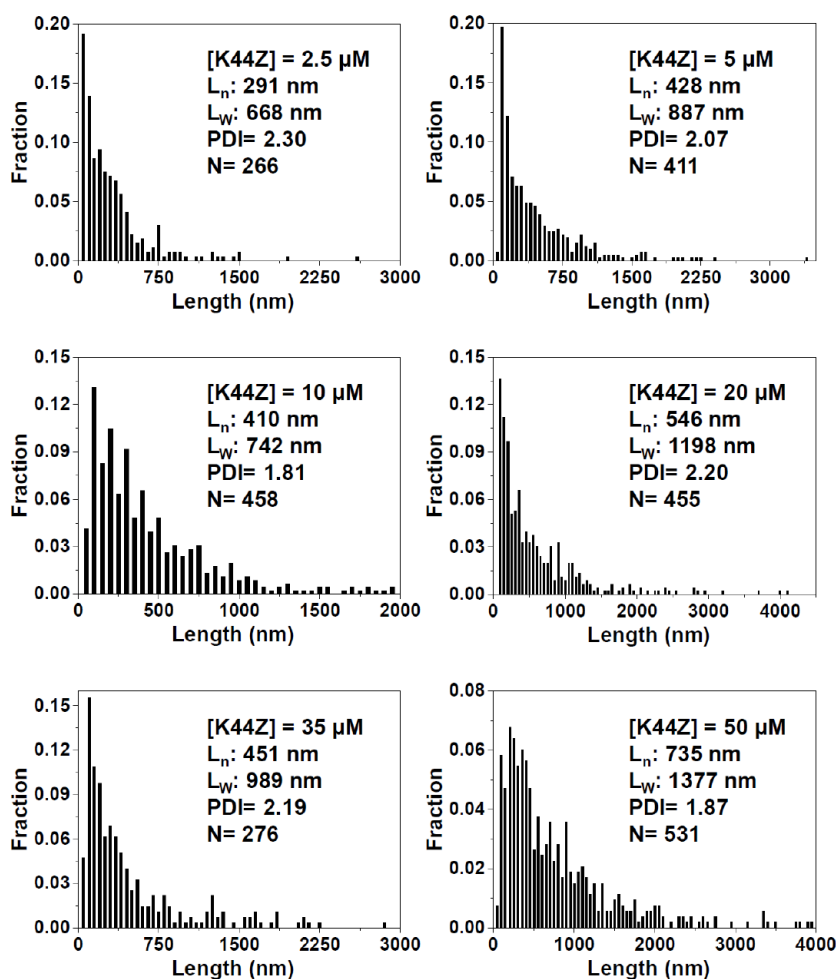
Appendix 2.6. (1) TEM images of the 1D rods with various concentrations of K44Z proteins with 3 equiv Ni^{2+} at 37 °C. (a) 2.5 μM (b) 5 μM (c) 10 μM (d) 20 μM (e) 35 μM (f) 50 μM of K44Z protein. No considerable difference in the length of the protein rods was observed upon the variations of the protein concentrations.



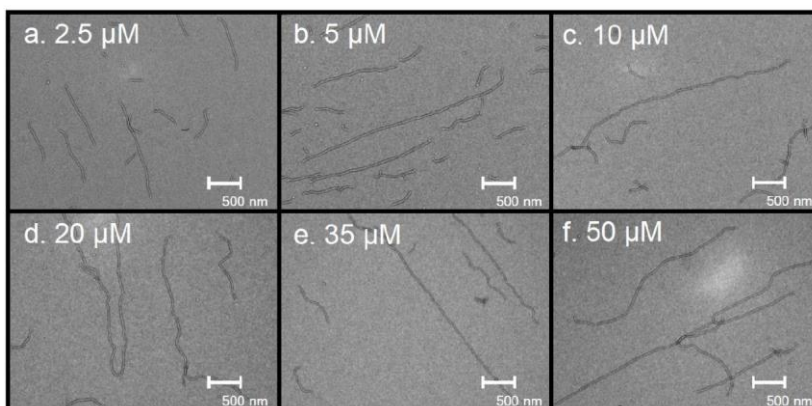
Appendix 2.6. (2) Distributions of K44Z-derived 1D-rods with various concentrations of K44Z (2.5–50 μM) and 3 equiv of Ni^{2+} at 37 °C for 24 h.



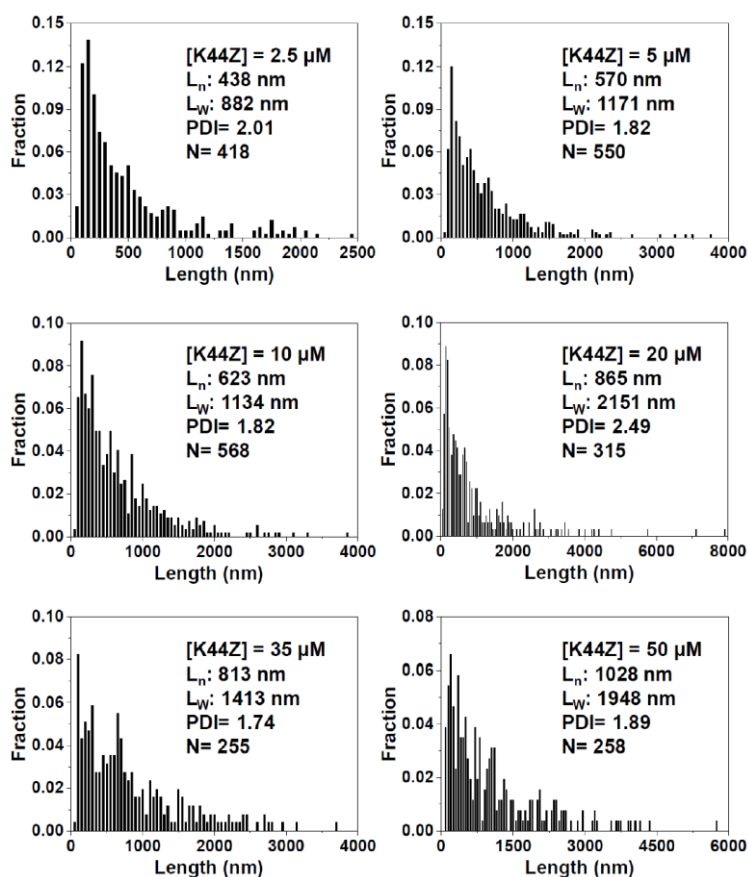
Appendix 2.7. (1) TEM images of the 1D rods formed with the various concentrations of K44Z protein and 6 equiv of Ni^{2+} at 37 °C for 24 h. (a) 2.5 μM (b) 5 μM (c) 10 μM (d) 20 μM (e) 35 μM (f) 50 μM of K44Z.



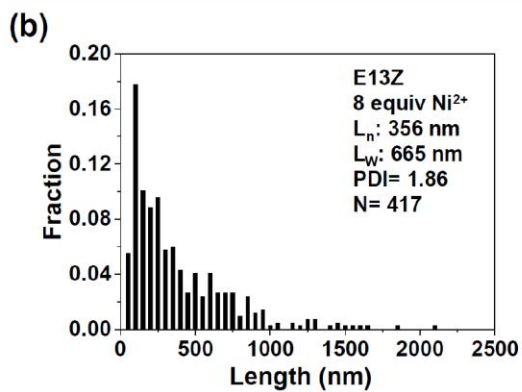
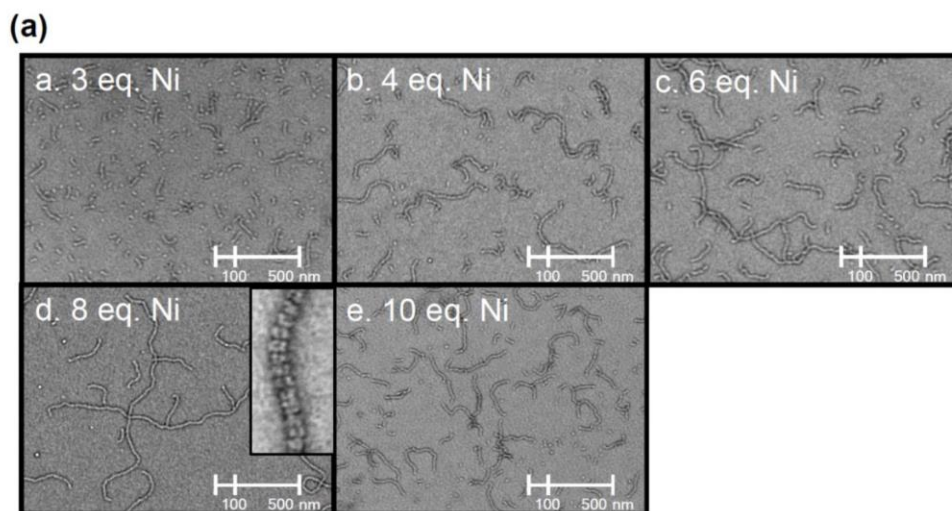
Appendix 2.7. (2) Distributions of the 1D-rods formed with K44Z (2.5–50 μM) and 6 equiv. (the less than optimal) of Ni^{2+} at 37 °C.



Appendix 2.8. (1) TEM images of the 1D rods formed with the various concentrations of K44Z protein and 8 equiv of Ni^{2+} at 37 °C for 24 h. (a) 2.5 μM (b) 5 μM (c) 10 μM (d) 20 μM (e) 35 μM (f) 50 μM of K44Z.

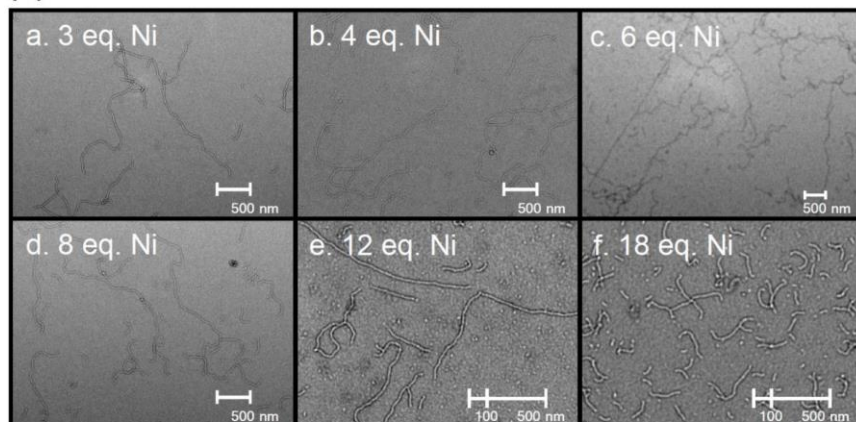


Appendix 2.8. (2) Distributions of the 1D-rods formed with K44Z (2.5–50 μM) and 8 equiv. (the less than optimal) of Ni^{2+} at 37 °C.

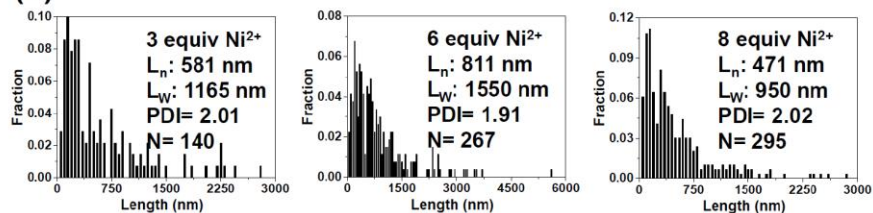


Appendix 2.9. Formation of 1D-rods with E13Z and Ni²⁺. (a) TEM images of 1D-rods from the reactions of E13Z (10 μM) and Ni²⁺ (3–10 equiv) at 37 °C. (b) Distribution of the number average length when the optimal ratio of Ni²⁺ to protein was applied as 8.

(a)

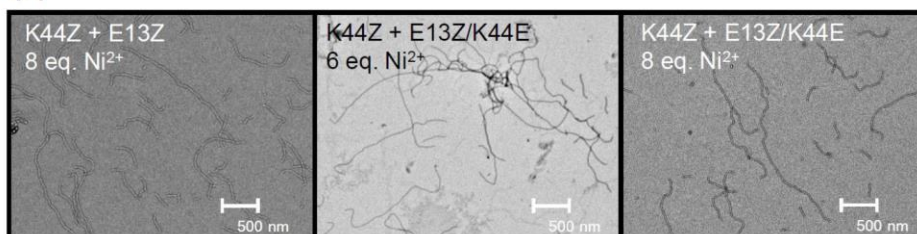


(b)

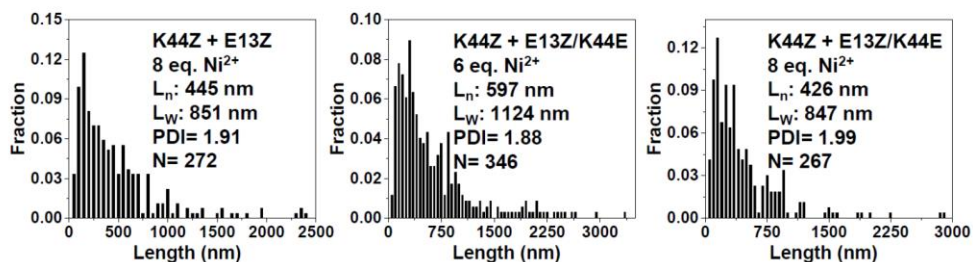


Appendix 2.10. Formation of 1D-rods with E13Z/K44E and Ni²⁺. (a) TEM images. (b) Distributions of the 1D-assembled structures from E13Z/K44E (10 μM) with Ni²⁺ (3–18 equiv.).

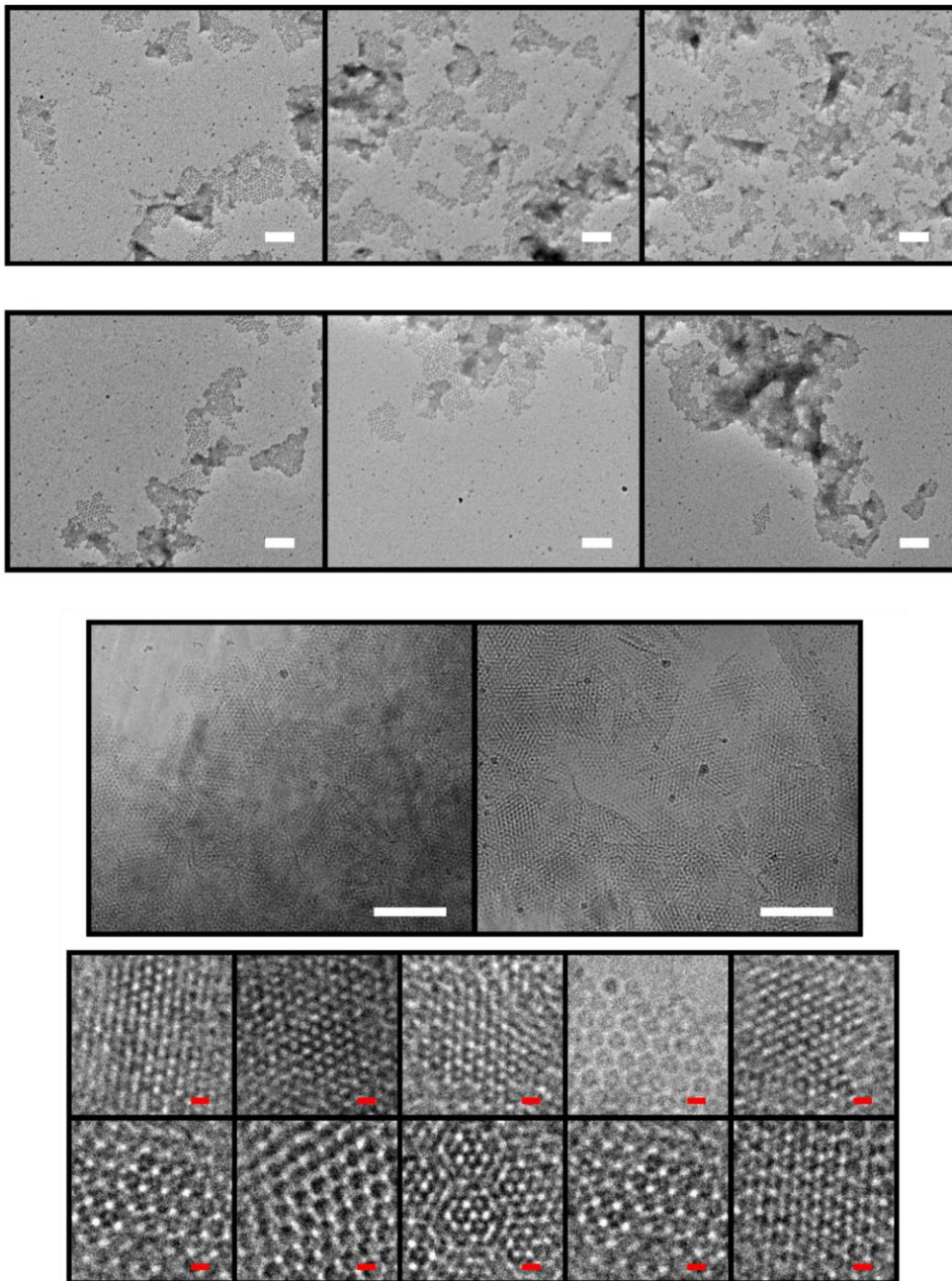
(a)



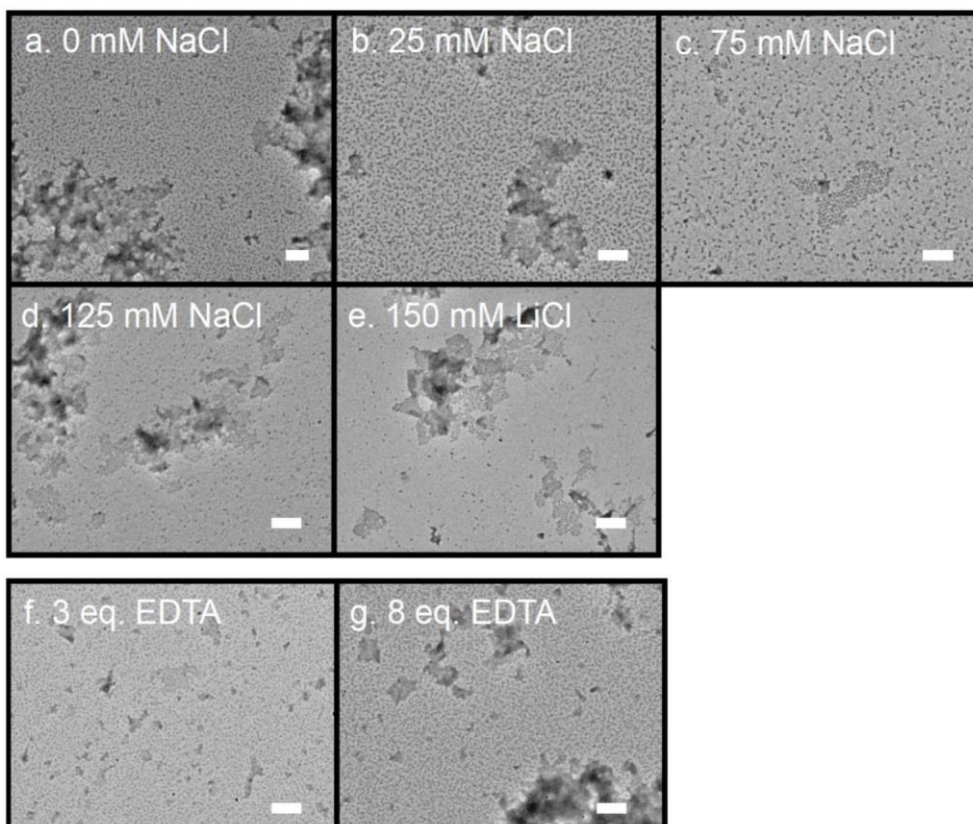
(b)



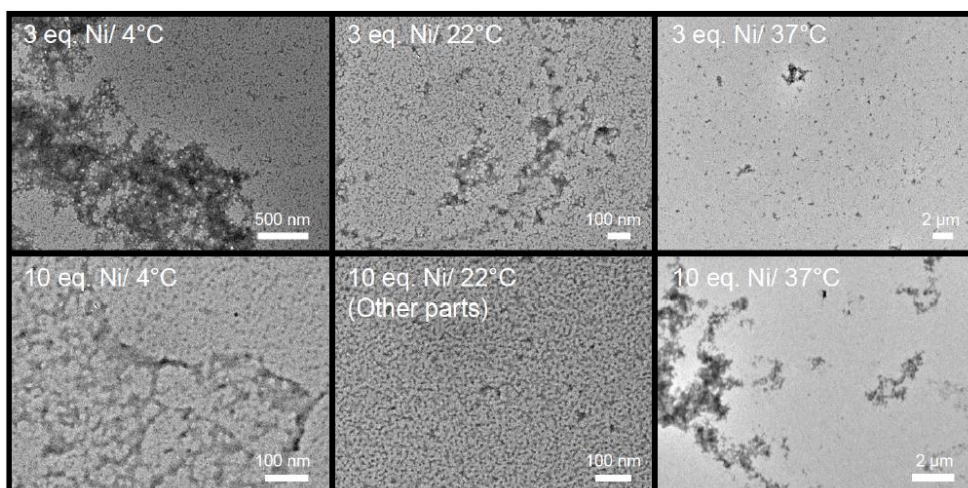
Appendix 2.11. Formation of 1D-assembled structures with two variants, K44Z and E13Z or E13Z/K44E. (a) TEM images. (b) Distributions from the data in (a). The equal ratio of each protein (10 μM at final concentration) was pre-mixed, followed by the addition of 6 or 8 equiv. Ni²⁺ at 37 °C for 24 h.



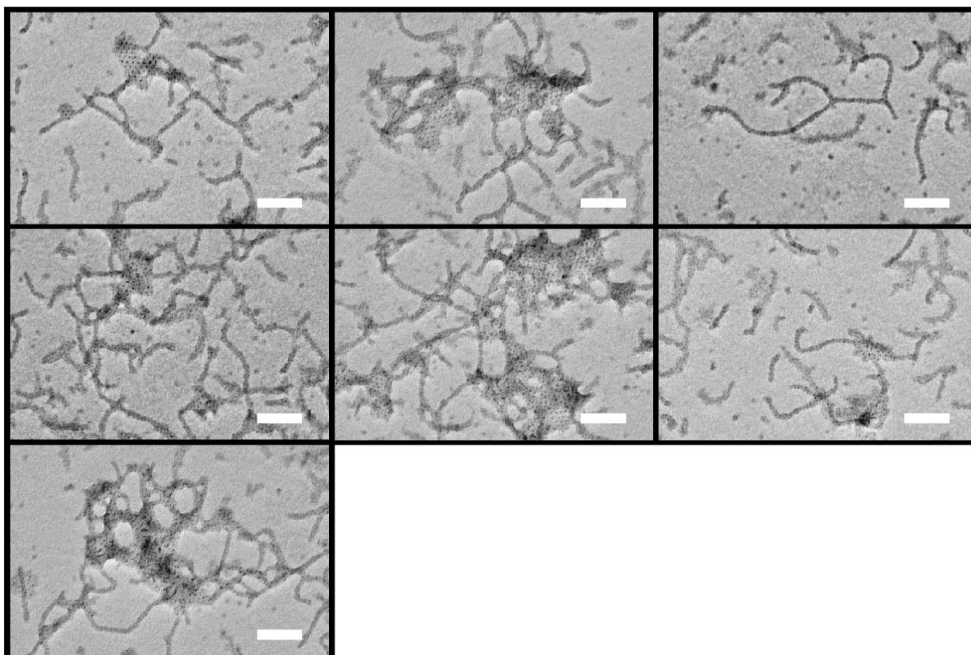
Appendix 2.12. (Top) 5 μM and 10 μM of K337Z protein and 6 equiv Ni²⁺ at 37 °C for 24 h (Scale bar: 100 nm). (Down) Cryo-TEM images of 2D-planes from the reactions of K337Z with 6 equiv Ni²⁺ at 37 °C for 24 h (Scale bar: 200 nm for white, 10 nm for red).



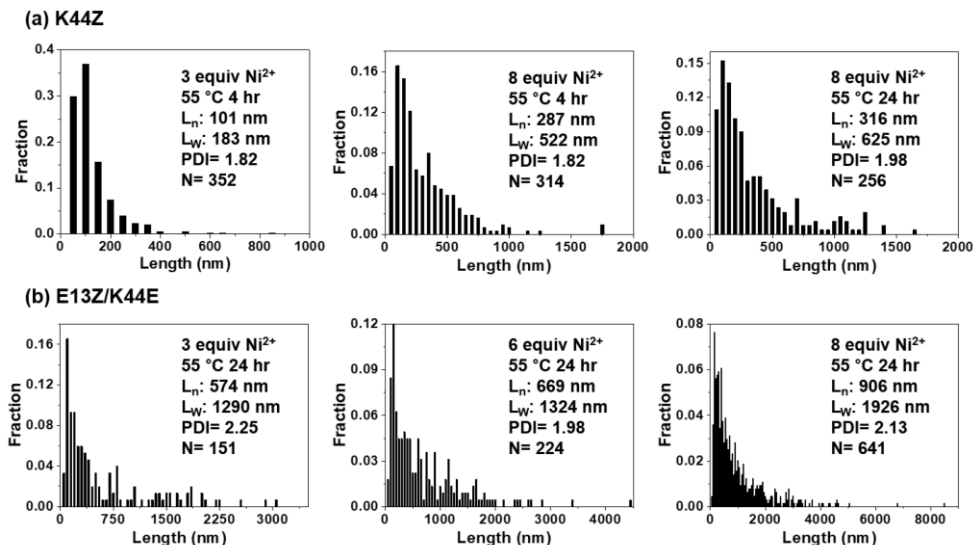
Appendix 2.13. TEM images of K337Z protein (10 μM) reacted with 6 equiv. of Ni²⁺ under various conditions. (a-d) [NaCl] = 0–125 mM NaCl (e) 150 mM LiCl (f-g) Destruction of pre-formed planes upon the addition of 3 or 8 equiv. of EDTA (Scale bar: 100 nm).



Appendix 2.14. TEM images of W298Z with Ni²⁺ under various conditions. Noncrystalline, heterogeneous materials were observed in the listed conditions.

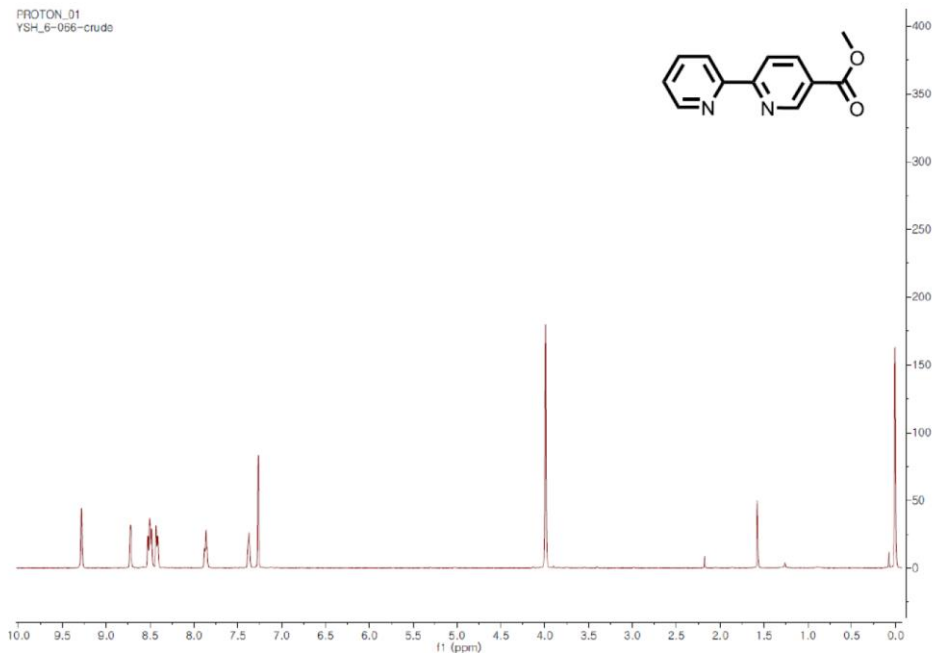


Appendix 2.15. TEM images of the hybrid structures with K44Z, K337Z, and Ni^{2+} . Relatively short nanorods were formed with K44Z ($10 \mu\text{M}$) with 3 equiv. of Ni^{2+} at 22°C for 4 h, followed by the addition of K337Z ($2 \mu\text{M}$) and 3 equiv. of Ni^{2+} 22°C for 20 h to yield desired structures. (Scale bar: 100 nm)



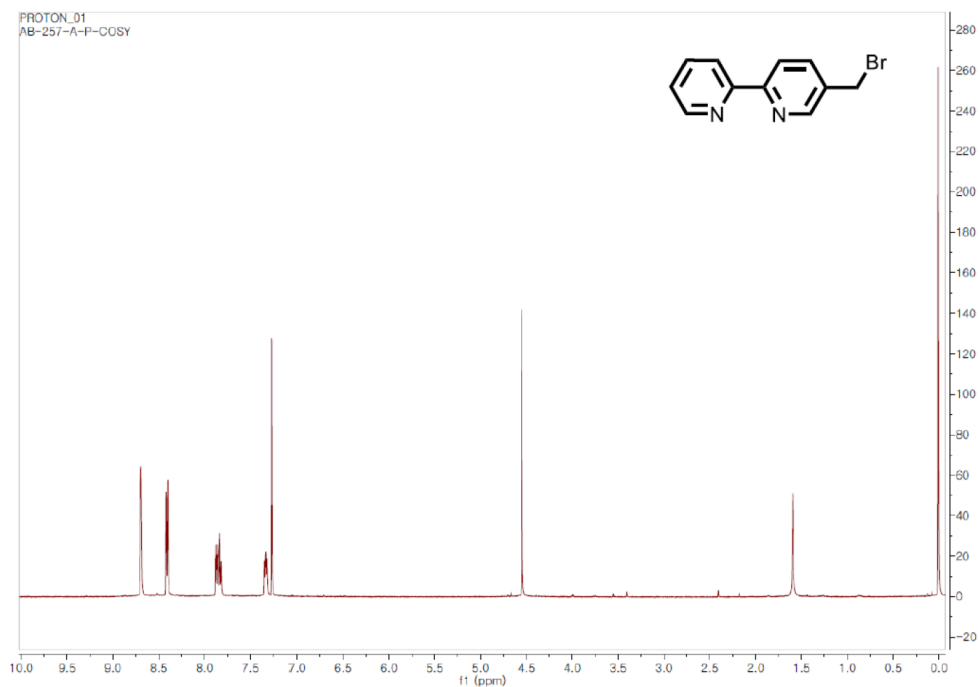
Appendix 2.16. Distributions of 1D-rods after heating at 55°C . The (a) K44Z or (b) K44E/E13Z with 3–8 equiv. of Ni^{2+} were incubated for 24 h at 37°C and further heated at 55°C for 4–24 h.

PROTON_01
YSH_6-066-crude

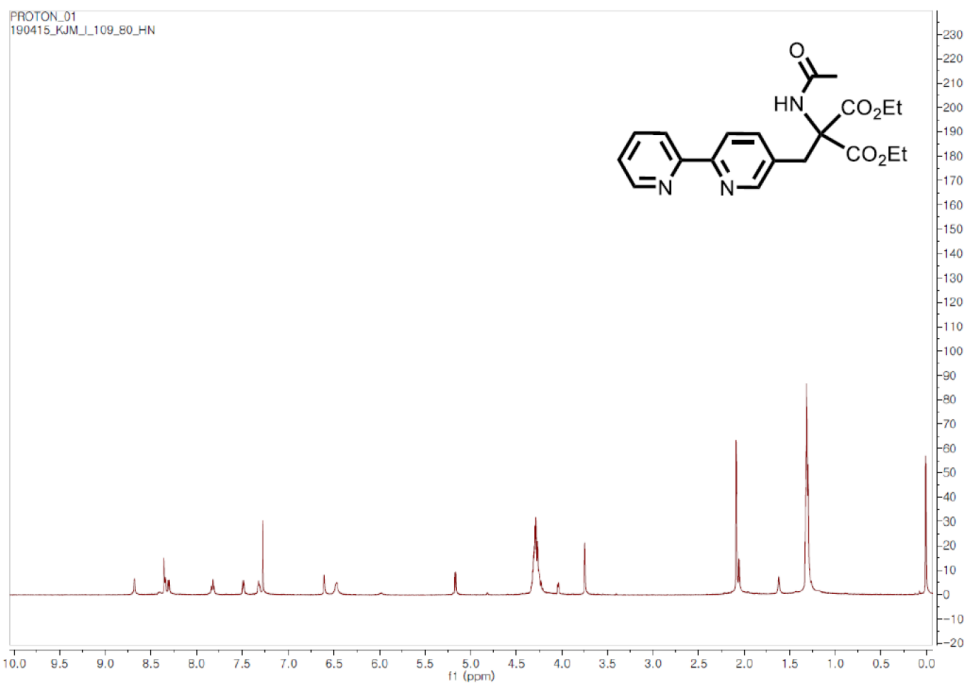


Appendix. 2.17. ¹H NMR spectrum of (2)

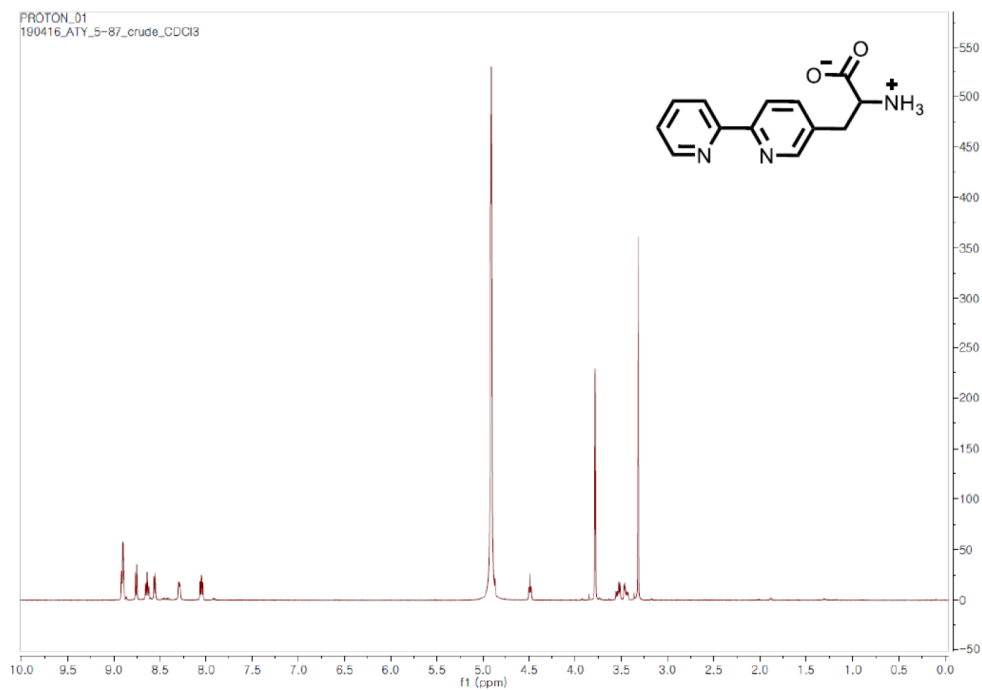
PROTON_01
AB-257-A-P-COSY



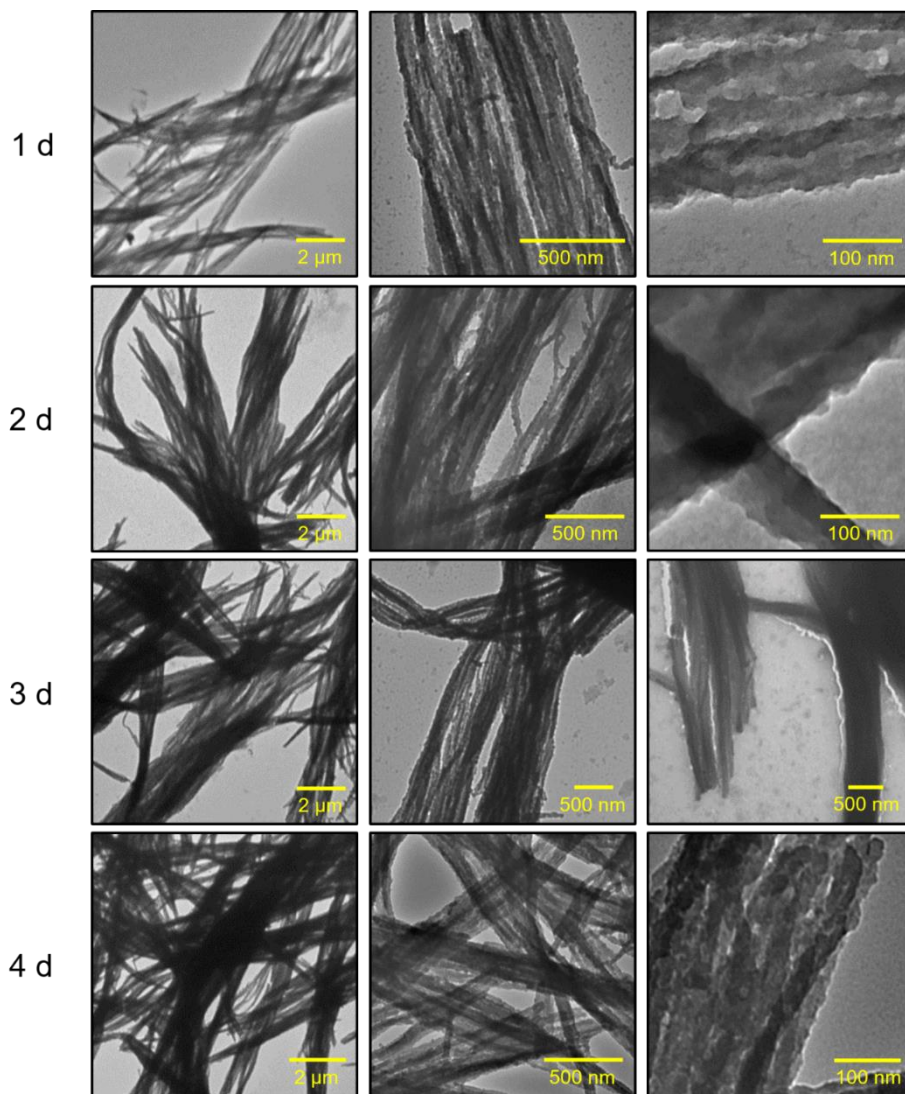
Appendix. 2.18. ¹H NMR spectrum of (4)



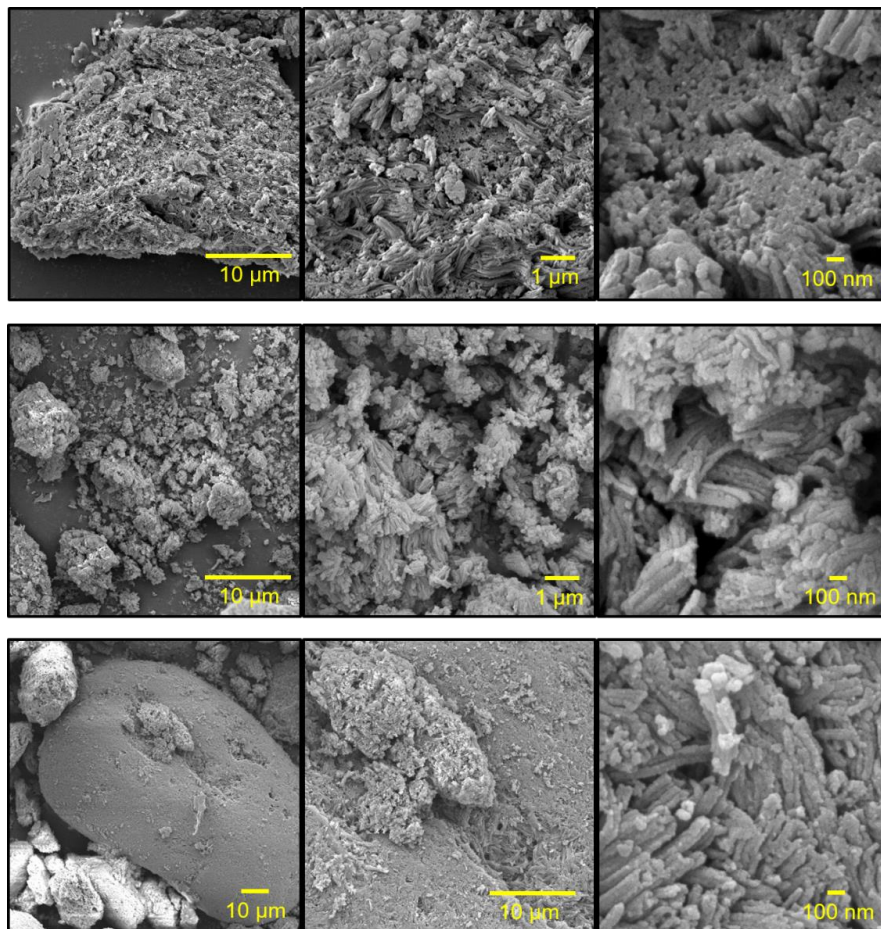
Appendix. 2.19. ^1H NMR spectrum of (5)



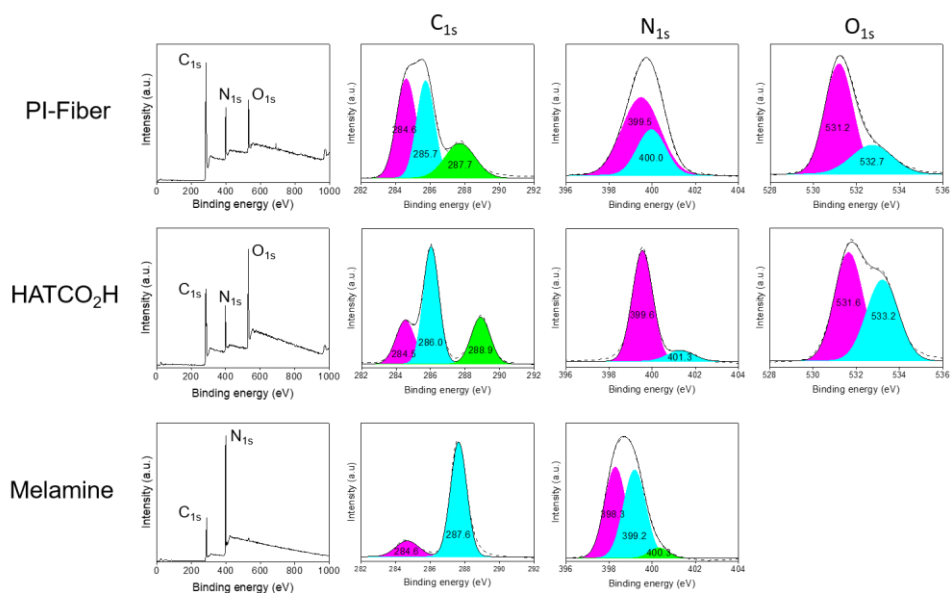
Appendix. 2.20. ^1H NMR spectrum of (6)



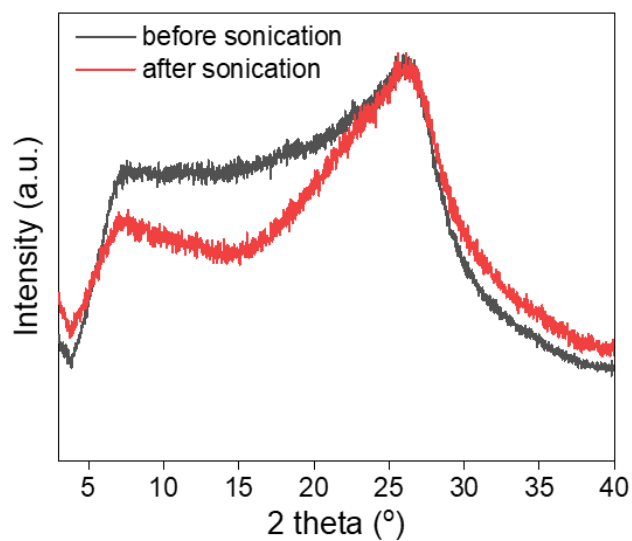
Appendix 4.1. Time-dependent TEM images of samples during imidization.



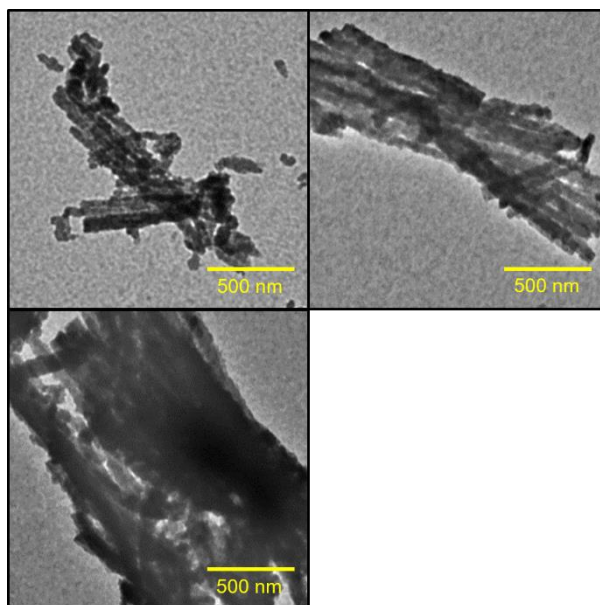
Appendix 4.2. SEM images of PI-Fiber. All images show fibril structures with some variations in overall morphology and size.



Appendix 4.3. XPS spectrum of PI-Fiber, HATCO₂H, and melamine. Full spectrum and high-resolution profile of C_{1s}, N_{1s}, and O_{1s} are represented.



Appendix 4.4. The PXRD patterns of PI-Fiber. The signals were slightly improved after sonication.



Appendix 4.5. TEM images of fragmented fibrils by sonication. PI-Fiber (< 1 mg) in 4 ml of NMP were sonicated for 2 h, and shortening and fragmentation was observed while maintaining the overall morphology.

국문 초록

재료 설계는 원하는 기능을 위한 빌딩 유닛뿐만 아니라 적절한 반응 조건에 대한 섬세한 고려가 필요한 경우가 많다. 전구체, 상, 온도, 압력, 부가물, 촉매 및 기질의 종류를 제어하면 결과 물질의 전체 형태와 기능이 변경된다. 따라서 빌딩 블록에 대한 적절한 설계 전략은 설계된 재료에서 원하는 기능의 잠재력을 최대한 활용하기 위해 고려되어야 한다. 이 논문은 상향식 접근법을 통한 단백질 기반 생체 재료 및 다공성 유기 폴리이미드의 생성에 대해 다룬다. 선택된 전구체들을 1, 2, 3차원으로 확장하기 위한 적절한 설계 전략이 논의될 것이다.

1장에서는 인공적으로 확장된 단백질 자가조립 구조에 대한 분야를 간략하게 소개한다. 다양한 단백질-단백질 경계면 설계 전략 중 인공적인 단백질 자가 조립을 위한 배위 결합의 활용에 대해 주로 논의한다. 2장에서는 비자연적 킬레이트 아미노산인 bpy-Ala를 부위 선택적으로 유전적으로 결합한 후 금속 이온을 추가함으로써 다양한 단백질 조립 구조를 프로그래밍할 수 있음을 나타내었다. 연구를 위해 선택한 단백질은 자기 조립과 관련된 구조적 및 기능적 특성을 나타내지 않지만 킬레이트 리간드의 도입과 함께 Ni^{2+} 를 추가하면 강력하고 가역적인 연결 모듈인 $[Ni(bpy)_2]$ 이 생성되어 선택적이고 조정 가능한 단백질 조립이 가능한 것을 보여주었다. 단일 사이트 돌연변이만으로도 1차원 선형 막대, 2차원 p312 구조를 가진 평면, 비결정질 2차원, 1차원과 2차원의 조합 물질 및 섬유성 계층 구조와 같은 다양한 구조를 생성하기에 충분했으며, 금속 배위 리간드는 강력하고 다양한 구조를 생성하기 위해 충분히 강한 에너지와 설계 가능한 방향성을 부여하는 것을 나타내었다. 단백질 자가 조립 과정은 다양한 반응 조건에서

광범위하게 연구되었으며, 열역학 및 화학 속도론에 관련된 여러 요인들이 단백질 조립 구조의 길이와 모양을 조절했음을 확인하였다. 게다가, 자가 조립된 단백질 구조는 고유의 효소 활성을 나타내면서 열적 안정성을 얻었으며, 이는 비자연적 킬레이트 아미노산을 이용한 무기 반응성이 구조적으로 매우 복잡한 단백질을 다양한 단백질 기반 기능 재료 및 생체 촉매로 쉽게 템플릿화할 수 있음을 의미한다.

3장에서는 에너지 저장 물질을 위한 산화환원 활성 다공성 유기 고분자의 활용에 대해 설명한다. 산화환원 활성 다공성 유기 고분자의 특성과 장점을 전극 응용 측면에서 논의하는 것을 목표로 한다. 4장에서는 주로 구조-기능 관계에 기반한 고성능 에너지 저장 장치의 설계 전략에 초점을 맞춘다. 헥사아자트리페닐렌 카르복실산과 멜라민의 조합을 사용하여 투과성이 높은 구조를 갖는 산화환원 활성기를 포함하는 다공성 유기 고분자를 구성하는 것을 목표로 한다. 우리의 설계 전략은 (1) 고에너지 밀도 재료를 위한 고도로 산화환원 활성인 헥사아자트리페닐렌 트리아미드 그룹을 합성하고 (2) 고출력 밀도 재료에 필요한 높은 이온 흐름을 촉진하기 위해 뒤틀린 미세 기공으로 인한 메조 기공 채널을 생성하는 것이었습니다. 자가 조립을 합성 방법으로 채택하여 완전히 이미드화된 네트워크 구조를 가진 균질한 원섬유 형태의 구조가 합성되었으며, 이는 목표로 한 고도의 산화환원 활성 그룹이 성공적으로 형성되었음을 나타냅니다 (PI-Fiber). 구조 분석을 통해 설계한 대로 균일한 크기의 미세 기공을 갖는 계층적 다공성 구조가 형성되었음을 확인하였다. 우리 재료는 결정질이 좋지 않은 시스템이지만 목표로 하는 이미드 결합과 구조가 형성되어, 자가 조립을 이용한 접근 방식이 효과적인 방법임을 나타내었다. 예상대로 빠른 충방전 속도에서도 높은 충전 용량을 가진 슈도캐패시터로서의

동작을 확인할 수 있었다. 우리의 활성 물질은 중간 정도의 안정성을 보였고 물질 자체가 가지고 있는 빠른 역학과 불안정화 메커니즘은 순환 전압 전류법을 통해 연구되었다. 우리는 또한 실제 장치에서의 응용 가능성을 테스트하기 위해 2전극 시스템을 구축하였다. 조립된 AC//PI-Fiber 전지는 중간 정도의 안정성과 함께 높은 전력 및 에너지 밀도를 나타내어 PI-Fiber가 실제 적용을 위한 장래의 전기화학 재료가 될 수 있음을 보여주었다.

주요어: 생체 재료, 비피리딘 금속 복합체, 폴리이미드, 다공성 유기 고분자, 단백질 자가 조립, 슈도커패시터, 산화환원 고분자, 가역 반응.

학 번: 2017-27428